Hills and valleys

Novel effects in the spectra of nuclear, atomic, and mesoscopic systems

DISSERTATION

submitted for the award of the title

Doctor of Natural Sciences

to

The Faculty of Physics, Mathematics, and Computer Science

of

Johannes Gutenberg University Mainz

Pavel Fadeev

July 2022

Thesis Advisors:

Professor Dr. Dmitry Budker and Professor Dr. Victor V. Flambaum

Abstract

High-precision measurements of frequencies move humanity forward in fundamental understanding of nature and technological innovation. We employ various spectroscopic techniques in nuclear, atomic, and mesoscopic systems to predict effects of the weak force, to bound the magnitude of possible phenomena beyond the Standard Model, and to propose how to measure the gyrogravitational ratio.

- In nuclear systems, temporal or spatial variation of the fine-structure constant α or the quark mass m_q can cause shifts in the nuclear energy levels. We determine the sensitivity to such effects in Mössbauer transitions as well as in the nuclear clock transition of thorium-229. We find that a change in α can be connected to a change in m_q, such that we can deduce one change from the other. Further in the nuclear realm, we find the magnitude of time-reversal-invariance violation in neutron-nucleus scattering, an effect of the weak force, providing a theoretical validation of ongoing experimental efforts.

- In atomic spectra, should discrepancies arise between the expected transition frequency and the measured one which cannot be accounted for by known effects or any kind of uncertainty, they could be explained by novel effects beyond the Standard Model. New bosons, such as axionlike particles and Z' bosons, if they exist, can be exchanged between the constituents of atoms, giving rise to interaction potentials which shift the electronic energy levels. We compile a list of such potentials, sorting them by type of coupling. We put bounds on the coupling constants of such interactions in antiprotonic helium, muonium, positronium, helium, and hydrogen.

- A mesoscopic-sized ($10^2 - 10^5$ nm) ferromagnet is a treasure mine for exploration. The coupling between the magnetization and the rigid structure of a ferromagnet gives rise to interesting dynamics. Specifically, in low magnetic fields (below 10^{-11} T for a micrometer magnet) a magnet is predicted to precess. We explore a levitated ferromagnet's behavior as a gyroscope, as a system to test for exotic bosons, and as a setup to test the gyrogravitational ratio.

Acknowledgments

"I would like to thank God it is over", said a friend of their PhD coming to an end. A PhD is a formidable endeavor. Like a roller coaster, it has its ups and downs. Taking this wild ride, I learned how to explore the universe, how to do science. At the front line of the past years' learning curve are my two supervisors and mentors, from each of whom I learned an ocean of knowledge.

Victor Flambaum, you taught me to put pen to paper, fingers to keyboard, from day one of a new project. I observed and learned from you the value of checking results in several ways for consistency, your pragmatic approach in face of the unknown. If I stretched your patience at times, then just as stretching to reach the ball when we played table tennis, it was worth it. When we played you noted, half joking, that you need to consult your trainer. You trained me in science for years. Thank you, Victor. If science were a table-tennis game, I would feel ready to turn pro.

Dima Budker, you showed me how to incorporate enthusiasm into our scientific work. I witnessed and absorbed how to collaborate in constructive ways with colleagues; to make sure we understand the foundations while exploring the frontier and focusing on a specific question. All this, in a steady manner: I recall we were reading a paper before submission. After dinner we had Limoncello. As my shot disappeared at once, you remarked, "you might consider drinking it gradually". "Very well", I replied, "pour another, I shall do so". Thank you, Dima.

Consistent progress, having an eye for important problems in versatile fields, and finding links between experiment and theory were present on both sides of the Indian ocean (Victor based in Australia, Dima is in Germany).

Thank you both for letting me decide at important junctions of the PhD on the projects I want to do. When questions of the sort "how about you go in this direction?" and "I have an idea for the next project for you" where answered by "I was thinking of a different direction" and "I have a different idea", my opinions where accounted for. This made me feel in charge of my research projects and having responsibility for them. Besides, when I feel it's my decision to work on a project, this makes me love it so much more.

Thanks to all the coauthors of the papers in this thesis. It is a pleasure to explore with you, in any place: be it Poznan, Poland, where Filip and I figured out the accurate way of constructing plots in our project; or Sydney during the pandemic, where Julian and I, coming to the office, were plunging through prolate spheroids, because it was too hard to stay at home.

Supervisors and coauthors are crucial to the PhD experience, and so are friends, colleagues, and the community at large. Anne Fabricant, thank you for editing my papers and this thesis, some of it in the countryside of Denmark, showing me how to carefully thread words into beautiful sentences with clear meaning. Anna Viatkina, thank you for your company during our visits to Victor. The months we spent there were much improved by sharing the challenges of science as well as going on hikes in Sydney. Martti Raidal, thank you for your hospitality in Tallinn. I felt like part of your group for a month; it was a lovely example of the scientific inclusive spirit.

There is much and there are many to be thankful for — let us mention a few more.

Amy Geddes, thank you for keeping me in shape, jumping to virtual fitness exercises after a day of science in locked-down Sydney, and for the oysters in North Haven.

Bryce Lackenby and Emily Kahl, thank you for your company in Sydney.

Marina Gil, thank you for bringing me to the other end of the world, where I met a great community and did science truly remotely, on an island surrounded by coconut trees.

Bernd Saering, who taught me astrophysics in high shool, thank you for showing me early on what physics is about and inspiring me.

Joanna Woo, who took the time to walk me through my first science project.

My parents and family, thank you for your trust and unconditional love.

Declaration of authorship

With this statement I declare that this PhD thesis and the work presented therein are my own. This work was done during my PhD candidature years at the Johannes Gutenberg University Mainz and on academic visits to The University of New South Wales in Sydney. Where external published or work is consulted, this is stated and the source is given. Hereafter is stated how the research presented was done jointly with others. I have not submitted the present thesis or parts of it as a dissertation or examination paper to another university, faculty or department.

Istanbul, 31.05.2022 Pavel Fadeev

As the lead author of every paper in the thesis, I was in charge of each project, writing the manuscript and obtaining central results. Each draft of the project was given extensive feedback by the coauthors, with parts rewritten as a result. In some occasions, sections were written by coauthors: section 1.1 was written by Victor Flambaum, section 6.1.2 was written by Alex Sushkov, and section 7.5 was written by Derek Jackson Kimball.

This is not one person's work, it is a team effort. I was obtaining the results in close cooperation with coauthors. In the nuclear part of the work I performed the calculations under guidance of Victor Flambaum. For example, Victor suggested to keep the volume constant in nuclear transitions, to help in cases where measurements of quadrupole momemts are not precise enough. I did so using mathematica, and Julian Berengut verified my results.

In spin-dependent potentials work, the middle part of the thesis, I worked with Filip Ficek on the plots bounding the properties of exotic bosons. When we were stuck we ask the coauthors and got valuable suggestions that moved us forwards. My calculations for the forms of potentials were verified by Yevgeny Stadnik.

In the work on ferromagnetic gyroscope, I took Derek's idea to use a precessing magnet as a probe for gravity and turned it, with our team, into a paper proposing an experiment for this purpose. I realized modeling was necessary, did it and obtained the necessary results. Then I found the formula for libration frequency, which was observed in ongoing experiments. Reaching out to people working on these experiments, we collaborated and I wrote a second paper on the subject, proposing a roadmap to construct a prototype device in a laboratory. I discovered and quantified how the dynamics of a levitating magnet above a superconductor differ from a magnet freely falling in space.

Contents

Introduction

Frequencies can be measured with less uncertainty than any other physical quantities, therefore playing a central role in precision experiments. In this work we explore phenomena that can affect the spectral lines of nuclear, atomic, and mesoscopic systems. A brief background of each topic follows, as well as an overview of our contributions.

In nuclear physics, ongoing experimental efforts, such as by the NOPTREX (Neutron Optics Time Reversal Experiment) collaboration, aim to measure time-reversal violation in neutron-nucleus scattering. We provide a prediction of such effects, showing that time-reversal symmetry is large enough to be detected in the experiment. This is covered in the first chapter.

In the second chapter, we turn to the lowest-energy nuclear transition in thorium-229. This transition is a promising candidate for a nuclear clock. We predict the sensitivity of this transition to temporal variation in the fine-structure constant α. That is to say, we find out how much the transition changes for a given variation in α. This is done for both quadrupole and octupole deformations of the nuclei. We present the possibility that the volume of the nucleus is constant in isomeric transitions, and test this assumption for nuclear transitions in several chemical elements.

Expanding upon variation of fundamental constants, in the third chapter we discuss such effects in the realm of Mössbauer spectroscopy. Besides variation in α, we consider variation of the quark-mass m_q. We find a way to link the sensitivities of isomeric transitions to variations in α and m_q, drawing from previous results in the literature. We compile an extensive list of these sensitivities in Mössbauer transitions.

In atomic physics, the exchange of exotic bosons between the constituents of atoms could affect atomic energy levels, affecting thus the measured spectra. Each exotic boson comes with its own type of interaction, such as a scalar or pseudovector interaction, which gives rise to an exchange potential which shifts the atomic energy levels. In the fourth chapter, we derive these potentials, nine in total, sorted by type of interaction. In each potential, the terms that contribute the most to each type of interaction are included. We discuss their properties in the context of previous theoretical results and current experimental efforts.

In the fifth chapter, we focus on the pseudovector and the pseudoscalar interactions. The former depends inversely on the square of the boson mass. We explain why such an interaction makes sense (i.e., does not explode when the boson mass goes to zero) and how to produce bounds on the properties of exotic bosons. Then, we use experimental spectra of

antiprotonic helium, muonium, positronium, helium, and hydrogen to extract bounds on the interaction constants of the potentials.

Moving to the sixth chapter, into the realm of mesoscopic systems, we propose an experiment, Gravity Prove Spin, to measure the value of the gyrogravitational ratio for an electron. This ratio determines the response of the intrinsic spin $\boldsymbol{s}$ to gravity, compared to the response of orbital angular momentum $\boldsymbol{l}$ to gravity. In our vision, a ferromagnet precessing in the presence of a weak magnetic field is sensitive to Lense-Thirring and de Sitter gravitational effects. We calculate the experimental requirements and the sensitivity needed for detection of gravitational effects acting on the magnetization. We model the ferromagnet dynamics within the provided experimental parameters and show the predicted signals in graphs of power spectral density. Such a setup can be used as a high-precision gyroscope for technological applications.

In the final, seventh, chapter, we team up with experimentalists from UK and Italy to envision a proof-of-principle experimental realization of a precessing ferromagnet levitating above a superconductor. We model such a setup, predicting the resulting precession and where in the power spectrum it will appear. A negative feedback mechanism shows up in the dynamics of a levitating magnet. We develop an analytical model that explains the numerical results and show how to use this setup to provide bounds on the properties of new bosons discussed in fourth and fifth chapters.

Overall, lines in spectra, be they atomic, nuclear, or power spectra, continue to provide fertile ground for advances, see Fig. 1 for a graphic summary of the topics in our work. We help explorers in several disciplines: investigators of weak-force effects in nuclei, detectives of new particles and variation of constants, mixers of gravitational and quantum properties, and builders of gyroscopes.

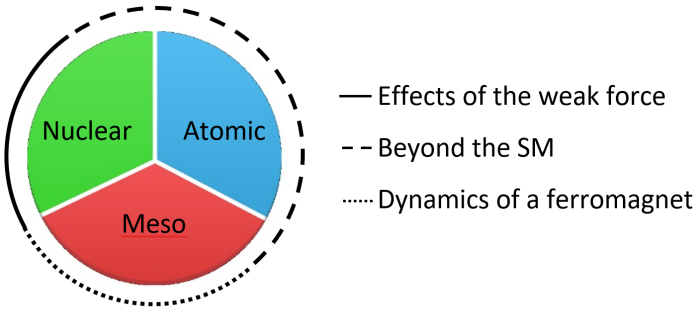

Figure 1: *Our work involves nuclear, atomic, and mesoscopic physics. The segments around the pie chart represent more specific topics. The continuous line above nuclear physics stands for weak-force effects in neutron-nucleus scattering. Dashed line stands for beyond-the-Standard-Model effects: variation of fundamental constants in nuclear transitions, possible contributions of exotic-bosons exchange to atomic transitions, and the effects of such bosons on the dynamics of a magnet, a mesoscopic setup. In mesoscopic systems, the dotted line stands for dynamics of a ferromagnet in low magnetic-fields, where we look for precession and nutation behaviour, as well as the coupling of gravity to magnetization.*

Time-symmetry violation in heavy-atoms scattering

A century ago, Emmy Noether linked fundamental symmetries of nature to the corresponding conserved quantities of a physical system [3]. Nowadays we sort symmetries of nature into two types: continuous and discrete. Energy and momentum conservation are associated with the first type, while parity, charge, and time conservation are associated with the second. Parity is conserved when a physical process is unchanged under spatial inversion, also known as parity transformation. Time or charge parity is conserved when time reversal or a change in sign of the electric charge, respectively, does not change the process.

The possibility of spatial parity being violated when the weak force is involved was proposed by Tsung-Dao Lee and Chen-Ning Yang in 1956 [1], and observed in beta decay of cobalt-60 in the group of Chien-Shiung Wu [2].

Efforts to observe parity violation in gamma-ray spectra of scattering events between neutrons hitting a target of heavy atoms proved challenging. In 1980, Victor V. Flambaum and Oleg P. Sushkov predicted that the parity-violations effect would be much larger in this system than previously thought [4]. A few years later, this prediction was verified in Dubna, using transmission spectrum of neutron-nuclei scattering [5–7]. Further experiments followed in US and Japan [8–12].

In scattering experiments of neutrons hitting a stationary target of compound nuclei, the scattering cross-section depends on the spin of both systems. The neutron-nucleus forward-scattering amplitude is

$$f = A + B\boldsymbol{\sigma}\cdot\boldsymbol{I} + C\boldsymbol{\sigma}\cdot\boldsymbol{k} + D\boldsymbol{\sigma}\cdot(\boldsymbol{I}\times\boldsymbol{k}) \ , \tag{1}$$

where $\boldsymbol{\sigma}$ is the neutron spin operator, $\boldsymbol{I}$ is the spin operator of the target nuclei, and $\boldsymbol{k}$ is the neutron momentum. The third and fourth terms violate parity, since $\boldsymbol{k}$ changes sign under parity transformation while $\boldsymbol{\sigma}$ does not. The fourth term also changes sign under time reversal, as its three operators change sign in such a transformation. Bombarding nuclei with neutrons in opposite helicity states, i.e. $\boldsymbol{\sigma}$ parallel or antiparallel to the momentum of the neutron, gives different cross-sections if the interaction does not conserve parity. This parity violation is a result of W-bosons exchanged in the weak interaction between neutrons and compound nuclei. The experimental result is shown in Fig. 2. Time-parity violation, another manifestation of W-boson exchange, has been observed in accelerators, but not yet in compound systems, since it is smaller than parity-violation effect.

How much smaller? While the magnitude of the parity-violation effect was predicted and measured, the magnitude of time-symmetry violation in neutron-nucleus scattering experiments system was not well-known theoretically or measured experimentally. Thus, the NOPTREX collaboration [13], looking for this effect, relied at first on a theoretical estimate of a three-body interaction in neutron-deuteron scattering [14]. But the NOPTREX experiment uses much heavier nuclei. Our theoretical result for heavy nuclei gives a justification for the ongoing experimental effort. We estimate the magnitude of the time-reversal invariance violation effect (T-violation), and conclude that the sensitivity in neutron-reaction experiments may be sufficient to improve the uncertainty limits on measurements of T-violating interactions. These results are covered in the paper forming the first chapter of the thesis:

- *Time-reversal invariance violation in neutron-nucleus scattering*
  P. Fadeev and V. V. Flambaum
  Phys. Rev. C **100**, 015504 (2019).

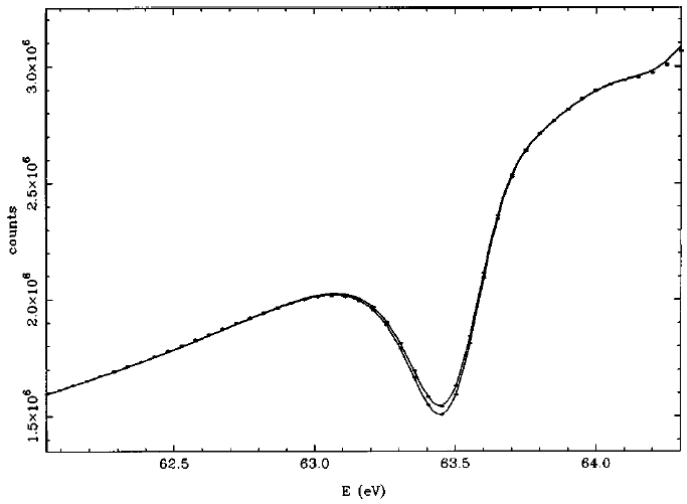

Figure 2: *Two overlaid neutron-transmission spectra for neutron-nuclei scattering of neutrons in opposite helicity states [15]. The effect of parity violation can be seen by eye in the difference between the two spectra in the region where the neutron energy is around 63.5 eV. The asymmetry is about 4%, with sufficiently small uncertainties to exclude a null result, Figure 4 in [15].*

Fine-structure-constant variation in the nuclear clock

After exploring violation of time-reversal symmetry, we move to violation of the constancy in time and space of fundamental constants. Suggested by Paul Dirac in order to keep constant the ratio between natural constants of cosmology and atomic theory [16], as well as by Brans and Dicke to incorporate Mach's principle into general relativity [17], the topic continues to be relevant. Interest in such a violation surged as it became possible to probe it on cosmological scales, and as it was realized that dark matter could induce change in the constants, among other reasons [18–20].

One way to look for temporal or spatial changes in fundamental constants is to study their effects on atomic and nuclear spectra. Atomic and nuclear energy levels depend on the value of the fine-structure constant α; if α changes, the energy levels shift. If such a change exists, it must be small, otherwise we would have seen it already, so high precision is needed in the measurement of transition frequencies. The highest precision is achieved nowadays with atomic clocks, see Fig. 3. Even higher precision is promised when a nuclear clock is constructed, as the nucleus is screened from external effects by the surrounding electrons. With an eye to the future, we focus on nuclear transitions. Specifically, we focus on the nuclear transition having lowest known frequency, the first excited state in thorium-229. Experimentalists are in hot pursuit of its direct detection, with several recent indirect

measurements [22, 23]. A direct detection of such a transition has many potential benefits for fundamental physics [24].

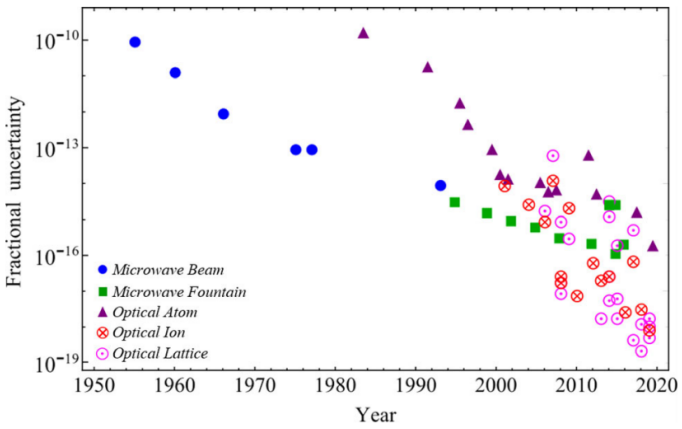

Figure 3: *Fractional uncertainties in frequency of various kinds of atomic clocks over the past 70 years, from [21]. The fractional uncertainty in the future nuclear clock are expected to be even lower, around* 10^{-20}.

The fractional variation in α is linked to to the fractional variation in nuclear-transition frequency f through the enhancement factor K:

$$\frac{df}{f} = K\frac{d\alpha}{\alpha}\,.$$

The factor K equals the ratio of ΔE_C, the change in Coulomb energy in a nuclear transition, to f:

$$K = \frac{\Delta E_C}{f}\,.$$

Smaller f gives larger K. Longer half-life of the nuclear transition corresponds to a more stable nuclear isomer, which is easier to work with experimentally. Nuclear transitions with relatively long half-life and low energy (small transition frequency f) are most sensitive to such variation in α. Our task thus is to derive K.

Using experimental values of the mean-square radius $\langle r^2\rangle$ and the quadrupole moment Q_0, we calculate ΔE_C for the lowest nuclear transition in ^{229}Th. We go further, generalizing from a spheroid-shaped nucleus to a pear-shaped one, Fig. 4. This way we consider possible octupole deformation of the nucleus and quantify its effect on ΔE_C.

Measurements of octupole and quadruple moments are a source of large uncertainly in the determination of K from experiment. To avoid this uncertainly, we consider isomeric transitions in which the volume of the nucleus stays the same. We find a simple relation between $\langle r^2\rangle$ and Q_0 when the volume is conserved,

$$\frac{dQ_0}{d\langle r^2\rangle} = 1 + \frac{2\langle r^2\rangle}{Q_0}\,.$$

We quantify the accuracy of this assumption in thorium-229 and successfully test our model on several other elements. The second chapter presents the details, in the following letter:

- *Sensitivity of ^{229}Th nuclear clock transition to variation of the fine-structure constant*
  P. Fadeev, J. C. Berengut, and V. V. Flambaum
  Phys. Rev. C **102**, 052833 (2020).

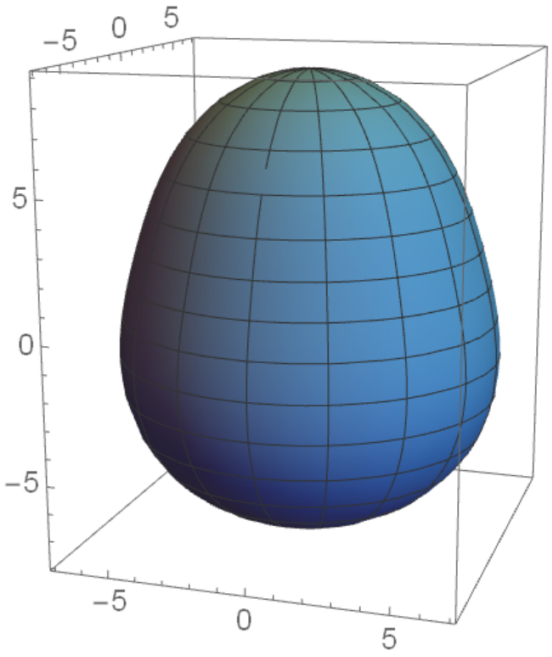

Figure 4: *Octupole deformation of the nucleus shows as a pear shape. The axes are lengths in femtometers.*

Mössbauer spectroscopy as a tool to detect variation in fundamental constants

The thorium nucleus is not the only one sensitive to variation of fundamental constants. To detect experimentally such a variation in other nuclei, an established technique that measures nuclear transitions with high accuracy is beneficial. One such technique is Mössbauer spectroscopy.

Mössbauer spectroscopy is a way to obtain the spectrum of nuclear transitions which overcomes the frequency shift due to recoil of the nucleus upon emission of a photon. This is possible when the nucleus is inside a solid–state material, as then the nucleus is incorporated in the lattice of the material, and the recoil energy thus spreads to the whole lattice instead of one nucleus recoiling. For recent reviews, see [25, 26].

We propose a new subfield of research: the search for space-time variation of the fundamental constants, possibly due to low-mass scalar dark matter, using Mössbauer transitions.

We compile a comprehensive list of suitable candidate transitions, propose several types of experiments, and perform necessary nuclear calculations. The work is of interest for nuclear, particle, and atomic-physics communities.

Similar to the enhancement factor for the variation of the fine-structure constant, the enhancement factor K_q for the variation of the quark mass is

$$\frac{\delta f}{f} = K_q \frac{\delta m_q}{m_q} \,. \tag{2}$$

Combining our model with previous results, we arrive at a possible link between the enhancement factors K_q and K_α:

$$K_q = 1.45(K_\alpha - 1) \,. \tag{3}$$

The full story is presented in the third chapter, based on the paper:

- *Effects of variation of the fine structure constant α and quark mass m_q in Mössbauer nuclear transitions*
  P. Fadeev, J. C. Berengut, and V. V. Flambaum
  Phys. Rev. C **105**, L051303 (2022).

Spin-dependent potentials

The forces of nature are mediated by integer-spin particles called bosons: photons for the electromagnetic force, gluons for the strong force, Z and W bosons for the weak interaction — and gravitons, if discovered, will be the carriers of gravity.

Yet-to-be-discovered bosons, such as the paraphoton, axion, and Z' boson, could solve decades-old questions. These exotic bosons provide possible explanations for dark matter, dark energy, and the the CP puzzle (why does quantum chromodynamics seem to preserve CP-symmetry?).

In 1984, Moody and Wilczek [27] pointed out that some of the forces that exotic bosons provide can have macroscopic effects, called "new macroscopic forces". In 2006, a list of them was compiled by Dobrescu and Mocioiu [28]. Previously, we used these potentials to constrain the properties of exotic bosons in antiprotonic helium [29].

In 2006, the potentials were compiled and sorted by their spin-momentum form into 16 types; lookalike potentials were gathered in one group, even though they come from different bosons [28]. We sort them differently: each Lagrangian has one kind of boson in it. As each boson has two types of couplings, their combinations produce three families of potentials for each Lagrangian. This makes it easier to track the influence of different kinds of bosons on the particles, and one can see which spin-momentum terms contribute the most to each kind of interaction.

We include contact terms $\delta(\boldsymbol{r})$ in the potentials. These terms do not appear in the interaction between macroscopic objects which are not in direct contact with each other.

This is why these terms were omitted in a number of previous theoretical and experimental publications. However, they contribute to the interactions inside atoms and molecules. For some searches, contact terms can be the main actor — a hyperfine magnetic dipole-dipole interaction comes to mind as an example. Finally yet importantly, we make order. Over the years, factors and signs went astray, phantom potentials were searched for, and confusion over notation arose. We did our best to erase such misconceptions. The result is in the fourth chapter, following the paper:

- *Revisiting spin-dependent forces mediated by new bosons: Potentials in the coordinate-space representation for macroscopic- and atomic-scale experiments*
  Pavel Fadeev, Yevgeny V. Stadnik, Filip Ficek, Mikhail G. Kozlov, Victor V. Flambaum, and Dmitry Budker.
  Phys. Rev. A **99**, 022113 (2019).

While revisiting the potentials, we encountered a contribution proportional to the inverse square of the intermediate spin-one boson mass, $1/M^2$, originating from the longitudinal spin polarization. We analyzed this contribution, as well as the way contact terms are calculated numerically, and obtained new bounds on the corresponding interactions using data from recent atomic experiments. The results in the fifth chapter are:

1. First limits on the spin-spin interaction with $1/M^2$ term.
2. Explanation and solution for the apparent divergence of the $1/M^2$ term.
3. Use of the contact terms to perform numerical calculations.
4. Based on the previous points, bounds on coupling constants as a function of boson mass in the systems of antiprotonic helium, muonium, positronium, helium, and hydrogen — relying on the experimental spectra, theoretical calculations, and our estimate of the potentials' contribution.

These results were published in the following letter:

- *Pseudovector and pseudoscalar spin-dependent interactions in atoms*
  Pavel Fadeev, Filip Ficek, Mikhail G. Kozlov, Dmitry Budker, and Victor V. Flambaum
  Phys. Rev. A **105**, 022812 (2022).

A timely quotation says: "Recent precision atomic-spectroscopy measurements have uncovered several small discrepancies between experiment and theory" [30]. The effects of novel bosons in atoms provide possible explanations of such discrepancies, in case they cannot be explained by conventional means.

Precessing magnet

In the last part of the thesis, we explore the power spectrum of the motion of a rotating ferromagnet. Under the influence of a weak magnetic field (less than 10 pT for a micrometer

magnet), the ferromagnet behaves like a spinning top, precessing and nutating. The macroscopic magnetization is built from an ensemble of individual electron spins. In this regime, it should be possible to probe the reaction of quantum spins to general-relativistic effects.

A decade ago, Gravity Probe B, a satellite containing four highly spherical niobium-coated fused quartz gyroscopes in a cryogenic environment, measured precession of angular momentum of the gyroscopes due to gravitational effects predicted by general relativity [31]. Experimentally, it is unknown if the intrinsic spin of an electron precesses due to gravitational effects in the same way as the quartz gyroscopes precessed in Gravity Probe B.

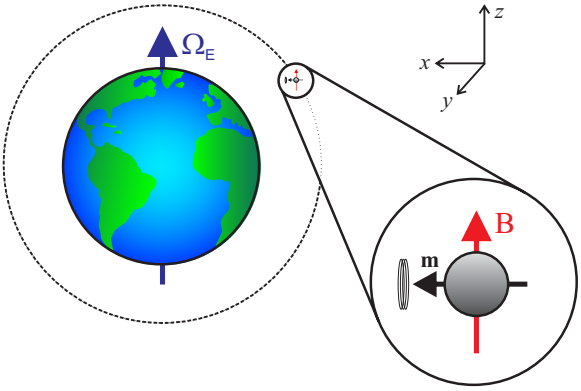

Figure 5: *Conceptual schematic diagram of a "Gravity Probe Spin" experiment. A freely floating spherical ferromagnet located within a superconducting shield is in a circular polar orbit. The static magnetic field B (from the flux in the superconducting shields) is oriented along $\hat{z}$, parallel to the direction of Earth's rotation axis $\mathbf{\Omega}_E$. The inset shows the initial orientation of the magnetization $\boldsymbol{m}$ along the $\hat{x}$ axis. The pick-up coil measures the ferromagnet's magnetization along $\hat{x}$. Gravity may couple to the magnetization, causing a modulation of the measured signal. This geometry is designed for the detection of the Lense-Thirring effect.*

Due to the weak coupling, it is infeasible to test general-relativistic precession of intrinsic spin using a single electron. However, an ensemble of electrons enables new possibilities. Recently we proposed a space mission similar to Gravity Probe B where instead of spherical quartz gyroscopes, millimeter-scale ferromagnets are used. In Fig. 5 a schematic diagram of the setup is shown. Modelling the dynamics of such a setup reveals that the experiment would be sensitive enough to detect the Lense-Thirring effect or the de Sitter effect on intrinsic spin [32]. The story is told in the following letter:

- *Gravity Probe Spin: Prospects for measuring general-relativistic precession of intrinsic spin using a ferromagnetic gyroscope*
  Pavel Fadeev, Tao Wang, Y. B. Band, Dmitry Budker, Peter W. Graham, Alexander O. Sushkov, and Derek F. Jackson Kimball
  Phys. Rev. D **103**, 044056 (2021).

In order for a ferromagnet to behave like a gyroscope, its angular momentum must be dominated by the intrinsic spin of the electrons [33]. This condition demands that the ambient

magnetic field should be low (0.1 – 10 pT). Efforts are ongoing to carry out a proof-of-principle experiment to observe precession of a ferromagnet in the laboratory [34, 35].

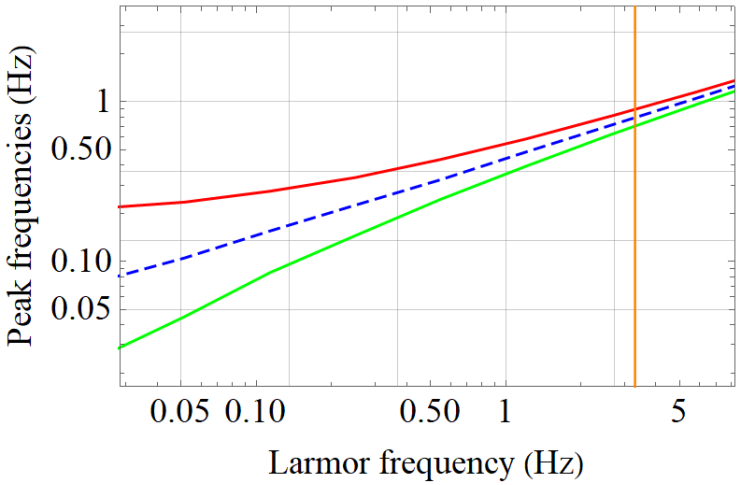

Figure 6: *Modelling the dynamics of a ferromagnet. Presented are the frequencies of the maxima in the spectrum of ferromagnet dynamics as a function of the Larmor frequency (as can be measured with a SQUID pick-up loop). The Larmor frequency is proportional to the applied magnetic field. The red and green curves (top and botton) are the frequencies corresponding, respectively, to nutation and precession frequencies. For Larmor frequencies greater than 3 Hz (vertical line), the two spectral lines converge to the frequency plotted in dashed blue, which corresponds physically to librational motion.*

One of the obstacles to carrying out such a proof-of-principle experiment is the problem of how to levitate the ferromagnet and isolate it from the environment so that it is free to precess. This problem is far easier to solve if the experiment is performed in a microgravity environment, such as the International Space Station or a satellite orbiting the Earth. Three main ingredients are required: a mm- to μm-scale ferromagnet, magnetic shielding and field-control coils, and a sensitive magnetometer, such as a superconducting quantum interference device (SQUID), to measure the ferromagnet's dynamics.

With these ingredients in place, various types of motion of the ferromagnet can be recorded as changes in the flux through the SQUID pick-up loop. In relatively large magnetic fields, the ferromagnet librates (wobbles), producing a characteristic frequency. This frequency has been observed in experiments [36]. In relatively low magnetic fields, we predict the libration frequency to effectively split into nutation and precession frequencies, the red and green curves in the Figure 6, enabling a method to tune the magnetic field to values where precession can be observed.

The precession can be observed in ground-based experiments as well. To this end, we proposed and modelled precession dynamics in a magnet levitated above a superconductor. We discovered that in such a system the threshold magnetic field below which precession occurs is much bigger compared to space environment. However, precession frequency then is lower. Such a mechanism is similar to a negative feedback. We explained this behaviour with an analytical model. In addition, we showed that the setup is sensitive to exotic spin-dependent interactions. The results are in:

- *Ferromagnetic Gyroscopes for Tests of Fundamental Physics*
  Pavel Fadeev, Chris Timberlake, Tao Wang, Andrea Vinante, Y. B. Band, Dmitry Budker, Alexander O. Sushkov, Hendrik Ulbricht, and Derek F. Jackson Kimball
  Quantum Sci. Technol. **6**, 024006 (2021).

In summary, experiments with levitated ferromagnets in a microgravity environment, or in a levitated system, can open possibilities for new tests of fundamental physics [33, 34], including on the boundary between quantum physics and general relativity [32].

Bibliography

[1] T. D. Lee and C. N. Yang, Phys. Rev. **104**, 254 (1956); Erratum Phys. Rev. **106**, 1371 (1957).

[2] C. S. Wu, E. Ambler, R. W. Hayward, D. D. Hoppes, and R. P. Hudson, Phys. Rev. **105**, 1413 (1957).

[3] E. Noether, Nachrichten von der Gesellschaft der Wissenschaften zu Göttingen, Mathematisch-Physikalische Klasse 235 (1918).

[4] Flambaum, V. V., and O. P. Sushkov, Phys. Lett. **94B**, 277 (1980).

[5] V. P. Alfimenkov, S. B. Borzakov, V. T. Vo, Yu. D. Mareev, L. B. Pikelner, A. S. Khrykin, and E. I. Sharapov, JETP Lett. **35**, 51 (1982).

[6] V. P. Alfimenkov, S. B. Borzakov, Vo Van Tkhuan„ Yu. D. Mareev, L. B. Pikelner, A. S. Khrykin, and E. I. Sharapov, Nucl. Phys. A **398**, 93 (1983).

[7] V. P. Alfimenkov, S. B. Borzakov, Vo Van Tkhuan„ Yu. D. Mareev, L. B. Pikel'ner, I. M. Frank, A. S. Khrykin, and E. I. Sharapov, Pis'ma Zh. Eksp. Teor. Fiz. **39**, 346 (1984) [JETP Lett. **39**, 416 (1984)].

[8] T. Okudaira, S. Takada, K. Hirota, A. Kimura, M. Kitaguchi, J. Koga, K. Nagamoto, T. Nakao, A. Okada, K. Sakai, H. M. Shimizu, T. Yamamoto, and T. Yoshioka, Phys. Rev. C **97**, 034622 (2018).

[9] Numerous review articles appear in *Parity and Time Reversal Violation in Compound States and Related Topics*, edited by N. Auerbach and J.D. Bowman (World Scientific, Singapure, 1996).

[10] A. G. Beda and V. R. Skoy, Phys. Part. Nucl. **38**, 1063 (2007).

[11] W. M. Snow, *Null Tests of Time Reversal Invariance Using Neutrons*, Proc. Sci. **294**, 007 (2017).

[12] M. Kitaguchi, K. Asahi, S. Endo, C. C. Haddock, M. Hino, K. Hirota, T. Ino, I. Ito, T. Iwata, J. Koga, Y. Miyachi, T. Momose, N. Oi, T. Okudaira, K. Sakai, T. Shima, H. M. Shimizu, S. Takada, Y. Yamagata, T. Yamamoto, and T. Yoshioka, JPS Conf. Proc. **22**, 011034 (2018).

[13] L. B. Palos (NOPTREX Collaboration), talk at Thirteenth Conference on the Intersections of Particle and Nuclear Physics (2018). https://conferences.lbl.gov/event/137/session/18/ contribution/139/material/slides/0.pdf.

[14] Y.-H. Song, R. Lazauskas, and V. Gudkov, Phys. Rev. C **83**, 015501 (2011).

[15] B. E. Crawford, J. D. Bowman, P. P. J. Delheij, T. Haseyama, J. N. Knudson, L. Y. Lowie, A. Masaike, Y. Matsuda, G. E. Mitchell, S. I. Penttilä, H. Postma, N. R. Roberson, S. J. Seestrom, E. I. Sharapov, S. L. Stephenson, and V. W. Yuan, Phys. Rev. C **58**, 1225 (1998).

[16] P. A. M. Dirac, Proc. R. Soc. A **165**, 199 (1938).

[17] C. Brans and R. H. Dicke, Phys. Rev. **124**, 925 (1961).

[18] L. Perivolaropoulos and F. Skara, arXiv:2105.05208.

[19] D. Milaković, C.-Chi Lee, R. F. Carswell, J. K. Webb, P. Molaro, and L. Pasquini, Mon. Not. Roy. Astron. Soc. **500**, 1 (2020).

[20] Y. V. Stadnik, *Manifestations of Dark Matter and Variations of the Fundamental Constants in Atoms and Astrophysical Phenomena* (Springer Thesis, 2017), ISBN: 978-3-319-63417-3.

[21] L. Sharma, H. Rathore, S. Utreja, Neelam, A. Roy, S. De, and S. Panja, Proc. MAPAN Oct. 1 (2020).

[22] K. Beeks, T. Sikorsky, T. Schumm, J. Thielking, M. V. Okhapkin, and E. Peik, Nat Rev Phys **3**, 238 (2021).

[23] L. von der Wense and B. Seiferle, Eur. Phys. J. A **56**, 277 (2020).

[24] E Peik, T, Schumm, M. S. Safronova, A. Pálffy, J. Weitenberg, and P. G. Thirolf, Quantum Sci. Technol. **6** 034002 (2021).

[25] P. Gutlich, E. Bill, A.X. Trautwein, *Mössbauer Spectroscopy and Transition Metal Chemistry*, Springer: Berlin/Heidelberg, Germany, (2011).

[26] G. Principi, Metals **10**, 992 (2020).

[27] J. E. Moody and F. Wilczek, Phys. Rev. D **30**, 130 (1984).

[28] B. A. Dobrescu and I. Mocioiu, JHEP **2006**, 005 (2006).

[29] F. Ficek, P. Fadeev, V. V. Flambaum, D. F. J. Kimball, M. G. Kozlov, Y. V. Stadnik, and D. Budker, Phys. Rev. Lett. **120**, 183002 (2018).

[30] B. M. Henson, J. A. Ross, K. F. Thomas, C. N. Kuhn, D. K. Shin, S. S. Hodgman, Yong-Hui Zhang, Li-Yan Tang, G. W. F. Drake, A. T. Bondy, A. G. Truscott, K. G. H. Baldwin, Science **376**, 199 (2022).

[31] C. W. F. Everitt, et. al., Phys. Rev. Lett. **106**, 221101 (2011).

[32] Pavel Fadeev, Chris Timberlake, Tao Wang, Andrea Vinante, Yehuda Band, Dmitry Budker, Alexander Sushkov, Hendrik Ulbricht, and Derek F. Jackson Kimball, Quantum Sci. Technol. **6**, 024006 (2021).

[33] D. F. Jackson Kimball, A. O. Sushkov, and D. Budker, Phys. Rev. Lett. **116**, 190801 (2016).

[34] Pavel Fadeev, Tao Wang, Yehuda Band, Dmitry Budker, Peter W. Graham, Alexander O Sushkov, Derek F. Jackson Kimball, Phys. Rev. D **103**, 044056 (2021).

[35] T. Wang, S. Lourette, S. R. O'Kelley, M. Kayci, Y. B. Band, D. F. Jackson Kimball, A. O. Sushkov, and D. Budker, Phys. Rev. Appl. **11**, 044041 (2019).

[36] A. Vinante, P. Falferi, G. Gasbarri, A. Setter, C. Timberlake, and H. Ulbricht, Phys. Rev. Applied **13**, 064027 (2020).

Chapter 1

Time-reversal invariance violation in neutron-nucleus scattering

Phys. Rev. C **100**, 015504 (2019)

Pavel Fadeev[1] and Victor V. Flambaum [1,2]

[1] *Helmholtz Institute Mainz, Johannes Gutenberg University, 55099 Mainz, Germany*
[2] *School of Physics, University of New South Wales, Sydney, New South Wales 2052, Australia*

Parity (P) and time-reversal (T) violating effects are enhanced a million times in neutron reactions near p-wave nuclear compound resonances. Planning and interpretation of corresponding experiments require values of the matrix elements of the T,P-violating nuclear forces between nuclear compound states. We calculate the root-mean-square values and the ratio of the matrix elements of the T,P-violating and P-violating interactions using statistical theory based on the properties of chaotic compound states. We present the results in terms of the fundamental parameters in five different forms: in terms of the constants of the contact nuclear interaction, meson exchange constants, QCD θ-term, quark chromo-electric dipole moments $\tilde{d}_u$ and $\tilde{d}_d$, and axion interaction constants. Using current limits on these parameters, we obtain upper bounds on the ratio of the matrix elements and on the ratio of T,P-violating and P-violating parts of the neutron reaction cross sections. Our results confirm that the expected sensitivity in neutron-reactions experiments may be sufficient to improve the limits on the T,P-violating interactions.

1.1 Introduction

A very popular way to search for time-reversal (T) and parity (P) violation and to test unification theories is based on the measurements of electric dipole moments (EDMs) of elementary particles and atomic systems. So far this method has produced stringent limits on EDMs which exclude or bound many models (see reviews in Refs. [1–5]). Studies of T,P-violating (also known as T,P-odd) effects via EDM also give limits on the axion and relaxion interactions [6]. An efficient alternative method is measurement of T,P-odd effects in neutron-nucleus scattering. This method is motivated by the millionfold enhancement of parity violation in neutron reactions near p-wave nuclear compound resonances, which was predicted

in Refs. [7–10]. The first confirmation was obtained in experiments performed at the Joint Institute for Nuclear Research in Dubna [11, 12]; then a very extensive experimental study was done in several laboratories, including the Joint Institute for Nuclear Research (Dubna), Petersburg Institute of Nuclear Physics, KEK (Tsukuba), and especially in Los Alamos (see reviews in Refs. [13, 14]). This activity continues now (see, for example, the recent experimental paper [15] and references therein). A similar mechanism of enhancement should work for the T,P-odd effects [16–19]. An unusual statistics of P-violating and T,P-violating effects, namely random-sign observables not vanishing upon averaging, was demonstrated in Refs. [20, 21]. Experiments searching for T,P-violating effects are in progress in Japan and the United States [15, 22–26].

Without any enhancement, the effects of P violation in low-energy nuclear reactions are extremely small, $\sim 10^{-7}$ (e.g., in the proton scattering on hydrogen and helium, and neutron radiative capture by protons) [27]. The formula for a P-violation effect near a p-wave compound resonance may be presented as [7–10] [1]

$$P \sim \frac{W_{sp}}{E_s - E_p}\sqrt{\frac{\Gamma_s^n}{\Gamma_p^n}}\,, \tag{1.1}$$

where W_{sp} is the matrix element of the parity-violating interaction mixing s and p resonances, $E_s - E_p$ is the energy interval between these resonances, and Γ_s^n, Γ_p^n are the neutron widths of these resonances. We see that there are two reasons for the enhancement of P violation near p-wave compound resonances. First, in a nucleus excited by neutron capture the interval $E_s - E_p$ between the chaotic compound states (resonances) of opposite parity is very small, and this enhances by three orders of magnitude the mixing of these states by the weak P-violating interaction between nucleons. The second reason is that the admixture of opposite-parity states allows neutron capture in the s wave to contribute to the p-wave resonance. At small neutron energies the s-wave amplitude is three orders of magnitude larger than the p-wave amplitude ($\sqrt{\Gamma_s^n/\Gamma_p^n} \sim 10^3$). As a result of these two 10^3 factors, the P-violating parts reach 1–10% of reactions' cross sections and become accessible to experimental scrutiny. T,P-violating effects are also produced by the parity-violating interaction; therefore, Eq. (1.1) and the enhancement mechanism works for them too [16–19].

For the experiments to produce useful results we need theory for their interpretation. At first glance, it seems impossible, since chaotic compound states are very complicated. However, chaos allows us to develop a statistical theory, similar to the Maxwell-Boltzmann theory for macroscopic systems, which actually gives very accurate predictions. We developed such a theory, including a method to calculate matrix elements between chaotic states in finite systems (in excited nuclei, atoms, and molecules) [28–34]. We briefly present the ideas below.

An increase in the excitation energy of a nucleus increases the number of its active particles k and available orbitals p, leads to an exponential increase of the density of energy levels $\sim p!/[(p-k)!k!]$, and brings the system into a state where the residual interaction between particles exceeds the intervals between the energy levels. The eigenstates $|n\rangle = \sum_i C_i^n\,|i\rangle$ become chaotic superpositions of thousands or even millions of Hartree-Fock basic states $|i\rangle$. All medium and heavy nuclei and atoms with an open f shell have chaotic excited

[1] We omit the numerical coefficient which depends on the specific process induced by the neutron capture.

compound states in the discrete spectrum and/or chaotic compound resonances. The idea of Refs. [28, 29] is to treat the expansion coefficients C_i^n as Gaussian random variables, with the average values $\overline{C_i^n} = 0$ and variance

$$\overline{(C_i^n)^2} = \frac{1}{\bar{N}} \Delta(\Gamma_{spr}, E^n - E_i)\,, \tag{1.2}$$

$$\Delta(\Gamma_{spr}, E^n - E_i) = \frac{\Gamma_{spr}^2/4}{(E^n - E_i)^2 + \Gamma_{spr}^2/4}\,, \tag{1.3}$$

where $\bar{N} = \pi\Gamma_{spr}/2d$ is the normalization constant found from $\sum_i (C_i^n)^2 = 1$, d is the average energy distance between the compound states (resonances) with the same angular momentum and parity, and Γ_{spr} is the spreading width of the component calculated using the Fermi golden rule [35]; $\bar{N}$ is called the number of principal components.[2]

We have tested this distribution of C_i^n by the numerical calculations of chaotic compound states in cerium and protactinium atoms [36–42], in highly charged ions with an open f shell [43–48], in the two-body random interaction model [49–52] and using an analytical approach [33, 53].

The function $\overline{(C_i^n)^2} = \Delta(\Gamma_{spr}, E^n - E_i)/\bar{N}$ gives the probability to find the basis component $|i\rangle$ in the compound state $|n\rangle$; i.e. it plays the role of the statistical partition function. The difference from the conventional statistical theory is that the partition function depends on the total energy of the isolated system E^n instead of on the temperature of a system in a thermostat [recall the Boltzmann factor $\exp(-E_i/T)$]. One may compare this with the microcanonical distribution where the equipartition is assumed within the shell of the states with fixed energy E_i.

Expectation values of matrix elements of any operator W in a chaotic compound state are found as $\overline{|\langle n|\ W\ |n\rangle|^2} = \sum_i \overline{(C_i^n)^2}\ |\langle i|\ W\ |i\rangle|^2$. For example, this formula with $W = a_k^+ a_k$ (the occupation-number operator) gives the distribution of the orbital occupation numbers in finite chaotic systems which replaces the Fermi-Dirac (or Bose-Einstein) distribution.[3]

Average values of the non-diagonal matrix elements are equal to zero, $\overline{\langle n|\ W\ |m\rangle} = 0$, while the average values of the squared matrix elements $W^2 \equiv \overline{|\langle n|\ W\ |m\rangle|^2} = \sum_{i,j} \overline{(C_i^n)^2 (C_j^m)^2}\ |\langle i|\ W\ |j\rangle|^2$ are reduced to the sum of matrix elements between the Hartree-Fock basis states $|\langle i|\ W\ |j\rangle|^2$, where W is any perturbation operator. The distribution of the matrix elements $\langle n|\ W\ |m\rangle$ is Gaussian with the variance given by the W^2.

For the correlator between two different operators (e.g., P-violating and T,P-violating) we obtain $\overline{\langle n|\ W_P\ |m\rangle\ \langle m|\ W_{T,P}\ |n\rangle} = \sum_{i,j} \overline{(C_i^n)^2 (C_j^m)^2}\ \langle i|\ W_P\ |j\rangle\ \langle j|\ W_{T,P}\ |i\rangle$ [28–32]. Note that our theory predicts the results averaged over several compound resonances.

We have done many tests comparing the statistical theory results for electromagnetic amplitudes [40], electron recombination rates [43–48, 54] and parity-violation effects [28, 29]

[2] Basis states $|i\rangle$ with shell-model energies E_i close to the energy of a compound state E^n (within the spreading width Γ_{spr}) have the highest weight ($\sim 1/\bar{N}$) and dominate in the normalization sum $\sum_i (C_i^n)^2 = 1$. The number of such states is $\bar{N}$.

[3] However, numerical calculations [36, 43, 44, 49] give occupation numbers which are close to the Fermi-Dirac distribution.

with the experimental data and with numerical simulations. For example, we obtained a thousandfold enhancement of the electron recombination rate with many highly charged tungsten ions due to the very dense spectrum of chaotic compound resonances [44–48, 54]. These results agree with all available experimental data and predict recombination rates for ions with a high ionization degree, where experiments are limited by existing techniques. Our results are important for thermonuclear reactors which are made from tungsten. Tungsten ions contaminate plasma and significantly affect the energy output.

Using the theory of chaotic nuclear compound resonances, we calculate in this paper the ratio w/v of the root-mean-square values of the matrix elements of the T,P-odd (w) and P-odd (v) matrix elements. We show the results in terms of the fundamental parameters in five different forms: in terms of the constants of the contact nuclear interaction, meson exchange constants, QCD θ-term, quark chromo-EDMs $\tilde{d}_u$ and $\tilde{d}_d$, and axion interaction constants. Using latest bounds on $\theta, \tilde{d}_u$ and $\tilde{d}_d$, and axion interaction constants we arrive at bounds on the magnitude of possible T violation. In the Conclusion section the results are compared with the expected experimental sensitivity to the T,P-violating effects.

1.2 P- and T,P-violating interactions

The ratio of the time-reversal-invariance violating (TRIV) and parity violating (PV) parts of the neutron nuclear cross sections induced by mixing of s- and p-wave nuclear compound resonances, $\Delta\sigma_{PT}/\Delta\sigma_P$, can be expressed as [15, 55, 56]:

$$\frac{\Delta\sigma_{PT}}{\Delta\sigma_P} = \kappa \frac{\langle\psi_p|W_{PT}|\psi_s\rangle}{\langle\psi_p|W_P|\psi_s\rangle}\,. \tag{1.4}$$

Here the factor κ includes amplitudes of the partial neutron widths which depend on spin channels $J = I \pm 1/2$, where I is the spin of the target nucleus and J is the spin of the compound resonance. For example, for $J = 0$, one obtains $\kappa = 1$, as in this case κ does not depend on neutron partial widths [16–18].

The ratio $\Delta\sigma_{PT}/\Delta\sigma_P$ for the neutron-deuterium scattering was calculated in Ref. [57]. However, experiments are planned for heavier nuclei where we expect a millionfold enhancement of the T,P-odd and P-odd effects.

In the short-range interaction limit, the PV operator W_P and TRIV operator W_{PT} are

$$W_P = \frac{Gg}{2\sqrt{2}m}\,\{(\sigma\mathbf{p}),\rho\}\,, \tag{1.5}$$

$$W_{PT} = \frac{G\eta}{2\sqrt{2}m}(\sigma\nabla)\rho\,. \tag{1.6}$$

Here G is the weak-interaction Fermi constant, m is the nucleon mass, $\mathbf{p}$ and σ are nucleon momentum and spin respectively, and ρ is the nucleon density. Nucleon dimensionless constants $g_{p,n}$ and $\eta_{p,n}$ characterize the strength of the interactions. Note that in the standard definition of angular wavefunctions the matrix element of W_P between bound states is imaginary (since the momentum operator $\mathbf{p} = -i\nabla$) and the matrix element of TRIV operator W_{PT} is real.

We define v^2 to be the average of the absolute value of the squared PV matrix element, and w^2 to be the average value of the squared TRIV matrix element between the s and p compound resonances, such that

$$v = \sqrt{\overline{\langle\psi_p|W_P|\psi_s\rangle \langle\psi_s|W_P|\psi_p\rangle}}\,, \tag{1.7}$$

$$w = \sqrt{\overline{\langle\psi_p|W_{PT}|\psi_s\rangle \langle\psi_s|W_{PT}|\psi_p\rangle}}\,. \tag{1.8}$$

Correlations might exist between the matrix elements of PV and TRIV interactions. The quantity parametrizing such correlations, the correlator, is defined as

$$C = \frac{|\overline{\langle\psi_p|W_P|\psi_s\rangle \langle\psi_s|W_{PT}|\psi_p\rangle}|}{v\,w}\,. \tag{1.9}$$

The correlator, which takes values between zero and one, can be useful to deduce the values and signs of TRIV effects, since much is already known about the PV effects. The correlator C was calculated by the same technique as the mean-square matrix element and was found to be [32]:

$$|\,C\,| \approx 0.1\,. \tag{1.10}$$

This result tells us that the correlations between the matrix elements are relatively small so we may neglect them.

1.2.1 Rough estimate of w/v

Naively one would expect from Eqs. (1.5) and (1.6) the following relation: $w/v \sim \eta/g$. However, this ratio is actually $A^{1/3}$ times smaller than the ratio of interaction constants [31], where A is the number of nucleons. Indeed, for $\nabla\rho$ in Eq. (1.6),

$$\nabla\rho \sim \frac{\rho}{R_N} \sim \frac{\rho}{r_0 A^{1/3}}\,, \tag{1.11}$$

where r_0 is the internucleon distance, and $R_N = r_0 A^{1/3}$ is the nuclear radius. The momentum in Eq. (1.5) is approximated as $p \sim p_F \sim \hbar/r_0$. Thus, the ratio of matrix elements is smaller than the ratio of interaction constants in Eqs. (1.5) and (1.6) by a factor of $A^{1/3}$:

$$\frac{w}{v} \sim \frac{\eta}{g A^{1/3}}\,. \tag{1.12}$$

For elements with the number of nucleons in the range 100–250, $A^{1/3} \approx 5$. A detailed discussion of this suppression factor including many-body effects can be found in Ref. [31].

1.2.2 Dependence of matrix elements on nucleon interaction constants

A general expression for the root-mean-square value of the matrix element v the PV operator (and the matrix element w of the TRIV operator) was derived in Ref. [29]:

$$v = \frac{1}{\sqrt{\bar{N}}} \left\{ \sum_{abcd} \nu_a \left(1-\nu_b\right) \nu_c \left(1-\nu_d\right) \frac{1}{4} \left| V_{ab,cd} - V_{ad,cb} \right|^2 \Delta \left(\Gamma_{spr}, \epsilon_a - \epsilon_b + \epsilon_c - \epsilon_d\right) \right\}^{\frac{1}{2}} . \tag{1.13}$$

Here ν are the orbital occupation numbers given by the Fermi-Dirac distribution in an excited nucleus, numerical values of the matrix elements of the two-nucleon interaction $V_{ab,cd}$ (see Fig. 1.1) are presented in Refs. [29, 32], and $\Delta\left(\Gamma_{spr}, \epsilon_a - \epsilon_b + \epsilon_c - \epsilon_d\right)$ is the "spread" δ function [Eq. (1.3)] of the change in energy $\epsilon_a - \epsilon_b + \epsilon_c - \epsilon_d$. Equation (1.13) has a clear interpretation. The Δ function means in fact an approximate energy conservation with an accuracy up to the spreading width Γ_{spr} (since the single-particle states are not stationary states in this problem). In the case $\Gamma_{spr} \to 0$ we have $\Delta\left(\Gamma_{spr}, \epsilon_a - \epsilon_b + \epsilon_c - \epsilon_d\right) \to (\pi\Gamma_{spr}/2)\delta(\epsilon_a - \epsilon_b + \epsilon_c - \epsilon_d)$. To have a transition, initial states must be occupied (this gives ν_a and ν_c) and final states empty (this gives $1-\nu_b$ and $1-\nu_d$).

The dependence of v and w on the nucleon interaction constants g and η [which appear in Eqs. (1.5) and (1.6)] can be presented in the following form [29, 32]:

$$v = \frac{1}{\sqrt{\bar{N}}} \sqrt{\left(\Sigma_{pp}^{(P)} g_p\right)^2 + \left(\Sigma_{nn}^{(P)} g_n\right)^2 + \left(\Sigma_{pn}^{(P)} g_p g_n\right)} , \tag{1.14}$$

$$w = \frac{1}{\sqrt{\bar{N}}} \sqrt{\left(\Sigma_{pp}^{(PT)} \eta_p\right)^2 + \left(\Sigma_{nn}^{(PT)} \eta_n\right)^2 + \left(\Sigma_{pn}^{(PT)} \eta_p \eta_n\right)} , \tag{1.15}$$

where g_p and g_n are proton and neutron weak constants — they characterize the strength of the P-odd weak potential; η_p, η_n are constants that characterize the strength of the T,P-odd potential, and Σ are sums of the weighted squared matrix elements of the weak interaction between nucleon orbitals defined in Eq. (1.13). Contributions of the cross terms $\Sigma_{pn}^{(P)} g_p g_n$ and $\Sigma_{pn}^{(PT)} \eta_p \eta_n$ are small compared to the other terms since they contain products of different matrix elements which have random signs, while in the terms containing squared interaction constants all contributions are positive.

Therefore, we can present v and w in the following form:

$$v = K_P \sqrt{g_n^2 + k g_p^2} , \tag{1.16}$$

$$w = K_{PT} \sqrt{\eta_n^2 + k \eta_p^2} . \tag{1.17}$$

The coefficient k should be slightly smaller than 1 since in heavy nuclei the number of neutrons $N = 1.5Z$, where Z is the number of protons. To make a simple estimate of the sensitivity of v and w to changes in the interaction constants, we assume in the next step that Σ from Eqs. (1.14) and (1.15) are proportional to the number of interaction terms in the nucleus. There are $Z^2/2$ interaction terms between protons, $N^2/2$ such terms between neutrons, and ZN terms between a proton and a neutron (Fig. 1.1). Thus we can write

$$k = \frac{Z^2 + 2ZN}{N^2 + 2ZN} = 0.76 . \tag{1.18}$$

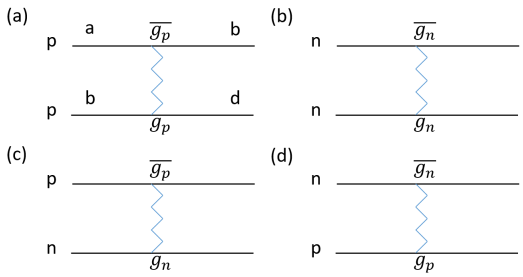

Figure 1.1: *Possible configurations of weak interactions $V_{ab,cd}$ [29] within the nucleus between protons (p) and neutrons (n). In each diagram, the upper vertex is P-violating. Constants g_p and g_n characterize the strength of the interactions. (a) Interactions between two protons; (b) interactions between two neutrons; (c) and (d) interactions between protons and neutrons, which contribute to the squared PV matrix element v^2 by $(V_{np}+V_{pn})^2 = V_{np}^2+V_{pn}^2+2V_{np}V_{pn}$. When summing matrix elements in (c) and (d), the terms $V_{np}V_{pn}$ have random signs and the result is much smaller than the sums of V_{np}^2 and V_{pn}^2.*

Numerical calculations of v and w have been done in Refs. [29–32] for specific values of the interaction constants g_p, g_n, η_p and η_n. The values of these constants have been updated since those calculations. Therefore, we would like to find updated values of these constants to insert into Eqs. (1.16) and (1.17). The general expressions for g_p and g_n are [28, 58–60]

$$g_p = 2\times10^5\, W_\rho\left[176\frac{W_\pi}{W_\rho}f_\pi - 19.5h_\rho^0 - 4.7h_\rho^1 + 1.3h_\rho^2 - 11.3(h_\omega^0+h_\omega^1)\right], \tag{1.19}$$

$$g_n = 2\times10^5\, W_\rho\left[-118\frac{W_\pi}{W_\rho}f_\pi - 18.9h_\rho^0 + 8.4h_\rho^1 - 1.3h_\rho^2 - 12.8(h_\omega^0+h_\omega^1)\right], \tag{1.20}$$

where f and h are the weak NN-meson couplings, and W_ρ and W_π are constants which account for the repulsion between nucleons at small distances as well as for the finite range of the interaction potential. We take $W_\rho = 0.4$ and $W_\pi = 0.16$ as in Refs. [58, 60].

For the choice of constants $g_p = 4, g_n = 1$ [61], numerical calculations give [29]

$$v = K_P\sqrt{1+16k} = 2.08\,\text{meV}\,. \tag{1.21}$$

We calculate updated values for g_p and g_n, using the best values of the constants h from Desplanques, Donoghue, and Holstein (DDH) [59] with an updated $f_\pi \equiv h_\pi^1$, which was recently derived by lattice QCD methods [62, 63]. Such calculations give $g_p = 2.6\,, g_n = 1.5$ (Table 4.1). Using these values with Eq. (1.21), we have

$$v_{updated} = 2.08\,\text{meV}\frac{\sqrt{1.5^2+2.6^2k}}{\sqrt{1+16k}} = 1.56\,\text{meV}\,, \tag{1.22}$$

where in the last step we used $k = 0.76$.[4] This theoretical estimate is in excellent agreement with the experimental value $1.39^{+0.55}_{-0.38}$ meV [64, 65].

[4] For $k = 1$ we would get 1.51 meV. Thus we see that our result is not very sensitive to the value of k.

Numerical calculations were done for $\eta_p = \eta_n$ and gave $w = 0.2|\eta_n|$ meV [32]. Using this result and Eq. (1.17) we obtain

$$w_{updated} = 0.15\,\text{meV}\sqrt{\eta_n^2 + 0.76\eta_p^2}\,. \tag{1.23}$$

Reference	g_p	g_n
DDH (1980) [59, 60]	4.5	0.2
ND (1986) [29, 61]	4	1
DZ (1986) [66]	2.4	1.1
FCDH (1991) [67]	2.7	−0.1
Wasem (2012) [63]	2.6	1.5
NPDGamma (2018) [68]	3.4	0.9

Table 1.1: *Values of g_p and g_n based on the meson exchange constants from different publications (left-hand column): Desplanques, Donoghue, and Holstein (DDH) [59, 60]; Noguera and Desplanques (ND) [61]; Dubovik and Zenkin (DZ) [66]; Feldman, Crawford, Dubach, and Holstein (FCDH) [67]. In the line of Wasem [63] we use the best DDH values for all the values of h except $f_\pi = h^1_\pi$, which was recently derived by the lattice QCD methods [62, 63] to be $h^1_\pi = 1.1 \cdot 10^{-7}$. Recent experiment measuring P-violation in the neutron radiative capture by proton [68] gave $h^1_\pi = [2.6 \pm 1.2(stat.) \pm 0.2(sys.)] \times 10^{-7}$ which is larger than the theoretical estimate $h^1_\pi = 1.1 \cdot 10^{-7}$. Using this experimental value, and the rest from DDH, gives slightly larger $g_p = 3.4 \pm 0.8$ and smaller $g_n = 0.9 \pm 0.6$ which are close to the values $g_p = 4$ and $g_n = 1$ used in the numerical calculation of P-violation in Ref. [29]. Corresponding value of the matrix element $v = 1.8 \pm 0.4$ meV is consistent with both Eq. (1.21) and Eq. (1.22).*

1.2.3 The ratio w/v expressed via meson exchange constants, QCD θ-term, quark chromo-EDMs $\tilde{d}_u$ and $\tilde{d}_d$, and axion exchange constants

Now we can express the ratio w/v in five different ways: as a function of η_p, η_n, by π_0 meson-exchange coupling constants with the nuclei, by QCD CP-violation parameter θ, by quark chromo-EDMs, and finally by axion exchange constants.

First, to express the ratio w/v as a function of η, we use Eqs. (1.22) and (1.23) to obtain

$$\frac{w}{v} = 0.10\sqrt{\eta_n^2 + 0.76\eta_p^2}\,. \tag{1.24}$$

If, following Refs. [32, 69], we take $|\eta_p| = |\eta_n|$, the ratio in Eq. (1.24) becomes

$$\frac{w}{v} = 0.13|\eta_n|\,. \tag{1.25}$$

Second, the T,P-odd nuclear forces are dominated by π_0 meson exchange. Such an ex-

change is described by the interaction [70–72]

$$\mathcal{W}(\boldsymbol{r}_1-\boldsymbol{r}_2)=-\frac{\bar{g}}{8\pi m_N}\left[\nabla_1\left(\frac{e^{-m_\pi r_{12}}}{r_{12}}\right)\right]\cdot\{(\boldsymbol{\sigma}_1-\boldsymbol{\sigma}_2) \times\left[\bar{g}_0\boldsymbol{\tau}_1\cdot\boldsymbol{\tau}_2+\bar{g}_2\left(\boldsymbol{\tau}_1\cdot\boldsymbol{\tau}_2-3\tau_{1z}\tau_{2z}\right)\right]+\bar{g}_1\left(\tau_{1z}\boldsymbol{\sigma}_1-\tau_{2z}\boldsymbol{\sigma}_2\right)\}\,, \tag{1.26}$$

where $\bar{g}=13.6$ is the strong-force T,P-conserving πNN coupling constant, $\bar{g}_0,\bar{g}_1$, and $\bar{g}_2$, are the strengths of the isoscalar, isovector, and isotensor T,P-violating couplings, respectively, m_N is the nucleon mass, m_π is the pion mass, $\boldsymbol{\sigma}$ is the nucleon spin, $\boldsymbol{\tau}$ is the nucleon Pauli isospin matrix in vector form, and r_{12} is the separation between nucleons. The coupling constants η can be expressed in terms of $\bar{g}$ [69]:

$$-\eta_p=\eta_n=5\times10^6\bar{g}\left(\bar{g}_1+0.4\bar{g}_2-0.2\bar{g}_0\right)\,. \tag{1.27}$$

Then we have

$$\frac{w}{v}=0.13|\eta_n|=|6.5\times10^5\bar{g}\left(\bar{g}_1+0.4\bar{g}_2-0.2\bar{g}_0\right)|\,. \tag{1.28}$$

Third, using the previous results $\bar{g}\bar{g}_0=-0.37\theta$ [73] ,where θ is the QCD CP-violation parameter, and $\bar{g}\bar{g}_1=\bar{g}\bar{g}_2=0$, we can write the ratio w/v as a function of θ:

$$\frac{w}{v}=4.8\times10^4|\theta|\,. \tag{1.29}$$

Using updated results [4, 74]

$$\bar{g}\bar{g}_0=-0.2108\,\theta\,, \tag{1.30}$$
$$\bar{g}\bar{g}_1=46.24\times10^{-3}\theta\,, \tag{1.31}$$

we can write, still with $\bar{g}\bar{g}_2=0$,

$$\frac{w}{v}=5.7\times10^4|\theta|\,.$$

Using the current limit on θ, obtained from constraints on neutron EDM, $|\theta|<10^{-10}$ [4], we obtain

$$w/v<10^{-5}\,. \tag{1.32}$$

Fourth, we can connect our result to the quark chromo-EDM $\tilde{d}$ [2]:

$$\bar{g}\bar{g}_1=4\times10^{15}\left(\tilde{d}_u-\tilde{d}_d\right)/\mathrm{cm}\,, \tag{1.33}$$
$$\bar{g}\bar{g}_0=0.8\times10^{15}\left(\tilde{d}_u+\tilde{d}_d\right)/\mathrm{cm}\,. \tag{1.34}$$

Then

$$\frac{w}{v}=|\,6.5\times10^{20}\left(4\left(\tilde{d}_u-\tilde{d}_d\right)-0.16\left(\tilde{d}_u+\tilde{d}_d\right)\right)|\,/\mathrm{cm}\,. \tag{1.35}$$

Using the current limits (Table IV in [75]; see also Ref. [76])

$$|\tilde{d}_u - \tilde{d}_d| < 6 \times 10^{-27}\text{cm}\,, \tag{1.36}$$

$$|\frac{1}{2}\tilde{d}_u + \tilde{d}_d| < 3 \times 10^{-26}\text{cm}\,, \tag{1.37}$$

we obtain

$$w/v < 2 \times 10^{-5}\,. \tag{1.38}$$

Finally, a T,P-violating interaction, similar to the pion-exchange-induced Eq. (1.26), may be due to exchange by any scalar particle which has both scalar (with the interaction constant g^s) and pseudoscalar (with the interaction constant g^p) couplings to nucleons. The most popular examples are the dark-matter candidates axion [77, 78] and relaxion [79–81], which have very small masses.[5] A numerical estimate shows that due to the long range of the interaction the matrix elements in the small-mass case ($e^{-mr} \approx 1$) are ~ 1.5 times larger than the pion exchange matrix elements; i.e., we have instead of Eq. (1.28) the following estimate:

$$\frac{w}{v} \sim |1 \times 10^6 g^s g^p|\,. \tag{1.39}$$

The limit on $g^s g^p$ may be obtained from the proton EDM calculation,[6]

$$d_p = \frac{g^s g^p e}{8\pi^2 m_p}\,, \tag{1.40}$$

and measurement [76], $|d_p| < 2 \times 10^{-25} e$ cm, $|g^s g^p| < 1 \times 10^{-9}$. Using limits from the proton EDM and the ^{199}Hg nuclear-Schiff-moment measurements in Ref. [75], the authors of Ref. [82] concluded that the limit on $|g^s g^p|$ is between 10^{-9} and 10^{-11}. This gives a rather weak limit on w/v induced by axion exchange:

$$w/v < 10^{-3} - 10^{-5}\,. \tag{1.41}$$

1.3 Conclusion

Using the bound in Eq. (1.38), and assuming $\kappa \approx 1$ in Eq (1.4) (which is reasonable [55] and matches experimental results [15, 26]), we arrive at

$$\frac{\Delta\sigma_{PT}}{\Delta\sigma_P} \lesssim 2 \times 10^{-5}\,. \tag{1.42}$$

The limit based on the axion exchange in Eq. (1.41) is weaker. The vurrent expected experimental sensitivity is [26, 83]

$$\frac{\Delta\sigma_{PT}}{\Delta\sigma_P}_{\text{exp. sensitivity}} < 10^{-6}\,. \tag{1.43}$$

Thus we confirm that the expected experimental sensitivity in neutron reactions may be sufficient to improve the limits on the TRIV interactions, or possibly to detect them.

[5] The limits on the T,P-violating electron-nucleon interactions mediated by the axion or relaxion exchange from EDM measurements were obtained in Ref. [6], where more references may be found.

[6] The calculation is similar to that for electron EDM [6].

Acknowledgments

We thank Anne Fabricant for editing the manuscript. We are grateful to William Michael Snow for informing us about the new measurement of the constant h_π^1 [68]. This work is supported by the Australian Research Council and Gutenberg Fellowship.

Bibliography

[1] J. S. M. Ginges and V. V. Flambaum, Phys. Rep. **397**, 63 (2004).

[2] M. Pospelov and A. Ritz, Ann. Phys. **318**, 119 (2005).

[3] J. Engel, M. J. Ramsey-Musolf, U. van Kolck, Prog. Part. Nucl. Phys. **71**, 21–74 (2013).

[4] N. Yamanaka, B. K. Sahoo, N. Yoshinaga, T. Sato, K. Asahi, and B. P. Das, Eur. Phys. J. A **53**, 54 (2017).

[5] T.E. Chupp, P. Fierlinger, M.J. Ramsey-Musolf, and J.T. Singh, Rev. Mod. Phys. **91**, 015001 (2019).

[6] Y. V. Stadnik, V. A. Dzuba, and V. V. Flambaum, Phys. Rev. Lett. **120**, 013202 (2018).

[7] O. P. Sushkov and V. V. Flambaum, Pis'ma Zh. Eksp. Teor. Fiz. **32**, 377 (1980) [JETP Lett. **32**, 352 (1980)].

[8] O. P. Sushkov and V. V. Flambaum, Usp. Fiz. Nauk. **136** (1), 3, (1982) [Sov. Phys. Usp. 25, 1 (1982)].

[9] V. V. Flambaum and O. P. Sushkov, Nucl. Phys. A **412**, 13 (1984).

[10] V. V. Flambaum and O. P. Sushkov, Nucl. Phys. A **435**, 352 (1985).

[11] V. P. Alfimenkov, S. B. Borzakov, Vo Van Tkhuan„ Yu. D. Mareev, L. B. Pikelner, A. S. Khrykin, and E. I. Sharapov, Nucl. Phys. A **398**, 93 (1983).

[12] V. P. Alfimenkov, S. B. Borzakov, Vo Van Tkhuan„ Yu. D. Mareev, L. B. Pikel'ner, I. M. Frank, A. S. Khrykin, and E. I. Sharapov, Pis'ma Zh. Eksp. Teor. Fiz. **39**, 346 (1984) [JETP Lett. **39**, 416 (1984)].

[13] G. E. Mitchell, J. D. Bowman, S. I. Penttilä, E. I. Sharapov, Phys. Rep. **354**, 157 (2001).

[14] G. E. Mitchell, J. D. Bowman, and H. A. Weidenmöller, Rev. Mod. Phys. **71**, 445 (1999).

[15] T. Okudaira, S. Takada, K. Hirota, A. Kimura, M. Kitaguchi, J. Koga, K. Nagamoto, T. Nakao, A. Okada, K. Sakai, H. M. Shimizu, T. Yamamoto, and T. Yoshioka, Phys. Rev. C **97**, 034622 (2018).

[16] V. E. Bunakov and V. P. Gudkov, Nucl. Phys. A **401**, 93 (1983).

[17] V. E. Bunakov and V. P. Gudkov, *Tests of Time Reversal Invariance in Neutron Physics*, edited by N. R. Roberson, C. R. Gould, and J. D. Bowman (World Scientific, Singapore, 1987), pp. 175–183.

[18] V. P. Gudkov, Phys. Rep. **212**, 77 (1992).

[19] V. V. Flambaum and G. F. Gribakin, Prog. Part. Nucl. Phys. **35**, 423 (1995).

[20] V. V. Flambaum and G. F. Gribakin, Phys. Rev. C **50**, 3122 (1994).

[21] J. C. Berengut, V. V. Flambaum, and G. F. Gribakin, Phys. Rev. C **62**, 024610 (2000).

[22] Numerous review articles appear in *Parity and Time Reversal Violation in Compound States and Related Topics*, edited by N. Auerbach and J.D. Bowman (World Scientific, Singapure, 1996).

[23] A. G. Beda and V. R. Skoy, Phys. Part. Nucl. **38**, 1063 (2007).

[24] W. M. Snow, *Null Tests of Time Reversal Invariance Using Neutrons*, Proc. Sci. **294**, 007 (2017).

[25] M. Kitaguchi, K. Asahi, S. Endo, C. C. Haddock, M. Hino, K. Hirota, T. Ino, I. Ito, T. Iwata, J. Koga, Y. Miyachi, T. Momose, N. Oi, T. Okudaira, K. Sakai, T. Shima, H. M. Shimizu, S. Takada, Y. Yamagata, T. Yamamoto, and T. Yoshioka, JPS Conf. Proc. **22**, 011034 (2018).

[26] L. B. Palos (NOPTREX Collaboration), talk at Thirteenth Conference on the Intersections of Particle and Nuclear Physics (2018). https://conferences.lbl.gov/event/137/session/18/ contribution/139/material/slides/0.pdf.

[27] M. T. Gericke, R. Alarcon, S. Balascuta, L. Barrón-Palos, C. Blessinger, J. D. Bowman, R. D. Carlini, W. Chen, T. E. Chupp *et al.*, Phys. Rev. C **83**, 015505 (2011).

[28] V. V. Flambaum, Phys. Scripta. **T46**, 198 (1993).

[29] V. V. Flambaum and O. K. Vorov, Phys. Rev. Lett. **70**, 4051 (1993).

[30] V. V. Flambaum and O. K. Vorov, Phys. Rev. C **49**, 1827, (1994).

[31] V. V. Flambaum and O. K. Vorov, Phys. Rev. C **51**, 1521 (1995).

[32] V. V. Flambaum and O. K. Vorov, Phys. Rev. C**51**, 2914 (1995).

[33] V. V. Flambaum and G. F. Gribakin, Philos. Mag. B **80**, 2143 (2000).

[34] V. V. Flambaum in *Parity and Time Reversal Violation in Compound States and Related Topics*, edited by N. Auerbach and J.D. Bowman (World Scientific, Singapure, 1996), pp. 41-64.

[35] A. Bohr and B. Mottelson, *Nuclear Structure* (Benjamin, New York, 1969), Vols. 1 and 2.

[36] V. V. Flambaum, A. A. Gribakina, G. F. Gribakin, and M. G.Kozlov, Phys. Rev. A **50**, 267, (1994).

[37] A. A. Gribakina, V. V. Flambaum, and G. F. Gribakin, Phys. Rev. E **52**, 5667 (1995).

[38] V. V. Flambaum, A. A. Gribakina, and G. F. Gribakin, Phys. Rev. A, **54**, 2066 (1996).

[39] V. V. Flambaum, A. A. Gribakina, G. F. Gribakin, and I. V. Ponomarev, Phys. Rev. E **57**, 4933 (1998).

[40] V. V. Flambaum, A. A. Gribakina, and G. F. Gribakin, Phys. Rev. A **58**, 230 (1998).

[41] V. V. Flambaum, A. A. Gribakina, G. F. Gribakin, and I. V. Ponomarev, Physica D **131**, 205 (1999).

[42] A. V. Viatkina, M. G. Kozlov, and V. V. Flambaum, Phys. Rev. A **95**, 022503 (2017).

[43] G. F. Gribakin, A. A. Gribakina, and V. V. Flambaum, Aust. J. Phys. **52**, 443 (1999).

[44] V. V. Flambaum, A. A. Gribakina, G. F. Gribakin, and C. Harabati, Phys. Rev. A **66**, 012713 (2002).

[45] V. A. Dzuba, V. V. Flambaum, G. F. Gribakin, and C. Harabati, Phys. Rev. A **86**, 022714 (2012).

[46] V. A. Dzuba, V. V. Flambaum, G. F. Gribakin, C. Harabati, and M. G. Kozlov, Phys. Rev. A **88**, 062713 (2013).

[47] J. C. Berengut, C. Harabati, V. A. Dzuba, V. V. Flambaum, and G. F. Gribakin, Phys. Rev. A **92**, 062717 (2015).

[48] C. Harabati, J. C. Berengut, V. V. Flambaum, and V. A. Dzuba, J. Phys. B **50**, 125004 (2017).

[49] V. V. Flambaum, F. M. Izrailev, and G. Casati, Phys. Rev. E **54**, 2136 (1996).

[50] V. V. Flambaum and F. M. Izrailev, Phys. Rev. E **55**, R13 (R) (1997).

[51] V. V. Flambaum and F. M. Izrailev, Phys. Rev E **56**, 5144 (1997).

[52] V. V. Flambaum and F. M. Izrailev, Phys. Rev. E **61**, 2539 (2000).

[53] V. V. Flambaum, G. F. Gribakin, and F. M. Izrailev, Phys. Rev. E **53**, part A, 5729 (1996).

[54] V. V. Flambaum, M. G. Kozlov, and G. F. Gribakin, Phys. Rev. A **91**, 052704 (2015).

[55] V. Gudkov and H. M. Shimizu, Phys. Rev. C **97**, 065502 (2018).

[56] V. P. Gudkov, Phys. Lett. B **243**, 319 (1990).

[57] Y.-H. Song, R. Lazauskas, and V. Gudkov, Phys. Rev. C **83**, 015501 (2011).

[58] V. V. Flambaum, I. B. Khriplobich, and O. P. Sushkov, Phys. Lett. B **146**, 367 (1984).

[59] B. Desplanques, J. F. Donoghue, and B. R. Holstein, Ann. Phys. (N.Y.) **124**, 449 (1980).

[60] V. V. Flambaum and D. W. Murray, Phys. Rev. C **56**, 1641 (1997).

[61] S. Noguera and B. Desplanques, Nucl. Phys. A **457**, 189 (1986).

[62] W. Haxton and B. Holstein, Prog. Part. Nucl. Phys. **71**, 185 (2013).

[63] J. Wasem, Phys. Rev. C **85**, 022501(R) (2012).

[64] J. D. Bowman, C. D. Bowman, J. E. Bush, P. P. J. Delheij, C. M. Frankle, C. R. Gould, D. G. Haase, J. Knudson, G. E. Mitchell *et al.*, Phys. Rev. Lett. **65**, 1192 (1990).

[65] C. M. Frankle, J. D. Bowman, J. E. Bush, P. P. J. Delheij, C. R. Gould, D. G. Haase, J. N. Knudson, G. E. Mitchell, S. Penttilä, H. Postma, N. R. Roberson, S. J. Seestrom, J. J. Szymanski, S. H. Yoo, V. W. Yuan, and X. Zhu, Phys. Rev. Lett. **67**, 564 (1991).

[66] V. M. Dubovik and S. V. Zenkin, Ann. Phys (N.Y.) **172**, 100 (1986).

[67] G. B. Feldman, G. A. Crawford, J. Dubach, and B. R. Holstein, Phys. Rev. C **43**, 863 (1991).

[68] D. Blyth et al. (NPDGamma Collaboration), Phys. Rev. Lett. **121**, 242002 (2018).

[69] V. V. Flambaum, D. DeMille, and M. G. Kozlov, Phys. Rev. Lett. **113**, 103003 (2014).

[70] W. C. Haxton and E. M. Henley, Phys. Rev. Lett. **51**, 1937 (1983).

[71] I. B. Khriplovich, and R. V. Korkin, Nucl. Phys. A **665**, 365 (2000).

[72] V. F. Dmitriev, and R. A. Sen'kov, Phys. At. Nucl. **66**, 1940 (2003).

[73] R. J. Crewther, P. di Vecchia, G. Veneziano, and E. Witten, Phys. Lett. B **91**, 487 (1980).

[74] J. de Vries, E. Mereghetti, and A. Walker-Loud, Phys. Rev. C **92**, 045201 (2015).

[75] M. D. Swallows, T. H. Loftus, W. C. Griffith, B. R. Heckel, E. N. Fortson, and M. V. Romalis, Phys. Rev. A **87**, 012102 (2013).

[76] B. Graner, Y. Chen, E. G. Lindahl, and B. R. Heckel, Phys. Rev. Lett. **116**, 161601 (2016).

[77] J. E. Moody and F. Wilczek, Phys. Rev. D **30**, 130 (1984).

[78] D. J. Marsh, Phys. Rep. **643**, 1 (2016).

[79] P.W. Graham, D. E. Kaplan, and S. Rajendran, Phys. Rev. Lett. **115**, 221801 (2015).

[80] R. S. Gupta, Z. Komargodski, G. Perez, and L. Ubaldi, J. High Energy Phys. 02 (2016) 166.

[81] T. Flacke, C. Frugiuele, E. Fuchs, R. S. Gupta, and G. Perez, J. High Energy Phys. 06 (2017) 050.

[82] S. Mantry, M. Pitschmann, and M. J. Ramsey-Musolf, Phys. Rev. D **90**, 054016 (2014).

[83] J. D. Bowman and V. Gudkov, Phys. Rev. C **90**, 065503 (2014).

Chapter 2

Sensitivity of ^{229}Th nuclear clock transition to variation of the fine-structure constant

Phys. Rev. C **102**, 052833 (2020)

Pavel Fadeev[1], Julian C. Berengut[2], and Victor V. Flambaum [1,2]

[1] *Helmholtz Institute Mainz, Johannes Gutenberg University, 55099 Mainz, Germany*
[2] *School of Physics, University of New South Wales, Sydney, New South Wales 2052, Australia*

Peik and Tamm [Europhys. Lett. **61**, 181 (2003)] proposed a nuclear clock based on the isomeric transition between the ground state and the first excited state of thorium-229. This transition was recognized as a potentially sensitive probe of possible temporal variation of the fine-structure constant, α. The sensitivity to such a variation can be determined from measurements of the mean-square charge radius and quadrupole moment of the different isomers. However, current measurements of the quadrupole moment are yet to achieve an accuracy high enough to resolve non-zero sensitivity. Here we determine this sensitivity using existing measurements of the change in the mean-square charge radius, coupled with the ansatz of constant nuclear density. The enhancement factor for α variation is $K = -(0.82 \pm 0.25) \times 10^4$. For the current experimental limit, $\delta\alpha/\alpha \lesssim 10^{-17}$ per year, the corresponding frequency shift is $\sim$200 Hz per year. This shift is six orders of magnitude larger than the projected accuracy of the nuclear clock, paving the way for increased accuracy of the determination of $\delta\alpha$ and interaction strength with low-mass scalar dark matter. We verify that the constant-nuclear-density ansatz is supported by nuclear theory and propose how to verify it experimentally. We also consider a possible effect of the octupole deformation on the sensitivity to α variation, and calculate the effects of α variation in a number of Mössbauer transitions.

2.1 Introduction

The first excited isomeric state of thorium-229, ^{229m}Th, is a candidate for the first nuclear optical clock [1]. This is due to the state's low excitation energy of several electron-volts [2–5] (the lowest of all known isomeric states) and long radiative lifetime of up to 10^4 seconds [6, 7]. Several theoretical and experimental groups are making rapid progress toward using ^{229m}Th as

a reference for a clock with unprecedented accuracy [8–16]. These papers proposed specific experimental schemes for the nuclear clocks and performed detailed studies of systematic effects such as the black body radiation shifts, effects of the ion trapping fields in ion traps, and effects of the stray fields. The advantage of the nuclear clock in comparison with atomic clocks is that, due to the very small size of the nucleus and its shielding by the atomic electrons, it is insensitive to many systematic effects. For example, the nuclear polarizability and its contribution to the major systematic effect, the black body radiation shift, are 15 orders of magnitude smaller than in atomic transitions. Nuclear clocks may perform at a level of accuracy of 10^{-19} [9], 1–2 orders of magnitude higher than the accuracy of the best existing atomic clocks.

In a recent crucial step towards this goal, the transition was measured using spectroscopy of the internal conversion electrons emitted in flight during the decay of neutral ^{229m}Th atoms [17], yielding an excitation energy $E_{is} = 8.28\,(17)$ eV. Another approach, using γ-ray spectroscopy at 29.2 keV, obtained $E_{is} = 8.30\,(92)$ eV [18, 19]. More recently, $E_{is} = 8.10\,(17)$ eV was reported [20].

The ^{229m}Th nuclear clock is expected to be a sensitive probe for time variation of the fundamental constants of nature [21]. To avoid dependence on units we consider the effect of variation of the dimensionless fine-structure constant, α, related to the electromagnetic interaction [21–26]. Another dimensionless parameter, m_q/Λ_{QCD}, where m_q is the quark mass and Λ_{QCD} is the QCD scale, is related to the strong interaction. The effect of m_q/Λ_{QCD} variation on the ^{229}Th transition has been estimated in Refs. [21, 27, 28]. The high sensitivity to α comes about because the change in Coulomb energy between the isomers, which depends linearly on α, is almost entirely cancelled by the nuclear force contribution which has only weak α-dependence. This cancellation makes the energy of the transition $E_{is} = 8$ eV low compared to typical nuclear transitions, so any change in α and the Coulomb energy leads to a relative change several orders of magnitude larger in the energy of the transition $\Delta E_{is}/E_{is}$.

We also should note that the measurements of the variation of the fundamental constants does not require absolute frequency measurement. All that is required is high stability of the ratio of two frequencies with a different dependence on the fundamental constants [29, 30]. For example, it may be the ratio of the 8-eV nuclear transition frequency to that of an atomic clock transition in the Th ion, as considered in Ref. [31].

The change in the nuclear transition frequency, f, between the isomeric state and the ground state, δf, for a given change in the fine-structure constant, $\delta\alpha$, is [21]

$$h\,\delta f = \Delta E_C \frac{\delta\alpha}{\alpha}\,, \tag{2.1}$$

where ΔE_C is the difference in Coulomb energy between the two isomers. The enhancement factor K is defined by

$$\frac{\delta f}{f} = K\frac{\delta\alpha}{\alpha}\,, \tag{2.2}$$

where $K = \Delta E_C/E_{is}$. Therefore, to find the sensitivity of ^{229m}Th transition to variation in α, one needs to know ΔE_C.

The Coulomb energy E_C depends on the shape of the nucleus. Unlike atomic systems, which are spherical due to the $1/r$ potential from the pointlike nucleus (r is the distance from the nucleus), nuclear systems can have deformed shapes as the potential originates from the nucleons themselves. Reference [25] showed that, by modeling the nucleus as a prolate spheroid [32], ΔE_C can be deduced from measurements of the change in nuclear charge radius and quadrupole moment between the isomeric and the ground states. Using this model with measurements of nuclear parameters, the authors of [33] give a value of

$$\Delta E_C = -0.29\,(43)\,\text{MeV}\,, \tag{2.3}$$

where the dominant source of error is the uncertainty in measured quadrupole moments of the ground and the exited states. Such a ΔE_C is consistent with a K value anywhere between 0 and 10^5. This can be compared to a K of about 0.1–6 for current atomic clocks [29, 30, 34–37].

In this paper we use the fact that the change in quadrupole moment is related to the change in charge radius to arrive at ΔE_C with errors consistent with a nonzero value, consequently giving a nonzero value for K. This relationship can be understood from the assumption of a constant charge density between isomers. We verify that this assumption gives a relation that is consistent with previous results from nuclear theory [23]. We also test this assumption in several Mössbauer transitions, which we find have much lower sensitivities to α variation than the ^{229}Th transition. Finally, following models that suggest the existence of an octupole deformation in ^{229}Th, we use a more general treatment of a deformed nuclei. The results of the two models coincide within uncertainties.

2.2 Prolate spheroid model

We start by modeling the nucleus as a prolate spheroid with semiminor and semimajor axes a and c. The volume $(4\pi/3)\,R_0^3$ depends on a and c by

$$a^2 c = R_0^3\,. \tag{2.4}$$

The eccentricity e is defined by

$$e^2 = 1 - \frac{a^2}{c^2}\,, \tag{2.5}$$

while the mean-square radius $\langle r^2 \rangle$ and the quadrupole moment Q_0 are

$$\begin{aligned} \langle r^2 \rangle &= \frac{1}{5}\left(2a^2 + c^2\right)\,, \\ Q_0 &= \frac{2}{5}\left(c^2 - a^2\right)\,. \end{aligned} \tag{2.6}$$

The Coulomb energy can be written as a product of E_C^0, the Coulomb energy of an undeformed nucleus, and an anisotropy factor due to the deformation, B_C [38],

$$E_C = E_C^0\, B_C\,, \tag{2.7}$$

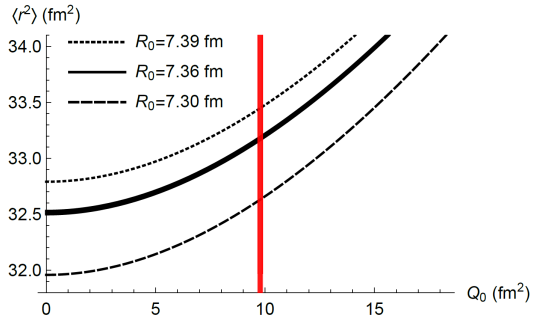

Figure 2.1: *Mean-square charge radius $\langle r^2\rangle$ as a function of intrinsic quadrupole moment Q_0 under the constant-volume ansatz for three volumes. The dashed lower curve corresponds to R_0 deduced from Hartree-Fock-Bogoliubov calculations using the SkM* functional, while the upper dotted curve is based on SIII functional (see Table 2.1). The middle curve, including errors, corresponds to $R_0 = 7.3615(16)$ fm deduced from the measurements by which (2.15) is obtained. The red line corresponds to the 1σ experimental range of Q_0 [39].*

where

$$E_{\rm C}^0 = \frac{3}{5}\frac{q_e^2 Z^2}{R_0}\,, \tag{2.8}$$

$$B_{\rm C} = \frac{(1-e^2)^{1/3}}{2e}\ln\left(\frac{1+e}{1-e}\right)\,. \tag{2.9}$$

Here q_e is the electron charge and Z is the number of protons.

In previous works [25], Q_0 and $\langle r^2\rangle$ were treated as independent parameters. As such, calculation of $\Delta E_{\rm C}$ involved derivatives of $E_{\rm C}$ both by Q_0 and by $\langle r^2\rangle$:

$$\Delta E_{\rm C} = \langle r^2\rangle \frac{\partial E_{\rm C}}{\partial\langle r^2\rangle}\frac{\Delta\langle r^2\rangle}{\langle r^2\rangle} + Q_0\frac{\partial E_{\rm C}}{\partial Q_0}\frac{\Delta Q_0}{Q_0}\,. \tag{2.10}$$

With current experimental values $\langle r^2\rangle = (5.76\text{ fm})^2$ and $Q_0 = 9.8(1)$ fm^2 [39], Eqs. (3.8) and (3.6) give

$$\Delta E_{\rm C} = -485\,\text{MeV}\frac{\Delta\langle r^2\rangle}{\langle r^2\rangle} + 11.6\,\text{MeV}\frac{\Delta Q_0}{Q_0}\,. \tag{2.11}$$

Substitution of measured changes in mean-square radius and quadrupole moment [33], $\Delta\langle r^2\rangle = 0.012\,(2)$ fm^2 and $\Delta Q_0/Q_0 = -0.01(4)$, gives the limit (2.3).

Let us now consider the ansatz of constant charge density between isomers, equivalent to the ansatz of constant volume. That is, R_0 and hence $E_{\rm C}^0$ are kept constant in the isomeric transition. Therefore, changes in $\langle r^2\rangle$ and Q_0 are coupled by (2.4) using (2.6). We show this dependence graphically in Fig. 2.1, and we can express it as

$$\frac{dQ_0}{d\langle r^2\rangle} = 1 + \frac{2\langle r^2\rangle}{Q_0} = 7.8\,, \tag{2.12}$$

Table 2.1: *Theoretical values of root-mean-square radius r_{rms}, Q_0, ΔQ_0, and Δr_{rms} calculated using Hartree-Fock-Bogoliubov approach with two energy functionals, SkM* and SIII. In the fifth row we deduce the relationship between ΔQ_0 and $\Delta\langle r^2\rangle$, which may be compared to the result of the constant density ansatz, $dQ_0/d\langle r^2\rangle = 7.8$. In the last two rows we show the change in Coulomb energy from direct calculation and using (2.14) with calculated values of charge radii.*

	SkM*		SIII	
	n	p	n	p
$r_{\rm rms}$ (fm)[a]	5.8716	5.7078	5.8923	5.7769
Q_0 (fm^2)[a]	9.2608	9.3717	9.0711	9.1643
ΔQ_0 (fm^2)[a]	0.2647	0.2756	−0.0516	−0.0495
$\Delta r_{\rm rms}$ (fm)[a]	0.0036	0.0039	−0.0005	−0.0005
$\Delta Q_0/\Delta\langle r^2\rangle$	6.26	6.19	8.76	8.57
$\Delta E_{\rm C}$ (MeV)[b]		−0.307		0.001
$\Delta E_{\rm C}$ (MeV)[a]		−0.287		0.036

[a] From Ref. [23], Table II and Eq. (2.14) for $\Delta E_{\rm C}$.
[b] From Ref. [23], Table I.

where 7.8 corresponds to the experimental values. Substitution of (3.12) into (2.11) gives us the following result:

$$\Delta E_{\rm C} = -180\,\text{MeV}\,\frac{\Delta\langle r^2\rangle}{\langle r^2\rangle}\,. \tag{2.13}$$

The relation between changes in $\langle r^2\rangle$ and Q_0 can also be obtained from nuclear calculations where the constant-density ansatz is not assumed. Results of the Hartree-Fock-Bogoliubov calculations of [23] are summarized in Table 2.1. We extract $\Delta Q_0/\Delta\langle r^2\rangle$ for two different energy functionals, SkM* and SIII, and for both protons and neutrons (for details see [23]). In all cases the derivative is close to that predicted by the constant-density ansatz.

In addition to the results reproduced in Table 2.1, Ref. [23] presents Hartree-Fock calculations (which do not include pairing) using the same functionals. For SkM*, the Hartree-Fock calculations give the wrong sign for $\langle r^2\rangle$, while for SIII the change between isomers is very small and susceptible to numerical noise. Nevertheless in both cases the Hartree-Fock calculations give reasonably close values for the derivative.

For the Hartree-Fock-Bogoliubov calculations, the SkM* better reproduces the measured energy interval and change in the nuclear radius between the isomers. We take the average of the SkM* value $dQ_0/d\langle r^2\rangle$ for protons and the experimental value from (3.12) as our estimate of the derivative, and their difference as an estimate of the derivative's uncertainty, giving $dQ_0/d\langle r^2\rangle = 7.0\,(1.6)$. [1] With this we write the change in Coulomb energy $\Delta E_{\rm C}$ in terms of the change in mean-square radius at the physical point as

$$\Delta E_{\rm C} = -210\,(60)\,\text{MeV}\,\frac{\Delta\langle r^2\rangle}{\langle r^2\rangle}\,. \tag{2.14}$$

[1] Alternatively, we could use the average value between SkM* and SIII numbers for the derivatives $\Delta Q_0/\Delta r^2$ but the change in the result would be within the error bars.

The last row in Table 2.1 lists the results of application of this formula to the nuclear calculations of $\Delta r_{\rm rms}$ from [23]. Filling in the measured $\Delta\langle r^2\rangle = 0.0105\,(13)$ fm^2 [40] and $\langle r^2\rangle = (5.76\text{ fm})^2$ [41], we obtain

$$\Delta E_{\rm C} = -0.067\,(19)\,\text{MeV}\,, \tag{2.15}$$

$$K = -0.82\,(25)\times 10^4\,. \tag{2.16}$$

Since our model does not rely on the measured ΔQ_0, which gives the biggest error in (2.3), the result of (2.15) has smaller error than (2.3). We also predict $\Delta Q_0/Q_0 = 0.0075\,(20)$ fm^2 which is within the experimental error of $\Delta Q_0/Q_0 = -0.01\,(4)$ fm^2 presented in Ref. [33].

2.3 Effect of octupole deformation

Nuclear calculations of N. Minkov and A. Pálffy suggest that the ^{229}Th nucleus has an octupole deformation [7, 42] (see also a recent experiment [43]). They therefore describe the nucleus using a quadrupole-octupole model, obtaining a fair comparison to experimental results [7, 42]. This prompts us to include an octupole deformation in addition to the quadrupole deformation.

To facilitate this we describe the nucleus shape by its radius vector in axially symmetric spherical harmonics [44, 45],

$$r(\theta) = R_s\left[1+\sum_{n=1}^{N}\left(\beta_n Y_{n0}(\theta)\right)\right]\,, \tag{2.17}$$

where the coefficients β_n are called deformation parameters and $N=3$ for the quadrupole-octupole model (pear shape). The length R_s is defined by normalization of the volume to that of the undeformed nucleus,

$$\frac{2\pi}{3}\int_0^\pi r^3(\theta)\sin\theta\,d\theta = \frac{4\pi R_0^3}{3}\,. \tag{2.18}$$

The parameter β_1 is set such that the center of mass of the shape is at the origin of the coordinate system.

The mean-square radius and the intrinsic quadrupole moment of the nucleus are related to the deformation parameters β_2 and β_3 through $r(\theta)$ by

$$\langle r^2\rangle = \int r^2(\theta)\rho(r)\,d^3r\,, \tag{2.19}$$

$$Q_0 = 2\int r^2(\theta)P_2(\cos\theta)\rho(r)\,d^3r\,, \tag{2.20}$$

where $\rho(r)$ is the charge density divided by the total charge. The factor 2 in (2.20) is a matter of definition [46], and fits with the special case of Q_0 in (2.6).

To determine β_2 for the pear shape, we solve (2.19) and (2.20) using the experimental values of Q_0 and $\langle r^2\rangle$. As the octupole moment of ^{229}Th has not yet been measured, we take $\beta_3 = 0.115$ from nuclear calculations [7]. We arrive at $\beta_2 = 0.22$ and $R_s = 7.3$ fm. This

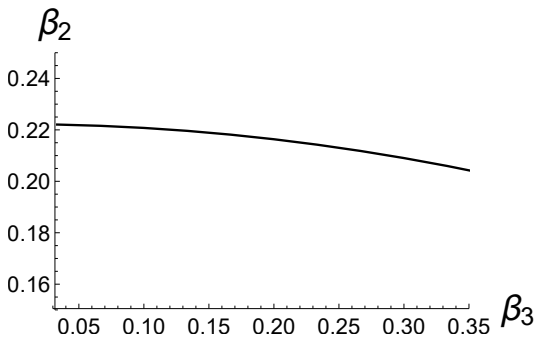

Figure 2.2: *Deformation parameter β_2 derived using (2.19) and (2.20) with experimental values of $Q_0 = 9.8\,fm^2$ and $\langle r^2\rangle = (5.76\,fm)^2$, as a function of β_3.*

value of β_2 is fairly close to the theoretical prediction of [7], $\beta_2 = 0.24$, and is not particularly sensitive to the chosen value of β_3 (see Fig. 2.2).

In this model the anisotropy factor is [32]

$$B_{\mathrm{C}} = 1 - \frac{5}{4\pi}\sum_{n=2}^{\infty}\frac{n-1}{2n+1}\beta_n^2 + \mathcal{O}(\beta_n^3)\ . \tag{2.21}$$

Higher-order terms do not change our results within stated errors. With the aforementioned values for β_2 and β_3, we obtain for the constant-density ansatz (i.e., constant E_C^0),

$$\Delta E_{\mathrm{C}} = -76\,\mathrm{MeV}\ \Delta\beta_2^2 - 108\,\mathrm{MeV}\ \Delta\beta_3^2 \tag{2.22}$$

$$\approx -190\,\mathrm{MeV}\ \frac{\Delta\langle r^2\rangle}{\langle r^2\rangle} - 0.42\,\mathrm{MeV}\ \frac{\Delta\beta_3^2}{\beta_3^2}\ . \tag{2.23}$$

Equation (2.23) is obtained by substituting (2.25), and is in good agreement with (2.13). We see that the sensitivity of the nuclear clock to α-variation does not depend strongly on the octupole moment.

2.4 Discussion

The constant-volume ansatz used in the present work may be tested in experiments. This ansatz allows one to relate the change in nuclear quadrupole moment to the change in nuclear charge radius. Therefore, determination of $\Delta\langle r^2\rangle$ by measuring the field isotope shift of atomic transitions, and extraction of ΔQ_0 from the hyperfine structure or nuclear rotational bands, gives a measure of the change in the nuclear charge density.

A specific procedure can be encoded in the change in mean-square radius [47, 48]

$$\Delta\langle r^2\rangle = \Delta\langle r^2\rangle_{\mathrm{sph}} + \Delta\langle r^2\rangle_{\mathrm{def}}\,. \tag{2.24}$$

Here the spherical part $\Delta\langle r^2\rangle_{\mathrm{sph}}$ describes the change in nuclear volume, i.e., volume contribution, and $\Delta\langle r^2\rangle_{\mathrm{def}}$ describes the deformation part assuming a constant volume, i.e., shape

Table 2.2: *Sensitivity of Mössbauer transitions to variation of the fine structure constant. Coulomb energy shifts ΔE_C and enhancement factors K are calculated using data from quadrupole moments [58] and isomeric shift measurements [59]. In columns 2 and 4 we use the constant density ansatz, where we have assumed a 25% error from the ansatz, Eq. (3.12), and 50% error in the values of $\Delta\langle r^2\rangle$ from Mössbauer isomer shifts [59]. The Eu isomers have more accurate values of $\Delta\langle r^2\rangle$ taken from muonic x-ray and Mössbauer data [60–62]. Columns 3 and 5 use experimental values of ΔQ_0 from [58] in the general formula (3.6). The ground-state $\langle r^2\rangle$ values are taken from [41]. ^{229}Th results are shown for comparison (discussed in the main text).*

	ΔE_C (MeV)		$\lvert K\rvert$	
	constant density	general	constant density	general
^{151}Eu 22 keV	−0.099 (51)	−0.099 (85)	4.6 (2.4)	4.6 (4.0)
^{153}Eu 103 keV	0.32 (18)	0.02 (15)	3.1 (1.8)	0.2 (1.5)
^{155}Gd 105 keV	0.030 (22)	0.08 (32)	0.28 (21)	0.8 (3.1)
^{157}Gd 64 keV	−0.055 (41)	−0.06 (21)	0.86 (63)	0.9 (3.3)
^{161}Dy 75 keV	−0.031 (23)	0.29 (55)	0.42 (31)	3.8 (7.4)
^{181}Ta 6 keV	0.19 (13)	0.20 (26)	30 (21)	32 (41)
^{243}Am 84 keV	0.23 (17)	0.45 (75)	2.8 (2.0)	5.4 (9.0)
^{229}Th 8 eV	−0.067 (19)	−0.26 (39)	0.82 (25) 10^4	3.1 (4.8) 10^4

contribution. The latter can be expressed by deformation parameters [47–50]

$$\Delta\langle r^2\rangle = \Delta\langle r^2\rangle_{\rm sph} + \frac{5}{4\pi}\langle r^2\rangle_{\rm sph}\left(\Delta\beta_2^2 + \Delta\beta_3^2 + ...\right), \tag{2.25}$$

where $\langle r^2\rangle_{\rm sph}$ is the mean-square charge radius of the nucleus assuming a spherical distribution. Equation (2.25) can be used in the future to test the volume-conservation hypothesis in isomers, once the $\Delta\beta$ is determined to higher accuracy.

Using existing experimental data [33] we may conclude that the relative change in volume between ^{229}Th isomers is less than a few parts per thousand, while the calculations in [23] imply a fractional volume change of about 5×10^{-4}. This gives a quantitative evaluation of the constant-volume ansatz, which at times is used in the literature (see, e.g., [51–53]).

The sensitivity to potential variation of α, i.e., the enhancement factor K, is three orders of magnitude larger than that of the most sensitive atomic clocks. For the present experimental bound $\delta\alpha/\alpha \lesssim 10^{-17}$ per year, the frequency shift is up to $\sim$200 Hz per year. Since such a frequency shift is six orders of magnitude larger than the projected accuracy of the nuclear clock [9], an unexplored range of $\delta\alpha$ may be tested. As discussed in Refs. [54–56],

the interaction between low-mass scalar dark matter and the electromagnetic field leads to oscillatory variation of α. Therefore, the improvement in the sensitivity to α variation by six orders of magnitude afforded by such a clock should also lead to improved sensitivity in the search for low-mass scalar dark matter.

We should note a certain similarity between the research on ^{229}Th isomeric transition and the very extensive experimental and theoretical studies of isomeric (chemical) shifts in Mössbauer spectroscopy, which also involve effects of the change in the nuclear charge radius and electric quadrupole moment between the ground and excited nuclear states connected by a γ transition. X-ray studies of muonic atoms are also able to deduce these nuclear properties. Using the same technique as in ^{229}Th we calculated the Coulomb energy difference $\Delta E_{\rm C}$ and the relative sensitivity to α variation K for nuclei where we have found sufficient experimental data. The results are presented in Table 3.1. The enhancement factors K for Mössbauer transitions ($K = \Delta E_C/E_{\rm is} \sim 1$ – 30) are much smaller than K for ^{229}Th since the energy of Mössbauer transitions is much larger, $E \sim 5$ – 100 KeV. However, they are comparable or even bigger than $K \sim 0.1 - 6$ in atomic clocks. The energy resolution in Mössbauer γ transitions may be as good as 10^{-18}, see, e.g., the measurement of the gravitational redshift in Ref. [57] where such a resolution was achieved after 5 days of measurements. This is even higher than that achieved recently in optical transitions, 10^{-17} – 10^{-18}. However, the authors of Ref. [57] noted a problem with solid state effects which are difficult to control.

The results in Table 3.1 serve as a test of the constant density ansatz. The predictions for $\Delta E_{\rm C}$ using the constant-density model and using the more general formula, (3.6), with experimental data for both $\Delta\langle r^2\rangle$ and ΔQ_0, agree within error bars. In these examples, using one of the values of $\Delta\langle r^2\rangle$ or ΔQ_0, the constant density ansatz reproduces the other value within error bars. This provides a check on the validity of the ansatz.

Acknowledgment

We thank Adriana Pálffy, Anne Fabricant, Angela Moller, and Vadim Ksenofontov for their help. The work was supported by the Australian Research Council Grants No. DP190100974 and DP20010015, the Gutenberg Fellowship, and the Alexander von Humboldt Foundation.

Bibliography

[1] E. Peik and C. Tamm, Europhys. Lett. **61**, 181 (2003).

[2] C. W. Reich and R. G. Helmer, Phys. Rev. Lett. **64**, 271 (1990).

[3] R. G. Helmer and C. W. Reich, Phys. Rev. C **49**, 1845 (1994).

[4] B. R. Beck, J. A. Becker, P. Beiersdorfer, G. V. Brown, K. J. Moody, J. B. Wilhelmy, F. S. Porter, C. A. Kilbourne, and R. L. Kelley, Phys. Rev. Lett. **98**, 142501 (2007).

[5] B. R. Beck, J. A. Becker, P. Beiersdorfer, G. V. Brown, K. J. Moody, C. Y. Wu, J. B. Wilhelmy, F. S. Porter, C. A. Kilbourne, and R. L. Kelley, Report No. LLNL-PROC-415170 (Los Alamos National Laboratory, 2009).

[6] E. V. Tkalya, C. Schneider, J. Jeet, and E. R. Hudson, Phys. Rev. C **92**, 054324 (2015).

[7] N. Minkov and A. Pálffy, Phys. Rev. Lett. **118**, 212501 (2017).

[8] S. G. Porsev, V. V. Flambaum, E. Peik, and Chr. Tamm, Phys. Rev. Lett **105**,182501 (2010).

[9] C. J. Campbell, A. G. Radnaev, A. Kuzmich, V. A. Dzuba, V. V. Flambaum, and A. Derevianko, Phys. Rev. Lett. **108**, 120802 (2012).

[10] P. G. Thirolf, B. Seiferle, and L. von der Wense, J. Phys. B: At. Mol. Opt. Phys. **52**, 203001 (2019).

[11] L. von der Wense, B. Seiferle, and P. G. Thirolf, Meas. Tech. **60**, 1178 (2018).

[12] E. V. Tkalya, Phys. Rev. Lett. **124**, 242501 (2020).

[13] B. S. Nickerson, M. Pimon, P. V. Bilous, J. Gugler, K. Beeks, T. Sikorsky, P. Mohn, T. Schumm, and A. Pálffy, Phys. Rev. Lett. **125**, 032501 (2020).

[14] S. G. Porsev, V.V. Flambaum, Phys. Rev. A **81**, 032504 (2010).

[15] S.G. Porsev, V.V. Flambaum, Phys. Rev. A**81**, 042516 (2010).

[16] A. Ya. Dzyublik, Phys. Rev. C **102**, 024604 (2020).

[17] B. Seiferle, L. von der Wense, P. V. Bilous, I. Amersdorffer, C. Lemell, F. Libisch, S. Stellmer, T. Schumm, C. E. Düllmann, A. Pálffy, and P. G. Thirolf, Nature **573**, 243 (2019).

[18] T. Masuda, A. Yoshimi, A. Fujieda, H. Fujimoto, H. Haba, H. Hara, T. Hiraki, H. Kaino, Y. Kasamatsu, S. Kitao, K. Konashi, Y. Miyamoto, K. Okai, S. Okubo, N. Sasao, M. Seto, T. Schumm, Y. Shigekawa, K. Suzuki, S. Stellmer, K. Tamasaku, S. Uetake, M. Watanabe, T. Watanabe, Y. Yasuda, A. Yamaguchi, Y. Yoda, T. Yokokita, M. Yoshimura, and K. Yoshimura, Nature **573**, 238 (2019).

[19] A. Yamaguchi, H. Muramatsu, T. Hayashi, N. Yuasa, K. Nakamura, M. Takimoto, H. Haba, K. Konashi, M. Watanabe, H. Kikunaga, K. Maehata, N. Y. Yamasaki, and K. Mitsuda, Phys. Rev. Lett. **123**, 222501 (2019).

[20] T. Sikorsky, J. Geist, D. Hengstler, S. Kempf, L. Gastaldo, C. Enss, C. Mokry, J. Runke, C. E. Düllmann, P. Wobrauschek, K. Beeks, V. Rosecker, J. H. Sterba, G. Kazakov, T. Schumm, and A. Fleischmann, Phys. Rev. Lett. **125**, 142503 (2020).

[21] V. V. Flambaum, Phys. Rev. Lett. **97**, 092502 (2006).

[22] V. V. Flambaum, N. Auerbach, and V. F. Dmitriev, Europhys. Lett. **85**, 50005 (2009).

[23] E. Litvinova, H. Feldmeier, J. Dobaczewski, and V. V. Flambaum, Phys. Rev. C **79**, 064303 (2009).

[24] P. G. Thirolf, B. Seiferle, and L. von der Wense, Ann. Phys. (Berlin) **531**, 1800381 (2019).

[25] J. C. Berengut, V. A. Dzuba, V. V. Flambaum, and S. G. Porsev, Phys. Rev. Lett. **102**, 210801 (2009).

[26] J. C. Berengut and V. V. Flambaum, Nuclear Physics News **20**, 19 (2010).

[27] Xiao-tao He and Zhong-zhou Ren, J. Phys. G: Nucl. Part. Phys. **34**, 1611 (2007).

[28] V. V. Flambaum and R. B. Wiringa, Phys. Rev. C **79**, 034302 (2009).

[29] V. A. Dzuba, V. V. Flambaum, and J. K. Webb, Phys. Rev. Lett. **82**, 888 (1999).

[30] V. A. Dzuba, V. V. Flambaum, and J. K. Webb, Phys. Rev. A **59**, 230 (1999).

[31] V. V. Flambaum and S. G. Porsev, Phys.Rev. A **80**, 064502 (2009).

[32] R. W. Hasse and W. D. Myers, *Geometrical Relationships of Macroscopic Nuclear Physics* (Springer-Verlag, Heidelberg, 1988).

[33] J. Thielking, M. V. Okhapkin, P. Glowacki, D. M. Meier, L. von der Wense, B. Seiferle, C. E. Düllmann, P. G. Thirolf, and E. Peik, Nature **556**, 321 (2018).

[34] N. Huntemann, B. Lipphardt, C. Tamm, V. Gerginov, S. Weyers, and E. Peik, Phys. Rev. Lett. **113**, 210802 (2014).

[35] V. V. Flambaum and V. A. Dzuba, Can. J. Phys. **87**, 25 (2009).

[36] V. A. Dzuba, V. V. Flambaum, and S. Schiller, Phys. Rev. A **98**, 022501 (2018).

[37] M.S. Safronova, Ann. Phys. (Berlin) **531**,1800364 (2019).

[38] B. C. Carlson, J. Math. Phys. **2**, 441 (1961).

[39] Note that the expressions for the laboratory/spectroscopic quadrupole moment differ by a factor of Z between [25] and [33]. That is because the factor Z was absorbed into the definition of the intrinsic quadrupole moment Q_0 in [33]. In this paper Q_0 is defined without the factor Z, so the quoted number for Q_0 in [33] equals $Q_0 Z$ in our notation. For the units of Q_0 we use fm^2; another common choice of units is eb (where eb stands for electron-barn, 1 eb $= 1.6022 \times 10^{-47}$C m^2), such that $Q\,(\text{eb}) = 10^2 eQ\,(\text{fm}^2)$.

[40] M. S. Safronova, S. G. Porsev, M. G. Kozlov, J. Thielking, M. V. Okhapkin, P. Głowacki, D. M. Meier, and E. Peik, Phys. Rev. Lett. **121**, 213001 (2018).

[41] I. Angeli and K. P. Marinova, At. Data Nucl. Data Tables **99**, 69 (2013).

[42] N. Minkov and A. Pálffy, Phys. Rev. Lett. **122**, 162502 (2019).

[43] M. M. R. Chishti, D. O'Donnell, G. Battaglia, M. Bowry, D. A. Jaroszynski, B. S. Nara Singh, M. Scheck, P. Spagnoletti, and J. F. Smith, Nat. Phys. **16**, 853 (2020).

[44] P. Möller, J. R. Nix, W. D. Myers, and W. J. Swiatecki, At. Data Nucl. Data Tables **59**, 185 (1995).

[45] P. A. Butler and W. Nazarewicz, Rev. Mod. Phys. **68**, 349 (1996).

[46] J. D. Jackson, *Classical Electrodynamics* (Wiley, New York, 1962), section 4.2 [3rd ed. (1999)].

[47] S. Ahmad, W. Klempt, R. Neugart, E. Otten, P.-G. Reinhard, G. Ulm, and K. Wendt, Nucl. Phys. A **483**, 244 (1988).

[48] G. Ulm, S. K. Bhattacherjee, P. Dabkiewicz, G. Huber, H. J. Kluge, T. Kühl, H. Lochmann, E. W. Otten, K. Wendt, S. A. Ahmad, W. Klempt, R. Neugart, and the ISOLDE Collaboration, Z. Phys. A **325**, 247 (1986).

[49] A. Bohr and B. R. Mottelson, *Nuclear Structure Volume II: Nuclear Deformations* (World Scientific, London, 1998).

[50] W. Kälber, J. Rink, K. Bekk, W. Faubel, S. Göring, G. Meisel, H. Rebel, and R. C. Thompson, Z. Phys. A **334**, 103 (1989).

[51] D. T. Yordanov, D. L. Balabanski, M. L. Bissell, K. Blaum, I. Budinčević, B. Cheal, K. Flanagan, N. Frömmgen, G. Georgiev, Ch. Geppert, M. Hammen, M. Kowalska, K. Kreim, A. Krieger, J. Meng, R. Neugart, G. Neyens, W. Nörtershäuser, M. M. Rajabali, J. Papuga, S. Schmidt, and P. W. Zhao, Phys. Rev. Lett. **116**, 032501 (2016).

[52] A. Boucenna, S. Madjber, and A. Bouketir, arXiv:nucl-th/0305026 (2003).

[53] M. Avgoulea, Y. P. Gangrsky, K. P. Marinova, S. G. Zemlyanoi, S. Fritzsche, D. Iablonskyi, C. Barbieri, E. C. Simpson, P. D. Stevenson, J. Billowes, P. Campbell, B. Cheal, B. Tordoff, M. L. Bissell, D. H. Forest, M. D. Gardner, G. Tungate, J. Huikari, A. Nieminen, H. Penttilä, and J. Äystö, J. Phys. G **38**, 025104 (2011).

[54] A. Arvanitaki, J. Huang, and K. Van Tilburg, Phys. Rev. D **91**, 015015 (2015).

[55] K. Van Tilburg, N. Leefer, L. Bougas, and D. Budker, Phys. Rev. Lett. **115**, 011802 (2015).

[56] Y. V. Stadnik and V. V. Flambaum, Phys. Rev. Lett. **115**, 201301 (2015).

[57] W. Potzel, C. Schafer, M. Steiner, H. Karzel, W. Schiessl, M. Peter, G.M. Kalvius, T. Katila, E. Ikonen, P. Helisto and J. Hietaniemi, Hyperfine Interact. **72**, 197 (1992).

[58] N.J. Stone, At.Data Nucl. Data Tables **111–112**,1(2016).

[59] G. M. Kalvius and G. K. Shenoy, At. Data Nucl. Data Tables **14**, 639 (1974).

[60] Y. Tanaka, R. M. Steffen, E. B. Shera, W. Reuter, M. V. Hoehn, and J. D. Zumbro, Phys. Rev. C **29**, 1897 (1984).

[61] J. Hess, Nucl. Phys. A **142**, 273 (1970).

[62] E. Steichele, S. Hüfner, and P. Kienle, Phys. Lett. **14**, 321 (1965).

Chapter 3

Effects of variation of the fine structure constant α and quark mass m_q in Mössbauer nuclear transitions

Phys. Rev. C **105**, L051303 (2022)

Pavel Fadeev[1], Julian C. Berengut[2], and Victor V. Flambaum [1,2]

[1] *Helmholtz Institute Mainz, Johannes Gutenberg University, 55099 Mainz, Germany*
[2] *School of Physics, University of New South Wales, Sydney, New South Wales 2052, Australia*

High accuracy measurements in Mössbauer transitions open up the possibility to use them in the search for temporal and spatial variation of the fine-structure constant α, quark mass m_q, and dark matter field which may lead to the variation of α and m_q. We calculate the sensitivity of nuclear transitions to variation of α and m_q. Mössbauer transitions have high sensitivity to variation of quark mass m_q and the strong interaction scale Λ_{QCD}, to which atomic optical clocks are not sensitive. The enhancement factors K, defined by $\frac{\delta f}{f} = K_\alpha \frac{\delta\alpha}{\alpha}$ and $\frac{\delta f}{f} = K_q \frac{\delta m_q}{m_q}$ where f is the transition energy, may be large in some transitions. The 8 eV nuclear clock transition in ^{229}Th ($K_q \approx 10^4$) and 76 eV transition in ^{235}U ($K_\alpha \approx K_q \approx 10^3$) may be investigated using laser spectroscopy methods.

3.1 Introduction

Mössbauer spectroscopy has been used for diverse purposes ranging from gravitational redshift of light [1] to determinations of solids, atomic, and nuclear properties. The sensitivity of Mössbauer transitions can reach the 10^{-18} level, see e.g. [2]. Moreover, a recent paper [3] claims that for a variable perturbation the sensitivity may reach $\Delta E \sim 10^{-15} - 10^{-17}$ eV which corresponds to a $10^{-20} - 10^{-22}$ relative sensitivity to the frequency shift. For comparison, the best atomic clock limit on relative changes of α is $1.0(1.1) \times 10^{-18}$ per year [4] (atomic transition frequencies depend on α due to the relativistic effects [5–7]) while the limit on variation of m_q is $0.71(44) \times 10^{-14}$ per year [8] (here sensitivity to m_q comes from the nuclear magnetic moments in Cs and Rb hyperfine transitions [9]). High sensitivity motivates the study of nuclear transitions for topics of fundamental physics, such as variation of the

fundamental constants [10, 11], search for new particles and interactions [3, 11], and search for dark matter (see below). Different possibilities to produce a nucleus in upper state of Mössbauer transition are discussed e.g. in Ref. [3].

3.1.1 Variation of the fine structure constant α

The search for temporal and spatial variation of the fine structure constant α is an ongoing interdisciplinary endeavour spanning the fields of astrophysics, molecular, atomic, nuclear, and solid state physics [12, 13]. We elucidate the usage of high precision Mössbauer spectroscopy in the search for variation of α. The sensitivity to the change of α is encoded in the enhancement factor K_α, defined as

$$\frac{\delta f}{f} = K_\alpha \frac{\delta\alpha}{\alpha}\,. \tag{3.1}$$

A nuclear transition energy f would change by δf due to a change of α by $\delta\alpha$. Values of K_α for current atomic clocks are of the order 0.1–10 [5–7, 14–16]. In nuclei K_α may be found from the following relation [10]:

$$K_\alpha = \Delta E_{\rm C}/f\,, \tag{3.2}$$

where ΔE_C is the change in Coulomb energy in this transition. In the ^{229}Th 8 eV nuclear clock transition studied e.g. in Refs. [17–36] and expected to be a highly sensitive probe for time variation in α [10, 37–42], our recent analysis [11] gives K_α of 10^4.

3.1.2 Variation of the quark mass and strong interaction

To avoid dependence on the human units which also may vary (e.g. hyperfine transition frequency in Cs, used to define the second and Hz, which has a complicated dependence on the fundamental constants [9]), we consider variations of dimensionless parameters like the fine structure constant α. Another dimensionless parameter which affects nuclear transition energies is $X_q \equiv m_q/\Lambda_{QCD}$, where $m_q = (m_u + m_d)/2$ is the quark mass and Λ_{QCD} is the QCD scale. We do not make any assumptions about their independent variation since in this case we must specify the units in which we measure them. Here we measure m_q in units of Λ_{QCD}, i.e. in the calculations we may keep Λ_{QCD} constant.

The energy of a nuclear transition may be presented as

$$f = \Delta E_{\rm C} + E_S\,, \tag{3.3}$$

where E_S is the difference in bulk binding energies of the excited and ground states (including kinetic and strong potential energy but excluding the Coulomb interaction energy). Thus, using experimental value of the transition energy f and calculated value of the Coulomb energy difference $\Delta E_{\rm C}$, we can find $E_S = f - \Delta E_{\rm C}$. The dependence of E_S on quark mass was calculated in Ref. [37]:

$$\frac{\delta E_S}{E_S} = -1.45\frac{\delta m_q}{m_q}\,. \tag{3.4}$$

Using Eqs. (3.2 – 3.4), we obtain

$$\frac{\delta f}{f} = K_q \frac{\delta m_q}{m_q}, \quad K_q = 1.45(K_\alpha - 1). \tag{3.5}$$

3.2 Possible physical origins of α and m_q variation in Mössbauer transitions

There are several possible physical origins of α and m_q variation in Mössbauer transitions, some of which we illuminate here. Many popular theories extending the Standard Model contain scalar fields ϕ which interact with quarks q as $-(\phi/\Lambda_q)m_q\bar{q}q$. Here Λ_q is the interaction constant. This interaction may be added to the mass term in the Lagrangian $-m_q\phi\bar{q}q$ and presented as a dependence of the effective quark mass $m_q(\phi) = m_q(1 + (\phi/\Lambda_q))$ on the field ϕ (see e.g. [43, 44]). Another possibility is that an interaction $(\phi/4\Lambda_\gamma)F_{\mu\nu}F^{\mu\nu}$ between the scalar field and electromagnetic field $F^{\mu\nu}$ may be added to the electromagnetic term in the Lagrangian $F^{\mu\nu}F_{\mu\nu}/4$. This will manifest as a dependence of the fine structure constant $\alpha(\phi) = \alpha(1+(\phi/\Lambda_\gamma))$ on the field ϕ (see e.g. [43–45]). Assuming that the source and absorber of the Mössbauer radiation are separated by some distance r, the values of α and m_q can be different at these points, if the field ϕ varies in space (see below).

3.2.1 Yukawa field ϕ

The field ϕ may vary since the interaction between the field ϕ and Standard Model particles leads to the Yukawa field $\phi = C\exp(-mr)/r$ produced by any massive body. The coefficient C has been calculated in Ref. [44]. In this way the presence of a massive body affects the fundamental constants.

For example, in the experiment [44] variation of the field ϕ and $\alpha(\phi)$ was produced by moving a 300 kg lead mass back and forth, affecting the ratio of the transition frequencies in Dy and Cs atoms. These have different dependence on α, since in Dy K_α is strongly enhanced [5–7]. In the case of Mössbauer transitions, a mass may perform oscillating motion toward emitter (or absorber) of the radiation, producing a difference in the transition frequencies between the emitter and absorber $\delta f = f(K_\alpha\delta\alpha/\alpha + K_q\delta m_q/m_q)$ which oscillates with the frequency of the mass motion.

Alternatively, the Yukawa field ϕ may be generated on a microscopic scale. In a recent paper [3] a technique to search for new scalar and tensor interactions at the submicrometer scale is presented. They suggest to place the optically flat “attractor" (source of Yukawa field ϕ), which perturbs the Mössbauer absorber frequency, on a micropositioner. This arrangement will provide a high sensitivity to the field ϕ with mass corresponding to the submicron Compton wavelength. Importantly, the paper [3] provides estimates of the systematic effects produced by the electromagnetic interactions and concludes that they are very small: the estimated sensitivity is $\Delta E \sim 10^{-15}$ – 10^{-17} eV which corresponds to $\delta f/f \sim 10^{-20}$ – 10^{-22}. Based on these estimates and using $\delta f = f(K_\alpha\delta\alpha/\alpha + K_q\delta m_q/m_q)$ with values of K from Table 3.1, we obtain sensitivity to the variations $\delta\alpha/\alpha \sim \delta m_q/m_q \sim 10^{-20}$ – 10^{-23}. This

estimate may be optimistic but we should compare it with the current limits from atomic transitions $\delta\alpha/\alpha \sim 10^{-17} - 10^{-18}$ and $\delta m_q/m_q \sim 10^{-14}$.

A gradient of ϕ may also be due to the Yukawa field produced by a nearby mountain or by the whole Earth if this field has a large range (a small mass). Here the situation is somewhat similar to the measurements of the gradients of the gravitational field.

3.2.2 Dark matter field ϕ

If we identify the scalar field with dark matter, a gradient of the field $\phi = \phi_0 \cos(\mathbf{k}\cdot\mathbf{r} - \omega t)$ appears due to the non-zero wave vector $k \approx mv/\hbar$, where v is the speed of Earth in the reference frame of the Galaxy and $\omega \approx mc^2/\hbar$, ϕ_0 is determined by the dark matter mass density (see e.g. [43, 45]). In this case we have oscillating $m_q(\phi) = m_q(1 + (\phi/\Lambda_q))$ and $\alpha(\phi) = \alpha(1 + (\phi/\Lambda_\gamma))$, which depend on the position $\mathbf{r}$. Here Λ_γ is the constant of the interaction between the scalar field ϕ and photon. Therefore, the dark matter field ϕ induces oscillations in the difference of the transition energies between separated emitter and absorber of the Mössbauer radiation.

A gradient of the field ϕ may exist in the transient field of passing clumps of dark matter, Bose stars, domain walls, etc. A gradient of ϕ may also exist in the field of scalar particles captured by Earth (see e.g. reviews [13, 46] and references therein).

3.2.3 Comparison of transition frequencies which have different dependence on fundamental constants

Search for variation of the fundamental constants in atomic experiments has been done using time dependence measurement of the ratio of two transition frequencies which have different dependence on the fundamental constants. A Mössbauer transition might be compared with a transition of approximately the same frequency in a highly charged ion. It may be challenging to find such ion transition, but they may be sought in the spectra of ions with open f-shell, which are very dense.

In the case of the 8 eV nuclear clock transition in ^{229}Th, laser optical spectroscopy methods, such as frequency comb, may be used for comparison with other transitions. High frequency sources of coherent radiation, based on the multiplication of the frequencies of the laser field, should allow one to extend this approach to 76 eV transition in ^{235}U.

3.3 Calculation of the sensitivity to α and m_q variation in nuclear transitions

To deduce K_α for a particular transition, ΔE_C must be calculated. This can be done using measurements of the changes in the mean square charge radius $\Delta\langle r^2\rangle$ and intrinsic quadrupole moment ΔQ_0 between the ground and excited states [11, 47]:

$$\Delta E_{\rm C} = \langle r^2\rangle \frac{\partial E_{\rm C}}{\partial\langle r^2\rangle}\frac{\Delta\langle r^2\rangle}{\langle r^2\rangle} + Q_0\frac{\partial E_{\rm C}}{\partial Q_0}\frac{\Delta Q_0}{Q_0}\,. \tag{3.6}$$

To extract values of intrinsic electric quadrupole moments Q_0 from experimental data for the electric quadrupole moments Q_{lab} we use the following relation for rotating deformed nuclei:

$$Q_{lab} = ZQ_0 \frac{I(2I-1)}{(I+1)(2I+3)} \,. \tag{3.7}$$

The use of this formula in nuclei with a small or zero deformation is not justified, however the electric quadrupole in such nuclei is small and has little effect on the final result.

To calculate derivatives $\frac{\partial E_{\rm C}}{\partial \langle r^2 \rangle}$ and $\frac{\partial E_{\rm C}}{\partial Q_0}$ we model the nucleus as a spheroid [11, 47]. In such a model

$$E_{\rm C} = E^0_{\rm C}\, B_{\rm C} \,, \tag{3.8}$$

$$E^0_{\rm C} = \frac{3}{5}\frac{q_e^2 Z^2}{R_0} \,, \tag{3.9}$$

where q_e is the electron charge, Z is the number of protons, and for a prolate spheroid ($Q > 0$):

$$B_{\rm C} = \frac{(1-e^2)^{1/3}}{2e} \ln\left(\frac{1+e}{1-e}\right) \,, \tag{3.10}$$

with e being the eccentricity. For an oblate spheroid ($Q < 0$), with the eccentricity defined such that it stays positive:

$$B_{\rm C} = \frac{(1+e^2)^{1/3}}{e} \arctan(e) \,. \tag{3.11}$$

If one of the ΔQ_0 or $\Delta\langle r^2 \rangle$ measurements is missing, one way to estimate the result is by using the ansatz of constant charge density between isomers, which is equivalent to the ansatz of constant volume [11]. In such a case, for a spheroid,

$$\frac{dQ_0}{d\langle r^2 \rangle} = 1 + \frac{2\langle r^2 \rangle}{Q_0} \,. \tag{3.12}$$

Note that in Refs. [11, 47] we tested the accuracy of Eq. (3.6) and constant density anzats Eq. (3.12) using results of Hartree-Fock-Bogolyubov calculations [39] of ΔE_C, ΔQ_0 and $\Delta\langle r^2 \rangle$ for the ^{229}Th nuclear transition. We estimated the error in the constant density ansatz of $\sim 25\%$.

In Table 3.1 we compile an extensive list of ΔE_C and enhancement factors K for Mössbauer transitions. The measured values of $\Delta\langle r^2 \rangle$ and Q, which we use as an input, are presented in the Appendix. The accuracy of the electric quadrupole moments measurements at the moment is insufficient for extraction of reliable values ΔQ_0. Therefore, we base our results on the measured values of $\Delta\langle r^2 \rangle$ (which in any case gives the main contribution to ΔE_C) and constant density ansatz Eq. eq:dQdr2 to find ΔQ_0. Note that if we neglect ΔQ_0, the value of ΔE_C would increase. Therefore, the constant density ansatz gives us a conservative estimate of ΔE_C and K.

For some elements $\Delta\langle r^2 \rangle$ is absent in the literature, to the best of our knowledge. For an estimate, we could use the constant density ansatz Eq. (3.12) to find $\Delta\langle r^2 \rangle$ using known

Table 3.1: *Sensitivity of Mössbauer transitions to variation of the fine structure constant and of the quark mass. Coulomb energy shifts ΔE_C and enhancement factors K calculated using data which we list in the Appendix. We present in the Table the "experimental" errors which are determined from the errors in $\Delta\langle r^2\rangle$ values. Our estimate for the constant density ansatz "theoretical" error is 25 %.*

	$T_{1/2}$	$j\pi$		$\Delta E_{\rm C}$ (keV)	K_α	K_q
	excited state	gr	ex	const. density	const. density	const. density
^{57}Fe 14.4 keV	98 ns	1/2−	3/2−	39(9%)	2.7(9%)	2.4(14%)
^{67}Zn 93.3 keV	9.07 μs	5/2−	1/2−	−35(27%)	−0.37(27%)	−1.99(7%)
^{83}Kr 9.3 keV	147 ns	9/2+	7/2+	−15 (25%)	−1.6 (25%)	−3.8(15%)
^{99}Ru 90 keV	20.5 ns	5/2+	3/2+	−59 (26%)	−0.66 (26%)	−2.40(10%)
^{119}Sn 23.9 keV	17.8 ns	1/2+	3/2+	−25.1(3%)	−1.053(3%)	−2.98(1%)
^{121}Sb 37.2 keV	3.5 ns	5/2+	7/2+	183(4%)	4.91(4%)	5.67(5%)
^{125}Te 35.5 keV	1.48 ns	1/2+	3/2+	−13.3(17%)	−0.37(17%)	−1.99(5%)
^{127}I 57.6 keV	1.95 ns	5/2+	7/2+	56.1(10%)	0.97(10%)	−0.04(400%)
^{129}I 27.8 keV	16.8 ns	7/2+	5/2+	−69.7(10%)	−2.51(10%)	−5.08(7%)
^{149}Sm 22.5 keV	7.6 ns	7/2−	5/2−	−5.3 (29%)	−0.24 (29%)	−1.79(6%)
^{151}Eu 22 keV	9.5 ns	5/2+	7/2+	−99 (29%)	−4.6 (29%)	−8.1(24%)
^{153}Eu 83.4 keV	0.80 ns	5/2+	7/2+	10.2 (25%)	0.12 (25%)	−1.27(3%)
^{153}Eu 103 keV	3.9 ns	5/2+	3/2+	321 (15%)	3.1 (15%)	3.1(23%)
^{155}Gd 86.5 keV	6.35 ns	3/2−	5/2+	22 (25%)	0.25 (25%)	−1.09(8%)
^{155}Gd 105 keV	1.18 ns	3/2−	3/2+	30 (25%)	0.28 (25%)	−1.04(10%)
^{157}Gd 64 keV	0.46 ms	3/2−	5/2+	−55 (25%)	−0.86 (25%)	−2.69(12%)
^{161}Dy 25.7 keV	29 ns	5/2+	5/2−	−29 (25%)	−1.14 (25%)	−3.10(13%)
^{161}Dy 43.8 keV	0.78 ns	5/2+	7/2+	6.3 (25%)	0.14 (25%)	−1.24(4%)
^{161}Dy 75 keV	3.2 ns	5/2+	3/2−	−31 (25%)	−0.42 (25%)	−2.06(7%)
^{181}Ta 6 keV	6.05 ms	7/2+	9/2−	191 (25%)	30 (25%)	43 (26%)
^{197}Au 77.3 keV	1.91 ns	7/2+	1/2+	−42(29%)	−0.54(29%)	−2.24(10%)
^{229}Th 8 eV	10^3 s	5/2+	3/2+	−67 (13%)	$-0.82\,10^4$(13%)	$-1.19\,10^4$(13%)
^{235}U 76 eV	26 m	7/2−	1/2+	~ 100	10^3	10^3
^{243}Am 84 keV	2.3 ns	5/2−	5/2+	235 (25%)	2.8 (25%)	2.6 (39%)

values of the electric quadrupole moments Q in ^{235}U 46 keV, ^{233}U 40 keV, ^{179}Hf 123 keV, ^{165}Ho 95 keV, ^{160}Ho 60 keV, and ^{158}Ho 67.2 keV. However, the errors in ΔQ_0 and K_α are too large in these cases, so we can not make definite predictions.

We see in Table 3.1 that the average value of $|\Delta E_C|$ in medium and heavy deformed nuclei is ~ 70 keV. Therefore, we may assume $\Delta E_C \sim 70$ keV and $|K_\alpha| \sim 70$ keV$/f$ in all medium and heavy deformed nuclei where accurate data for $\Delta\langle r^2\rangle$ are not available. In light nuclei and spherical nuclei $|\Delta E_C| \sim 30$ keV .

Two exceptional transitions presented in Table 3.1 are the 8 eV nuclear clock transition in ^{229}Th and the 76 eV transition in ^{235}U. Investigation of the ^{229}Th transition using laser spectroscopy methods has long been discussed in the literature, however new sources of coherent radiation cover the range up to 100 eV (see e.g. [48]), so 76 eV transition in ^{235}U may be investigated using high precision spectroscopy too. The probability of the photon emission in the bare ^{235}U nucleus is very small but it is significantly enhanced by the electronic bridge mechanism in many-electron ions [49] (see also [50]). To avoid discharge of the 76 eV nuclear excited state by electron emission, ionization potential of the uranium ion should exceed 76 eV. This condition is satisfied in ions with charge bigger than 6. The values of the enhancement factors for 76 eV transition in ^{235}U, $K_q \approx K_\alpha \approx 10^3$, are estimated in the Appendix.

3.4 Summary

In summary, we show that nuclear transitions are a sensitive tool in the search for the variation of the fine structure constant α and especially variation of the strong interaction parameter m_q/Λ_{QCD} to which atomic optical transitions are not sensitive. We calculate the sensitivity to these parameters, presented as the enhancement factors K_α and K_q, for a number of Mössbauer transitions, 8 eV transition in ^{229}Th, and 76 eV transition in ^{235}U .

Acknowledgments

We are grateful to S. Bladwell who participated at the initial stage of this work. This work was supported by the Australian Research Council Grants No. DP190100974 and DP200100150 and the Gutenberg Fellowship.

3.5 Nilsson model calculations for 76 eV ^{235}U transition

Two low-lying energy transitions are of particular interest due to their high K values and possibility to use high precision atomic spectroscopy methods: the 8 eV ^{229}Th and the 76 eV ^{235}U. If these cases are realized with Mössbauer spectroscopy, they might bring the method into the UV laser range, in recoil-free resonance. We recently calculated K_α for ^{229}Th in [11]. Sensitivity to the quark mass for ^{229}Th is calculated in the present work using $K_q = 1.45(K_\alpha - 1)$. Let us now focus on the case of the 76 eV transition in ^{235}U.

The mean square root charge radius $\langle r^2\rangle^{1/2}$ of ^{235}U is 5.8337(41) fm [51]. As far as we know, the charge radius for the excited state has not been measured, so we estimate the difference of the charge radii between excited and ground states using the Nilsson deformed oscillator model [52]. Within the Nilsson model excited and ground states of ^{235}U differ by the z axis quantum numbers n_z of external neutron: $n_{z,e} = 3$ and $n_{z,g} = 4$. For the harmonic oscillator

$$\langle z^2\rangle = \frac{1}{m_N\omega_z}\left(n_z + \frac{1}{2}\right), \tag{3.13}$$

where $m_N = 940$ MeV is the nucleon mass and ω_z is the harmonic oscillator frequency on the symmetry axis of the deformed nucleus. Substitution of $n_{z,e} = 3$ and $n_{z,g} = 4$ gives

$$\langle r_3^2\rangle - \langle r_4^2\rangle = -\frac{1}{m_N\omega_z}. \tag{3.14}$$

The value of $\langle r^2\rangle$ is calculated for the total density of all nucleons, therefore, we should divide the result by the number of nucleons A.

$$\Delta\langle r^2\rangle = -\frac{1}{A}\frac{(\hbar c)^2}{m_N\omega_z} = -\frac{1}{235}\frac{197^2}{940\times 5} = -0.035\,\mathrm{fm}^2. \tag{3.15}$$

The quadrupole moment of ^{235}U ground state was measured to be $Q_{lab} = 4.936(6)$ b in the laboratory frame [53]. To calculate the intrinsic quadrupole moment Q_0 we use Eq. (3.7) with the nuclear spin $I = 7/2$.

As the quadrupole moment of the excited state has not been measured, we estimate the difference of Q_0 for the excited and ground states using the Nilsson model. Quadrupole moment for external neutron is given by

$$Q_0 = \frac{1}{A}\left[\frac{2}{m_N\omega_z}\left(n_z + \frac{1}{2}\right) - \frac{2}{m_N\omega_z}(N - n_z + 1)\right], \tag{3.16}$$

where N is the principle quantum number, which is 6 for the exited state and 7 for the ground state. Equation (3.16) is a result of using Eq. (3.13) in the quadrupole moment defined as

$$Q_0 = 2\langle z^2\rangle - \langle x^2 + y^2\rangle. \tag{3.17}$$

Inserting numerical values, the change in the intrinsic quadrupole moment of the distribution of A nucleons between the excited and ground states is

$$\Delta Q_0 = \frac{1}{A}\frac{1}{m_N\omega_z}(6 - 8) = -0.064\,\mathrm{fm}^2. \tag{3.18}$$

Using these values we obtain ΔE_C=434 keV for the prolate spheroid model and ΔE_C=191 keV for the constant density model. These values are few times bigger than $\Delta E_C \sim 100$ keV in other heavy deformed nuclei. Therefore, we assume that our Nilsson model calculations overestimate ΔE_C few times. A conservative estimate is $K_q \approx K_\alpha \sim 100$ keV/76 eV $\approx 10^3$.

Note that the E3 (76 eV) transition in the uranium ion occurs with the active participation of the electron shell in the electron bridge process. In fact, this is a re-emission of a photon by the electron shell with a change in the multipolarity and sometime with a change in the energy

of the initial gamma quantum. For example, the energy of the second electronic transition (at which the photon is emitted) depends on the variation of the fine structure constant α. However, we do not see any enhancement of the sensitivity to α in the electron part of the process while sensitivity of the nuclear transition frequency is very strongly enhanced. This means that the electronic effects can not significantly affect the estimate $K \sim 10^3$.

3.6 Inputs for derivation of K_α

In Table 3.2 we present the inputs we used for each isomeric transition to arrive at the values of K_α and K_q in the main text. For ^{57}Fe, we take the average of three values in [54] for $d\langle r^2\rangle$. For $d\langle r^2\rangle$ of ^{235}U we take the value derived in the Appendix 3.5. In ^{121}Sb, ^{127}I, and ^{129}I the error on $d\langle r^2\rangle$ is unknown.

Table 3.2: *Experimental data used for input. The ground state $\langle r^2\rangle$ values are taken from [51]. $\Delta\langle r^2\rangle$ referenced individually for each transition, unless taken from Mössbauer isomer shifts in [55]. Individual values in [55] do not have error bars, only a general "optimistic" estimate of the error $\sim$ 25% is given. We present % error in brackets. Q_{lab} values are from [53]. The ratio Q_{ex}/Q_{gr} is taken from the references in [53], as many times its uncertainty is smaller than the uncertainty one gets by division of individual values Q_{ex} and Q_{gr}. Empty cells of Q_{ex}/Q_{gr} appear when this ratio was obtained by division of individual values Q_{ex} and Q_{gr}.*

	$j\pi$				Q_{lab}		
	ground	excited	r^{gr}_{rms} fm	$d\langle r^2\rangle 10^{-3}$ fm^2	ground	excited	Q_{ex}/Q_{gr}
^{57}Fe 14.4 keV	1/2−	3/2−	3.7532± 0.0017	−23.4 (4.8%) [54]	0	0.160±0.008	
^{67}Zn 93.3 keV	5/2−	1/2−	3.9530± 0.0027	18 (22%)[56]	0.150± 0.015	0	
^{83}Kr 9.3 keV	9/2+	7/2+	4.1871± 0.0023	6.4 (25%)	0.259± 0.001	0.507± 0.003	1.958± 0.002
^{99}Ru 90 keV	5/2+	3/2+	4.4338± 0.0042	20 (25%)	0.079± 0.004	0.231± 0.013	2.93± 0.07
^{119}Sn 23.9 keV	1/2+	3/2+	4.6438± 0.0020	7.42 (2.3%)[54]	0	−0.132± 0.001	
^{121}Sb 37.2 keV	5/2+	7/2+	4.6802± 0.0026	−0.052 [57]	−0.543± 0.011	−0.727± 0.016	1.34± 0.01
^{125}Te 35.5 keV	1/2+	3/2+	4.7204± 0.0030	3.8 (13%) [54]	0	−0.31± 0.02	
^{127}I 57.6 keV	5/2+	7/2+	4.7500± 0.0081	−15.3 [54]	−0.696± 0.012	−0.624± 0.011	0.896± 0.002
^{129}I 27.8 keV	7/2+	5/2+	4.74± 0.01	19.3 [54]	−0.488± 0.008	−0.604± 0.010	1.2385± 0.0011
^{149}Sm 22.5 keV	7/2−	5/2−	5.0134± 0.0035	1.3 (25%)	0.078± 0.008	1.01± 0.09	
^{151}Eu 22 keV	5/2+	7/2+	5.0522 ± 0.0046	24.8 (29%)[58]	0.903 ± 0.010	1.28 ± 0.02	
^{153}Eu 83.4 keV	5/2+	7/2+	5.1115± 0.0062	−2.7 (25%)	2.41± 0.02	0.44± 0.02	
^{153}Eu 103 keV	5/2+	3/2+	5.1115 ± 0.0062	−85(15%) [59]	2.41 ± 0.02	1.253± 0.012	0.52± 0.003
^{155}Gd 86.5 keV	3/2−	5/2+	5.1319± 0.0041	−5.6 (25%)	1.27± 0.03	0.110± 0.008	0.087± 0.006
^{155}Gd 105 keV	3/2−	3/2+	5.1319± 0.0041	−7.7 (25%)	1.27± 0.03	1.27± 0.05	1± 0.03

	$j\pi$				Q_{lab}		
	ground	excited	r^{gr}_{rms} fm	$d\langle r^2\rangle 10^{-3}$ fm^2	ground	excited	Q_{ex}/Q_{gr}
^{157}Gd 64 keV	3/2−	5/2+	5.1449 ± 0.0042	14.3 (25%)	1.35 ± 0.03	2.43 ± 0.07	1.80 ± 0.03
^{158}Ho 67.2 keV	5+	2−	5.1571± 0.0316		4.2± 0.4	1.66± 0.17	
^{160}Ho 60 keV	5+	2−	5.1662± 0.0315		4.0± 0.2	1.83± 0.17	
^{161}Dy 25.7 keV	5/2+	5/2−	5.1962± 0.0459	7.4 (25%)	2.51± 0.02	2.51± 0.02	
^{161}Dy 43.8 keV	5/2+	7/2+	5.1962± 0.0459	−1.6 (25%)	2.51± 0.02	0.53± 0.13	0.21 ± 0.05
^{161}Dy 75 keV	5/2+	3/2−	5.1962± 0.0459	7.9(25%)	2.51± 0.02	1.45± 0.06	0.577± 0.025
^{165}Ho 95 keV	7/2−	9/2−	5.2022± 0.0312		3.58± 0.02	3.52± 0.04	0.983± 0.008
^{179}Hf 123 keV	9/2+	11/2+	5.3408± 0.0031		3.79± 0.03	1.88± 0.03	
^{181}Ta 6 keV	7/2+	9/2−	5.3507± 0.0034	−43(25%)	3.17± 0.02	3.59± 0.02	1.1315± 0.0002
^{197}Au 77.3 keV	3/2+	1/2+	5.4371± 0.0038	8.28(29%) [54]	0.547± 0.016	0	
^{229}Th 8 eV	5/2+	3/2+	5.7557 ± 0.0143	10.5 (12%)[13]	3.13 ± 0.03	1.74± 0.06	0.555± 0.019 [60]
^{233}U 40 keV	5/2+	7/2+	5.8203± 0.0049		3.663± 0.008	0.64± 0.03	
^{235}U 46 keV	7/2−	9/2−	5.8337± 0.0041		4.936± 0.006	1.87± 0.03	
^{235}U 76 eV	7/2−	1/2+	5.8337 ± 0.0041	−35 [61]	4.936± 0.006	0	
^{243}Am 84 keV	5/2−	5/2+	5.9048, 0.0035	−42 (25%)	4.32± 0.06	4.2± 0.2	0.97± 0.05

Bibliography

[1] R. V. Pound and G. A. Rebka, Phys. Rev. Lett. **4**, 337 (1960).

[2] W. Potzel, C. Schafer, M. Steiner, H. Karzel, W. Schiessl, M. Peter, G.M. Kalvius, T. Katila, E. Ikonen, P. Helisto and J. Hietaniemi, Hyperfine Interact. **72**, 197 (1992).

[3] G. Gratta, D. E. Kaplan, and S. Rajendran, Phys. Rev. D **102**, 115031 (2020).

[4] R. Lange, N. Huntemann, J. M. Rahm, C. Sanner, H. Shao, B. Lipphardt, Chr. Tamm, S. Weyers, and E. Peik, Phys. Rev. Lett. **126**, 011102 (2021).

[5] V. A. Dzuba, V.V. Flambaum, J. K. Webb , Phys. Rev. Lett. **82**, 888 (1999).

[6] V.A. Dzuba, V.V. Flambaum, and J.K. Webb. Phys. Rev. A **59**, 230 (1999).

[7] V. V. Flambaum and V. A. Dzuba, Can. J. Phys. **87**, 25 (2009).

[8] J. Gu´ena, M. Abgrall, D. Rovera, P. Rosenbusch, M. E. Tobar, P. Laurent, A. Clairon, and S. Bize, Phys. Rev. Lett. **109**, 080801 (2012).

[9] V.V. Flambaum, and A. F. Tedesco, Phys. Rev. C **73**, 055501 (2006).

[10] V. V. Flambaum, Phys. Rev. Lett. **97**, 092502 (2006).

[11] P. Fadeev, J. C. Berengut, and V. V. Flambaum, Phys. Rev. A **102**, 052833 (2020).

[12] C. J. A. P. Martins, Rep. Prog. Phys. **80**, 126902 (2017).

[13] M. S. Safronova, D. Budker, D. DeMille, D. F. J. Kimball, A. Derevianko, and C. W. Clark, Rev. Mod. Phys. **90**, 025008 (2018).

[14] N. Huntemann, B. Lipphardt, C. Tamm, V. Gerginov, S. Weyers, and E. Peik, Phys. Rev. Lett. **113**, 210802 (2014).

[15] V. A. Dzuba, V. V. Flambaum, S. Schiller, Phys. Rev. A **98**, 022501 (2018).

[16] M. S. Safronova, Ann. Phys.(Berlin) **531**, 1800364 (2019).

[17] E. Peik and C. Tamm, Europhys. Lett. **61**, 181 (2003).

[18] C. W. Reich and R. G. Helmer, Phys. Rev. Lett. **64**, 271 (1990).

[19] R. G. Helmer and C. W. Reich, Phys. Rev. C **49**, 1845 (1994).

[20] B. R. Beck, J. A. Becker, P. Beiersdorfer, G. V. Brown, K. J. Moody, J. B. Wilhelmy, F. S. Porter, C. A. Kilbourne, and R. L. Kelley, Phys. Rev. Lett. **98**, 142501 (2007).

[21] B. R. Beck, J. A. Becker, P. Beiersdorfer, G. V. Brown, K. J. Moody, C. Y. Wu, J. B. Wilhelmy, F. S. Porter, C. A. Kilbourne, and R. L. Kelley, Report No. LLNL-PROC-415170 (Los Alamos National Laboratory, 2009).

[22] E. V. Tkalya, C. Schneider, J. Jeet, and E. R. Hudson, Phys. Rev. C **92**, 054324 (2015).

[23] N. Minkov and A. Pálffy, Phys. Rev. Lett. **118**, 212501 (2017).

[24] S. G. Porsev, V. V. Flambaum, E. Peik, and Chr. Tamm, Phys. Rev. Lett **105**,182501 (2010).

[25] C. J. Campbell, A. G. Radnaev, A. Kuzmich, V. A. Dzuba, V. V. Flambaum, and A. Derevianko, Phys. Rev. Lett. **108**, 120802 (2012).

[26] P. G. Thirolf, B. Seiferle, and L. von der Wense, J. Phys. B: At. Mol. Opt. Phys. **52**, 203001 (2019).

[27] L. von der Wense, B. Seiferle, and P. G. Thirolf, Meas. Tech. **60**, 1178 (2018).

[28] E. V. Tkalya, Phys. Rev. Lett. **124**, 242501 (2020).

[29] B. S. Nickerson, M. Pimon, P. V. Bilous, J. Gugler, K. Beeks, T. Sikorsky, P. Mohn, T. Schumm, and A. Pálffy, Phys. Rev. Lett. **125**, 032501 (2020).

[30] S. G. Porsev, V.V. Flambaum, Phys. Rev. A **81**, 032504 (2010).

[31] S.G. Porsev, V.V. Flambaum, Phys. Rev. A **81**, 042516 (2010).

[32] A. Ya. Dzyublik, Phys. Rev. C **102**, 024604 (2020).

[33] B. Seiferle, L. von der Wense, P. V. Bilous, I. Amersdorffer, C. Lemell, F. Libisch, S. Stellmer, T. Schumm, C. E. Düllmann, A. Pálffy, and P. G. Thirolf, Nature **573**, 243 (2019).

[34] T. Masuda, A. Yoshimi, A. Fujieda, H. Fujimoto, H. Haba, H. Hara, T. Hiraki, H. Kaino, Y. Kasamatsu, S. Kitao, K. Konashi, Y. Miyamoto, K. Okai, S. Okubo, N. Sasao, M. Seto, T. Schumm, Y. Shigekawa, K. Suzuki, S. Stellmer, K. Tamasaku, S. Uetake, M. Watanabe, T. Watanabe, Y. Yasuda, A. Yamaguchi, Y. Yoda, T. Yokokita, M. Yoshimura, and K. Yoshimura, Nature **573**, 238 (2019).

[35] A. Yamaguchi, H. Muramatsu, T. Hayashi, N. Yuasa, K. Nakamura, M. Takimoto, H. Haba, K. Konashi, M. Watanabe, H. Kikunaga, K. Maehata, N. Y. Yamasaki, and K. Mitsuda, Phys. Rev. Lett. **123**, 222501 (2019).

[36] T. Sikorsky, J. Geist, D. Hengstler, S. Kempf, L. Gastaldo, C. Enss, C. Mokry, J. Runke, C. E. Düllmann, P. Wobrauschek, K. Beeks, V. Rosecker, J. H. Sterba, G. Kazakov, T. Schumm, and A. Fleischmann, Phys. Rev. Lett. **125**, 142503 (2020).

[37] V.V. Flambaum, R.B. Wiringa, Phys. Rev. C **79**, 034302 (2009).

[38] V.V. Flambaum, N. Auerbach, V.F. Dmitriev EPL (Europhysics Letters) **85**, 50005 (2009).

[39] E. Litvinova, H. Feldmeier, J. Dobaczewski, and V.V. Flambaum, Phys. Rev. C **79**, 064303 (2009).

[40] P.G. Thirolf, B. Seiferle, and L. von der Wense, Ann. Phys.(Berlin) **531**, 1800381 (2019).

[41] J. C. Berengut and V. V. Flambaum, Nuclear Physics News **20**, 19 (2010).

[42] K. Beeks, T. Sikorsky, T. Schumm, J. Thielking, M. V. Okhapkin, and E. Peik, Nat. Rev. Phys. (2021).

[43] Y. V. Stadnik and V. V. Flambaum, Phys. Rev. Lett. **115**, 201301 (2015).

[44] N. Leefer, A. Gerhardus, D. Budker, V. V. Flambaum, Y. V. Stadnik, Phys. Rev. Lett. **117**, 271601 (2016).

[45] A. Arvanitaki, J. Huang, and K. Van Tilburg, Phys. Rev. D **91**, 015015 (2015).

[46] A. Banerjee, D. Budker, J. Eby, V. V. Flambaum, H. Kim, O. Matsedonsky, and G. Perez, JHEP **2020**, 4 (2020).

[47] J. C. Berengut, V. A. Dzuba, V. V. Flambaum, and S. G. Porsev, Phys. Rev. Lett. **102**, 210801 (2009).

[48] C. Lyu, S. M. Cavaletto, C. H. Keitel, and Z. Harman, Phys. Rev. Lett. **125**, 093201 (2020).

[49] J. C. Berengut, Phys. Rev. Lett. **121**, 253002 (2018).

[50] D. Hinneburg. Z. Phys. A **300**, 129 (1981).

[51] I. Angeli and K. P. Marinova, At. Data Nucl. Data Tables **99**, 69 (2013).

[52] Preliminary results of this ^{235}U calculation have been presented in the undergraduate research thesis by S. Bladwell, 2011 (unpublished).

[53] N. J. Stone, At. Data Nucl. Data Tables **111–112**, 1 (2016).

[54] M. Filatov, Coord. Chem. Rev. **253**, 594 (2009).

[55] G. M. Kalvius and G. K. Shenoy, At. Data Nucl. Data Tables **14**, 639 (1974).

[56] F. Buheitel, W. Potzel and D. C. Aumann, Hyperfine Interact. **47/48**, 606 (1989).

[57] A. Svane, Phys. Rev. B **68**, 064422 (2003).

[58] Y. Tanaka, R. M. Steffen, E. B. Shera, W. Reuter, M. V. Hoehn, and J. D. Zumbro, Phys. Rev. C **29**, 1897 (1984).

[59] J. Hess, Nucl. Phys. A **142**, 273 (1970).

[60] J. Thielking, M. V. Okhapkin, P. Glowacki, D. M. Meier, L. von der Wense, B. Seiferle, C. E. Düllmann, P. G. Thirolf, and E. Peik, Nature **556**, 321 (2018).

[61] The estimate of this number appears in Appendix A.

Chapter 4

Revisiting spin-dependent forces mediated by new bosons: Potentials in the coordinate-space representation for macroscopic- and atomic-scale experiments

Phys. Rev. A **99**, 022113 (2019)

Pavel Fadeev[1], Yevgeny V. Stadnik[1], Filip Ficek[2], Mikhail G. Kozlov[3,4], Victor V. Flambaum[1,5], and Dmitry Budker[1,6,7]

[1] *Helmholtz Institute Mainz, Johannes Gutenberg University, 55099 Mainz, Germany*
[2] *Institute of Physics, Jagiellonian University, Łojasiewicza 11, 30-348 Kraków, Poland*
[3] *Petersburg Nuclear Physics Institute of NRC "Kurchatov Institute", Gatchina 188300, Russia*
[4] *St. Petersburg Electrotechnical University LETI, Prof. Popov Str. 5, 197376 St. Petersburg, Russia*
[5] *School of Physics, University of New South Wales, Sydney, New South Wales 2052, Australia*
[6] *Department of Physics, University of California at Berkeley, Berkeley, California 94720-7300, USA*
[7] *Nuclear Science Division, Lawrence Berkeley National Laboratory, Berkeley, California 94720, USA*

The exchange of spin-0 or spin-1 bosons between fermions or spin-polarised macroscopic objects gives rise to various spin-dependent potentials. We derive the coordinate-space non-relativistic potentials induced by the exchange of such bosons, including contact terms that can play an important role in atomic-scale phenomena, and correct for errors and omissions in the literature. We summarise the properties of the potentials and their relevance for various types of experiments. These potentials underpin the interpretation of experiments that search for new bosons, including spectroscopy, torsion-pendulum measurements, magnetometry, parity nonconservation and electric dipole moment experiments.

4.1 Introduction

There are four known types of interactions in nature — electromagnetic, strong, weak and gravitational. Still, additional interactions may exist. For example, the exchange of a new

spin-0 or spin-1 boson between two fermions produces a plethora of "exotic" interaction potentials [1]. Yet-to-be-discovered bosons may solve several outstanding puzzles. The axion (a spin-0 boson) may explain the apparent absence of CP violation in strong interactions [2–9]. The observed dark matter [10] and dark energy [11] may also be explained by the existence of new bosonic particles. The possibility to solve such central questions motivates numerous searches for new bosons. Recent examples of searches for new forces mediated by such bosons can be found in Refs. [12–52].

In Ref. [53] (see also the earlier papers [54, 55]), the three distinct non-relativistic potentials arising from the exchange of a spin-0 boson between spin-polarised and spin-unpolarised bodies were presented. Later, Ref. [1] expanded this list to include additional long-range non-relativistic potentials arising from the exchange of spin-0 bosons and spin-1 bosons (such as Z' bosons and paraphotons). These potentials were presented in Ref. [1] in a mixed momentum- and coordinate-space representation, which is convenient when the relative velocity between two bodies can be described by a classical vector, such as in the macroscopic-scale experiments of Refs. [28, 35, 42, 52]. However, in phenomena that arise on the (sub)atomic scale, the relative velocity between two particles can no longer be described by a classical vector, but must instead be described by a quantum vector operator (see, for example, [41, 44, 51]).

Furthermore, the potentials induced by the exchange of bosons in general contain not only long-range terms, but also short-range (contact) terms, which can play an important role in atomic-scale experiments. For example, the usual magnetic dipole-dipole interaction between atomic electrons and the nucleus (mediated by the exchange of photons) contains both long-range and contact terms. For atomic states with zero electron orbital angular momentum (which are described by spherically symmetric wavefunctions), the expectation value of the long-range part of the magnetic dipole-dipole interaction vanishes and the entire contribution to the hyperfine energy shift comes from the contact part of the magnetic interaction [56].

In the present paper, we derive the coordinate-space non-relativistic potentials, including contact terms. These potentials are particularly important in searches for new spin-dependent forces based on atomic-scale experiments (such as in [41, 49]) and on macroscopic-scale experiments [13, 16, 28, 35, 42, 52]. In atomic systems that satisfy $Z\alpha \ll 1$, where Z is the nuclear charge and $\alpha \approx 1/137$ is the fine-structure constant at zero momentum transfer, the velocities of the particles are small. For example, in atomic hydrogen, the expectation value of the square of the velocity of the electron orbiting the nucleus (in natural relativistic units, $\hbar = c = 1$) is $\langle v^2 \rangle \sim \alpha^2 \sim 10^{-4}$. In macroscopic-scale experiments that search for velocity-dependent effects due to the relative motion of Earth and the Sun, the square of the relative velocity is $v^2 \sim 10^{-8}$.

The structure of this paper is as follows. In Sec. 4.2, we derive the coordinate-space non-relativistic potentials induced by the exchange of spin-0 and spin-1 bosons. In Sec. 4.3, we discuss the properties and nuances of these potentials, and point out several erroneous results and omissions in the earlier literature. Some of the more technical details are presented in the Appendices.

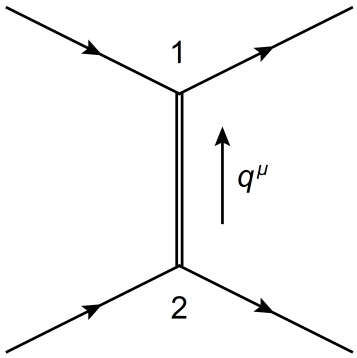

Figure 4.1: *Elastic scattering of two fermions with masses m_1 and m_2 and spins $\boldsymbol{s}_1$ and $\boldsymbol{s}_2$, respectively, mediated by a boson of mass M with four-momentum q^μ that is transferred from fermion 2 to fermion 1.*

4.2 Coordinate-space potentials

Consider the elastic scattering of two fermions with masses m_1 and m_2 and spins $\boldsymbol{s}_1$ and $\boldsymbol{s}_2$, respectively, mediated by a boson of mass M with four-momentum q^μ that is transferred from fermion 2 to fermion 1 (Fig. 4.1). We focus on three types of bosons in the present work — a spin-0 boson ϕ (which can be either massive or massless), a massive spin-1 boson Z' and a massless spin-1 boson γ'. Each boson has its own set of local Lorentz-invariant interactions with the standard-model fermions ψ [1, 57]:

$$\mathcal{L}_\phi = \phi \sum_\psi \bar{\psi} \left(g^s_\psi + i\gamma_5 g^p_\psi \right) \psi \,, \tag{4.1}$$

$$\mathcal{L}_{Z'} = Z'_\mu \sum_\psi \bar{\psi}\gamma^\mu \left(g^V_\psi + \gamma_5 g^A_\psi \right) \psi \,, \tag{4.2}$$

$$\mathcal{L}_{\gamma'} = \frac{v_h}{\Lambda^2} P_{\mu\nu} \sum_\psi \bar{\psi}\sigma^{\mu\nu} \left[\mathrm{Re}(C_\psi) + i\gamma_5 \mathrm{Im}(C_\psi) \right] \psi \,. \tag{4.3}$$

Here ψ denotes the fermion field (for instance, $\psi = e$ for an electron, and $\psi = N$ for a nucleon), $P_{\mu\nu} = \partial_\mu A_\nu - \partial_\nu A_\mu$ is the field strength tensor of the massless paraphoton field A_μ, $\sigma^{\mu\nu} = \frac{i}{2}[\gamma^\mu, \gamma^\nu]$, and γ^μ, $\gamma_5 = i\gamma^0\gamma^1\gamma^2\gamma^3$ are Dirac matrices. The dimensionless interaction constants g^s_ψ, g^p_ψ, g^V_ψ, g^A_ψ, $\mathrm{Re}(C_\psi)$, $\mathrm{Im}(C_\psi)$ parametrise the scalar, pseudoscalar, vector, pseudovector, tensor and pseudotensor interaction strengths, respectively. The Higgs vacuum expectation value is denoted by v_h, and Λ is the ultraviolet energy cutoff scale for Lagrangian (4.3).

We have chosen the interactions in Eqs. (4.1) – (4.3), since this set of interactions spans the full space of Lorentz-invariant Dirac operators. The case of a massive spin-1 boson is distinguished from the case of a massless spin-1 boson by the presence of a longitudinal polarisation, and so we treat the massless and massive cases separately.

We derive the coordinate-space non-relativistic potentials associated with the interactions in Eqs. (4.1) – (4.3) by applying the Feynman diagrammatic technique, which is described

in detail in standard textbooks [58, 59]. We summarise our conventions, along with useful identities and Fourier transforms in Appendices 4.4 – 4.6. We present the detailed derivations of three potentials in Appendix 4.7.

Each of the Lagrangians in Eqs. (4.1) – (4.3) contains a sum of two terms, which correspond to two types of vertices. There are three distinct combinations of these two vertices for the scattering of two fermions, and so each Lagrangian can give rise to three distinct potentials. In total, the following nine non-relativistic potentials result:

$$V_{ss}(\mathbf{r}) = -g_1^s g_2^s \underbrace{\frac{e^{-Mr}}{4\pi r}}_{\mathcal{V}_1}, \tag{4.4}$$

$$V_{ps}(\mathbf{r}) = -g_1^p g_2^s \underbrace{\boldsymbol{\sigma}_1 \cdot \hat{\mathbf{r}} \left(\frac{1}{r^2} + \frac{M}{r}\right) \frac{e^{-Mr}}{8\pi m_1}}_{\mathcal{V}_{9,10}}, \tag{4.5}$$

$$V_{pp}(\mathbf{r}) = -\frac{g_1^p g_2^p}{4} \underbrace{\left[\boldsymbol{\sigma}_1 \cdot \boldsymbol{\sigma}_2 \left[\frac{1}{r^3} + \frac{M}{r^2} + \frac{4\pi}{3}\delta(\mathbf{r})\right] - (\boldsymbol{\sigma}_1 \cdot \hat{\boldsymbol{r}})\,(\boldsymbol{\sigma}_2 \cdot \hat{\mathbf{r}}) \left[\frac{3}{r^3} + \frac{3M}{r^2} + \frac{M^2}{r}\right]\right] \frac{e^{-Mr}}{4\pi m_1 m_2}}_{\mathcal{V}_3}, \tag{4.6}$$

$$\begin{aligned} V_{VV}(\mathbf{r}) =& g_1^V g_2^V \underbrace{\frac{e^{-Mr}}{4\pi r}}_{\mathcal{V}_1} \\ &+ \frac{g_1^V g_2^V}{4} \underbrace{\left[\boldsymbol{\sigma}_1 \cdot \boldsymbol{\sigma}_2 \left[\frac{1}{r^3} + \frac{M}{r^2} + \frac{M^2}{r} - \frac{8\pi}{3}\delta(\mathbf{r})\right] - (\boldsymbol{\sigma}_1 \cdot \hat{\mathbf{r}})\,(\boldsymbol{\sigma}_2 \cdot \hat{\mathbf{r}}) \left[\frac{3}{r^3} + \frac{3M}{r^2} + \frac{M^2}{r}\right]\right] \frac{e^{-Mr}}{4\pi m_1 m_2}}_{\mathcal{V}_2+\mathcal{V}_3}, \end{aligned} \tag{4.7}$$

$$V_{AV}(\mathbf{r}) = g_1^A g_2^V \underbrace{\boldsymbol{\sigma}_1 \cdot \left\{\frac{\boldsymbol{p}_1}{m_1} - \frac{\boldsymbol{p}_2}{m_2}, \frac{e^{-Mr}}{8\pi r}\right\}}_{\mathcal{V}_{12,13}} - \frac{g_1^A g_2^V}{2} \underbrace{(\boldsymbol{\sigma}_1 \times \boldsymbol{\sigma}_2) \cdot \hat{\mathbf{r}} \left(\frac{1}{r^2} + \frac{M}{r}\right) \frac{e^{-Mr}}{4\pi m_2}}_{\mathcal{V}_{11}}, \tag{4.8}$$

$$\begin{aligned} V_{AA}(\mathbf{r}) =& - g_1^A g_2^A \underbrace{\boldsymbol{\sigma}_1 \cdot \boldsymbol{\sigma}_2 \frac{e^{-Mr}}{4\pi r}}_{\mathcal{V}_2} \\ &- \frac{g_1^A g_2^A m_1 m_2}{M^2} \underbrace{\left[\boldsymbol{\sigma}_1 \cdot \boldsymbol{\sigma}_2 \left[\frac{1}{r^3} + \frac{M}{r^2} + \frac{4\pi}{3}\delta(\mathbf{r})\right] - (\boldsymbol{\sigma}_1 \cdot \hat{\mathbf{r}})\,(\boldsymbol{\sigma}_2 \cdot \hat{\mathbf{r}}) \left[\frac{3}{r^3} + \frac{3M}{r^2} + \frac{M^2}{r}\right]\right] \frac{e^{-Mr}}{4\pi m_1 m_2}}_{\mathcal{V}_3}, \end{aligned} \tag{4.9}$$

$$V_{TT}(\mathbf{r}) = \frac{4v_h^2 \mathrm{Re}(C_1)\mathrm{Re}(C_2) m_1 m_2}{\Lambda^4} \underbrace{\left[\boldsymbol{\sigma}_1 \cdot \boldsymbol{\sigma}_2 \left[\frac{1}{r^3} - \frac{8\pi}{3}\delta(\mathbf{r})\right] - (\boldsymbol{\sigma}_1 \cdot \hat{\mathbf{r}})(\boldsymbol{\sigma}_2 \cdot \hat{\mathbf{r}}) \frac{3}{r^3}\right] \frac{1}{4\pi m_1 m_2}}_{\mathcal{V}_2+\mathcal{V}_3}, \tag{4.10}$$

$$\begin{aligned} V_{\tilde{T}T}(\mathbf{r}) =& \frac{4v_h^2 \mathrm{Im}(C_1)\mathrm{Re}(C_2) m_1 m_2}{\Lambda^4} \underbrace{\left[(\boldsymbol{\sigma}_1 \times \boldsymbol{\sigma}_2) \cdot \left\{\frac{\boldsymbol{p}_1}{m_1} - \frac{\boldsymbol{p}_2}{m_2}, \frac{1}{r^3} + \frac{4\pi}{3}\delta(\mathbf{r})\right\}\right] \frac{1}{8\pi m_1 m_2}}_{\mathcal{V}_{14}} \\ &+ \frac{4v_h^2 \mathrm{Im}(C_1)\mathrm{Re}(C_2) m_1 m_2}{\Lambda^4} \underbrace{\left\{\left(\frac{\boldsymbol{p}_1}{m_1} - \frac{\boldsymbol{p}_2}{m_2}\right)_i, \frac{3(\boldsymbol{\sigma}_1 \cdot \hat{\mathbf{r}})(\boldsymbol{\sigma}_2 \times \hat{\mathbf{r}})_i}{8\pi m_1 m_2 r^3}\right\}}_{\mathcal{V}_{15}} \\ &- \frac{2v_h^2 \mathrm{Im}(C_1)\mathrm{Re}(C_2) m_1 m_2}{\Lambda^4} \underbrace{\frac{\boldsymbol{\sigma}_1 \cdot [\boldsymbol{\nabla}\delta(\mathbf{r})]}{m_1 m_2^2}}_{\mathcal{V}_{9,10}}, \end{aligned} \tag{4.11}$$

$$V_{\tilde{T}\tilde{T}}(\mathbf{r}) = \frac{4v_h^2 \mathrm{Im}(C_1)\mathrm{Im}(C_2) m_1 m_2}{\Lambda^4} \underbrace{\left[\boldsymbol{\sigma}_1 \cdot \boldsymbol{\sigma}_2 \left[\frac{1}{r^3} + \frac{4\pi}{3}\delta(\mathbf{r})\right] - (\boldsymbol{\sigma}_1 \cdot \hat{\mathbf{r}})(\boldsymbol{\sigma}_2 \cdot \hat{\mathbf{r}}) \frac{3}{r^3}\right] \frac{1}{4\pi m_1 m_2}}_{\mathcal{V}_3}. \tag{4.12}$$

In these expressions, $\boldsymbol{\sigma}_1$ and $\boldsymbol{\sigma}_2$ denote the Pauli spin-matrix vectors of the two fermions, $\hat{\mathbf{r}}$ is the unit vector directed from fermion 2 to fermion 1, r is the distance between the two fermions, and $\{A, B\} \equiv AB + BA$ is the anticommutator of two operators A and B. The momenta $\boldsymbol{p}_1 = -i\boldsymbol{\nabla}_1$ and $\boldsymbol{p}_2 = -i\boldsymbol{\nabla}_2$ are vector differential operators in coordinate space.

For the sake of comparison with previous literature, we matched the individual terms in Eqs. (4.4) – (4.12) onto the $\mathcal{V}_i$ potential terms of Ref. [1]. In the momentum-space representation, the spin-momentum structures of $\mathcal{V}_2$ in Eq. (4.7), $\mathcal{V}_{9,10}$ in Eq. (4.11), and $\mathcal{V}_{14}$ in Eq. (4.11) are multiplied by $\boldsymbol{q}^2$, the square of the spatial components of the transferred momentum. Thus, although $\mathcal{V}_{9,10}$ has different forms in Eqs. (4.5) and (4.11), the underlying spin-momentum structure of these potential terms in the momentum-space representation is the same up to a factor of $\boldsymbol{q}^2$.

The potentials in Eqs. (4.5), (4.8), and (4.11) are written in an abbreviated form lacking symmetry under the permutation of particle indices $1 \leftrightarrow 2$. In the case of these potentials, we must add the terms obtained by permuting the particle indices $1 \leftrightarrow 2$.

Once the above terms are added, the potentials in Eqs. (4.4) – (4.12) are symmetric with respect to the permutation of particle indices $1 \leftrightarrow 2$, and hence do not vanish for identical particles. In order to determine whether or not specific matrix elements of the potentials in Eqs. (4.4) – (4.12) vanish for identical particles, one needs to take into account the fact that the overall wavefunction of indistinguishable fermions is antisymmetric under permutation of fermions.

We note that Eqs. (4.4) – (4.12) contain fewer than the 16 terms presented in Ref. [1], since we are interested in the non-relativistic limit. For example, the $\mathcal{V}_8$ term of Ref. [1] arises

as an $\mathcal{O}(v^2)$ relativistic correction to the $\mathcal{V}_2$ term in Eq. (5.1) and hence can be neglected in non-relativistic systems.

We have chosen to sort the potentials in Eqs. (4.4) – (4.12) by their types of physical couplings, in contrast to sorting them into 16 groups by their mathematical spin-momentum structure as in [1]. We believe that our classification is more useful from a physicist's point of view, since one is ultimately interested in the physical coupling constants of a particular model.

Other representations of these coordinate-space potentials are possible. In Appendix 4.8, we present these potentials in a semi-relativistic form that is convenient for numerical atomic calculations using Dirac-Hartree-Fock wavefunctions.

4.3 Discussion

We first point out a number of erroneous results and omissions in the earlier literature:

(1) Regarding the overall sign of the pseudoscalar-pseudoscalar potential in Eq. (5.3), we agree with the calculations of Refs. [1, 60], correcting the earlier sign error in Ref. [53].

(2) The overall signs of the tensor-type potentials in Eqs. (4.10), (4.11) and (4.12) are opposite to those in Ref. [1].

(3) The M^2/r term in $\mathcal{V}_2 + \mathcal{V}_3$ of the vector-vector potential in Eq. (4.7), which arises together with a contact term, was omitted in Ref. [1].

(4) The $\mathcal{V}_3$ term (omitted in Ref. [1]) in the pseudovector-pseudovector potential in Eq. (5.1) arises from a longitudinal polarisation mode for a massive spin-1 boson and nonconservation of the axial-vector current. Here we agree with the recent calculation of Ref. [61]. This term seems to tend to infinity in the limit of the boson mass $M \to 0$ and so it looks like the assumptions of perturbation theory are no longer justified (formally speaking, there is a violation of the perturbative unitarity bound), similarly to the violation of the perturbative unitarity bound in the high-energy scattering of longitudinal W and Z bosons in the standard model without a Higgs boson.

It is instructive to consider what occurs in a renormalisable theory, such as the standard model. In this case, the combination of parameters $g_1^A g_2^A/M^2$ remains finite as $M \to 0$. As an example, let us consider the case of Z boson exchange between two fermions, where the Z boson has purely pseudovector interactions and does not mix with the photon (i.e., $\sin(\theta_W) = 0$, where θ_W is the weak mixing angle). In this case, the Z boson mass is given by $M = gv/2$, where v is the Higgs vacuum expectation value and g is the (universal) electroweak interaction constant [62]. In order for the fermion masses, given by $m_f = fv/\sqrt{2}$ (f is a species-dependent interaction constant), to remain finite as $M \to 0$, v must also remain finite. Hence $g^2/M^2 = 4/v^2$ is independent of M and remains finite as $M \to 0$. In such a regime, when the $\mathcal{V}_3$ term in Eq. (5.1) gives the dominant contribution, it is appropriate to place constraints on the combination of parameters $g_1^A g_2^A/M^2$. The relation to the renormalisability of the theory makes such a case especially interesting to study.

In the special case of a massless vector boson, $M = 0$, Eq. (5.1) simplifies to solely the $\mathcal{V}_2$ term. In contrast to a massive vector boson, a massless vector boson does not have a

Table 4.1: *Properties of non-relativistic potentials induced by the exchange of spin-0 and spin-1 bosons.*

Property	$\mathcal{V}_1$	$\mathcal{V}_2$	$\mathcal{V}_3$	$\mathcal{V}_2+\mathcal{V}_3$	$\mathcal{V}_{9,10}$	$\mathcal{V}_{11}$	$\mathcal{V}_{12,13}$	$\mathcal{V}_{14}$	$\mathcal{V}_{15}$
Parity,	+	+	+	+	−	−	−	−	−
Time-reversal symmetry	+	+	+	+	−	+	+	−	−
Velocity dependence	−	−	−	−	−	−	+	+	+
First-order energy shift	+	+	+	+	−	−	−	−	−
Mediated by spin-0 boson	+	−	+	−	+	−	−	−	−
Mediated by massive spin-1	+	+	+	+	−	+	+	−	−
Mediated by paraphoton	−	−	+	+	+	−	−	+	+

longitudinal polarisation mode, and hence there is no $\mathcal{V}_3$ term in Eq. (5.1) for the special case $M = 0$.

In light of the above, we believe it is worthwhile to reanalyse some earlier experiments (see, for example, [33, 35, 42, 48]) using the corrected potentials presented in the present paper and also to note the results of our paper for future experiments.

Additionally, we note that it is possible to write certain potentials in a form where some of their constituent "bare" terms, namely with the interaction constants (which also contain particle indices) removed, are antisymmetric with respect to the permutation of particle indices $1 \leftrightarrow 2$. For example, instead of writing the scalar-pseudoscalar potential in Eq. (4.5) in the form $V_{ps}(\mathbf{r}) = C_1\boldsymbol{\sigma}_1\cdot\hat{\mathbf{r}} + C_2\boldsymbol{\sigma}_2\cdot\hat{\mathbf{r}}$, where C_1 and C_2 can be identified from Eq. (4.5), the authors of [1] choose to write the same expression in the form $\tilde{C}_1\,(\boldsymbol{\sigma}_1+\boldsymbol{\sigma}_2)\cdot\hat{\mathbf{r}} + \tilde{C}_2\,(\boldsymbol{\sigma}_1-\boldsymbol{\sigma}_2)\cdot\hat{\mathbf{r}}$, where $C_1 = \tilde{C}_1 + \tilde{C}_2$ and $C_2 = \tilde{C}_1 - \tilde{C}_2$. Here, one of the bare terms is symmetric under permutation of fermions, while the other is antisymmetric. The authors of [1] note that only one combination of $\boldsymbol{\sigma}_1 \pm \boldsymbol{\sigma}_2$ survives for identical fermions. One should take this into account when searching for effects of spin-dependent forces between identical fermions. For instance, the authors of [33] present constraints on the antisymmetric potentials V_7, V_{15} and V_{16} for electrons, even though such potentials vanish for two identical fermions.

We summarise the properties of the non-relativistic potentials induced by the exchange of spin-0 and spin-1 bosons in Table 4.1. Several nuances of these potentials are also worth discussing. In macroscopic-scale experiments, the momentum and radial vectors appearing in Eqs. (4.4) – (4.12) may be treated as classical vectors, and symmetrised expressions such as $\{\boldsymbol{p}, f(r)\}$ may be replaced by their classical value, $\{\boldsymbol{p}, f(r)\} \to 2\boldsymbol{p}f(r)$. In atomic-scale experiments, however, the momentum and radial vectors need to be treated as quantum operators, and explicit symmetrisation in expressions such as $\{\boldsymbol{p}, f(r)\}$ must be retained.

Another difference between macroscopic-scale and atomic-scale experiments in relation to spin-dependent potentials is the manifestation of the parity- and/or time-reversal-invariance-violating nature of these potentials. Consider the P,T-violating correlation $\boldsymbol{\sigma}\cdot\hat{\mathbf{r}}$ in the term $\mathcal{V}_{9,10}$ in Eq. (4.5). In macroscopic-scale experiments, $\hat{\mathbf{r}}$ is a classical vector directed between macroscopically-separated bodies, and the interaction $\boldsymbol{\sigma}\cdot\hat{\mathbf{r}}$ causes the fermion spins to precess about the vector $\hat{\mathbf{r}}$ [12, 15, 25, 39, 43, 47]. In this sense, the macroscopic interaction $\boldsymbol{\sigma}\cdot\hat{\mathbf{r}}$ is reminiscent of the interaction of a fermion magnetic moment with a magnetic field. In atomic-scale experiments, $\hat{\mathbf{r}}$ is a radial operator directed between atomic electrons and nucleons, and

so the correlation $\boldsymbol{\sigma}\cdot\hat{\mathbf{r}}$ mixes atomic states of opposite parity and gives rise to atomic electric dipole moments [46, 51, 54]. Specific details of how electric dipole moments are induced in atoms and molecules as a result of the P,T-violating potential term $\mathcal{V}_{9,10}$ can be found in Refs. [46, 51]. Electric dipole moments in atoms and molecules can also be similarly induced as a result of the P,T-violating potential terms $\mathcal{V}_{14}$ and $\mathcal{V}_{15}$. Both atomic- and macroscopic-scale measurements involve spin precession. However, the spin precession takes place about different sets of vectors. In macroscopic-scale experiments, spin precession takes place about the vectors $\boldsymbol{B}$ and $\hat{\mathbf{r}}$, while in atomic-scale experiments, spin precession takes place about the vectors $\boldsymbol{B}$ and $\boldsymbol{E}$.

Finally, some of the potentials in Eqs. (4.4) – (5.1) may not be practical for numerical atomic calculations in their presented form for boson masses $M > m_1, m_2$. For example, in the case of a hydrogenlike system in a state with zero electron orbital angular momentum, the expectation value of the operator in Eq. (5.3) vanishes in the limit $M \to \infty$. In this limit, we have $e^{-Mr}/r \to 4\pi\delta(\mathbf{r})/M^2$. This $\delta(\mathbf{r})$ term cancels the $\delta(\mathbf{r})$ term inside the leftmost brackets in Eq. (5.3), after integrating over the angular coordinates (likewise, the other terms in Eq. (5.3) cancel for an arbitrary boson mass, after integrating over angular coordinates).

Numerically, this cancellation is hard to achieve. Finite numerical precision becomes insufficient at arbitrarily large boson masses, leading to problems in numerical calculations. To circumvent such issues, one can instead write Eq. (5.3) in the following equivalent form [which appears in an intermediate step of the derivation of the potential via Eq. (4.24)]:

$$V_{pp}(\mathbf{r}) = \frac{g_1^p g_2^p}{16\pi m_1 m_2}\,(\boldsymbol{\sigma}_1\cdot\boldsymbol{\nabla})\,(\boldsymbol{\sigma}_2\cdot\boldsymbol{\nabla})\left(\frac{e^{-Mr}}{r}\right), \tag{4.13}$$

and use integration by parts when calculating matrix elements of this operator. A similar situation occurs in Eq. (5.1).

Note that as $M \to \infty$, matrix elements of Eq. (5.6) scale as $\propto 1/M^2$. This is a general property of the potentials in Eqs. (4.4) – (5.1), whose terms scale as $\propto 1/M^2$ (or faster) in the limit $M \to \infty$. One can see this property more clearly in the semi-relativistic form of the potentials presented in Appendix 4.8.

In Eq. (4.7), in addition to $\mathcal{V}_3$ of Eq. (5.3) there is a contribution of $\mathcal{V}_2$ which is equivalent in form to:

$$\frac{g_1^V g_2^V}{16\pi m_1 m_2}\boldsymbol{\sigma}_1\cdot\boldsymbol{\sigma}_2\Delta\left(\frac{e^{-Mr}}{r}\right). \tag{4.14}$$

This expression results in two terms, by Eq. (4.23) in Appendix 4.6, which cancel as $M \to \infty$ in a similar manner as above. Likewise, Eq. (4.5) can be written as:

$$V_{ps}(\boldsymbol{r}) = \frac{g_1^p g_2^s}{8\pi m_1}\,(\boldsymbol{\sigma}_1\cdot\boldsymbol{\nabla})\left(\frac{e^{-Mr}}{r}\right), \tag{4.15}$$

thus highlighting its scaling $\propto 1/M^2$ as $M \to \infty$.

To summarise, we have derived the coordinate-space non-relativistic potentials induced by the exchange of spin-0 and spin-1 bosons, including contact terms that can play an important role in atomic-scale experiments. In the process, we have corrected for various errors and

omissions in the earlier literature. These potentials are important for the interpretation of numerous experiments, including spectroscopy, torsion-pendulum, magnetometry, parity-nonconservation and electric-dipole-moment experiments, in the search for new bosons.

Acknowledgments

We thank Derek Jackson Kimball, Szymon Pustelny, and Eric Adelberger for their valuable remarks. The authors acknowledge the support by the DFG Reinhart Koselleck project, the European Research Council Dark-OsT advanced grant under project ID 695405, and the Simons and the Heising-Simons Foundations. F.F. has been supported by the Polish Ministry of Science and Higher Education within the Diamond Grant (Grant No. 0143/DIA/2016/45). V.V.F. was supported by the Australian Research Council (ARC) and the JGU Gutenberg Research Fellowship. M.G.K. is supported by FQXi mini grant 2017-171370 and is grateful to JGU for hospitality. Y.V.S. was supported by the Humboldt Research Fellowship.

4.4 Units and conventions

We employ the natural relativistic units $\hbar = c = 1$ and the metric signature $(+---)$. We label space-time and spatial coordinates with Greek and Latin indices, respectively. We employ the Einstein summation convention for repeated indices. We use the following representation of the Dirac matrices:

$$\gamma^0 = \begin{bmatrix} 1 & 0 \\ 0 & -1 \end{bmatrix} , \ \gamma^i = \begin{bmatrix} 0 & \sigma_i \\ -\sigma_i & 0 \end{bmatrix} , \ \gamma_5 = \begin{bmatrix} 0 & 1 \\ 1 & 0 \end{bmatrix} , \tag{4.16}$$

where σ_i is the i^{th} Pauli matrix.

4.5 Useful identities

$$[\sigma_i, \sigma_j] = 2i\varepsilon_{ijk}\sigma_k \, , \tag{4.17}$$

$$\{\sigma_i, \sigma_j\} = 2\delta_{ij} \, , \tag{4.18}$$

$$\varepsilon_{ijk}\varepsilon^{imn} = \delta_j^m \delta_k^n - \delta_j^n \delta_k^m \, , \tag{4.19}$$

$$(\boldsymbol{A} \times \boldsymbol{B}) \cdot (\boldsymbol{C} \times \boldsymbol{D}) = (\boldsymbol{A} \cdot \boldsymbol{C})(\boldsymbol{B} \cdot \boldsymbol{D}) - (\boldsymbol{B} \cdot \boldsymbol{C})(\boldsymbol{A} \cdot \boldsymbol{D}) \, . \tag{4.20}$$

4.6 Fourier transforms

$$\int \frac{d^3q}{(2\pi)^3} \frac{e^{i\boldsymbol{q}\cdot\mathbf{r}}}{M^2 + |\boldsymbol{q}|^2} = \frac{e^{-Mr}}{4\pi r} \, , \tag{4.21}$$

$$\int \frac{d^3q}{(2\pi)^3} \frac{(\boldsymbol{\sigma}\cdot\boldsymbol{q})\, e^{i\boldsymbol{q}\cdot\boldsymbol{r}}}{M^2 + |\boldsymbol{q}|^2} = -i\,(\boldsymbol{\sigma}\cdot\boldsymbol{\nabla}) \left(\frac{e^{-Mr}}{4\pi r} \right) , \tag{4.22}$$

$$\int \frac{d^3q}{(2\pi)^3} \frac{|\boldsymbol{q}|^2 \, e^{i\boldsymbol{q}\cdot\boldsymbol{r}}}{M^2+|\boldsymbol{q}|^2} = \left[\delta(\boldsymbol{r}) - \frac{M^2}{4\pi r}\right] e^{-Mr}\,, \tag{4.23}$$

$$\begin{aligned}\int \frac{d^3q}{(2\pi)^3} \frac{(\boldsymbol{\sigma}_1\cdot\boldsymbol{q})\,(\boldsymbol{\sigma}_2\cdot\boldsymbol{q})\, e^{i\boldsymbol{q}\cdot\boldsymbol{r}}}{M^2+|\boldsymbol{q}|^2} = \\ \frac{\boldsymbol{\sigma}_1\cdot\boldsymbol{\sigma}_2}{4\pi}\left[\frac{1}{r^3}+\frac{M}{r^2}+\frac{4\pi}{3}\delta(\boldsymbol{r})\right] e^{-Mr} \\ -\frac{(\boldsymbol{\sigma}_1\cdot\hat{\boldsymbol{r}})\,(\boldsymbol{\sigma}_2\cdot\hat{\boldsymbol{r}})}{4\pi}\left[\frac{3}{r^3}+\frac{3M}{r^2}+\frac{M^2}{r}\right] e^{-Mr}\,,\end{aligned} \tag{4.24}$$

$$\int \frac{d^3q}{(2\pi)^3} \frac{e^{i\boldsymbol{q}\cdot\boldsymbol{r}}}{|\boldsymbol{q}|^2} = \frac{1}{4\pi r}\,, \tag{4.25}$$

$$\int \frac{d^3q}{(2\pi)^3} e^{i\boldsymbol{q}\cdot\boldsymbol{r}} = \delta(\boldsymbol{r})\,, \tag{4.26}$$

$$\int \frac{d^3q}{(2\pi)^3} \frac{q_k q_l e^{i\boldsymbol{q}\cdot\boldsymbol{r}}}{|\boldsymbol{q}|^2} = \frac{1}{4\pi}\left[\frac{\delta_{kl}}{r^3} - 3\frac{r_k r_l}{r^5} + \frac{4\pi}{3}\delta_{kl}\delta(\boldsymbol{r})\right]\,, \tag{4.27}$$

$$\int \frac{d^3q}{(2\pi)^3} \boldsymbol{q} e^{i\boldsymbol{q}\cdot\boldsymbol{r}} = -i\boldsymbol{\nabla}\delta(\boldsymbol{r})\,, \tag{4.28}$$

$$\int \frac{d^3q}{(2\pi)^3} |\boldsymbol{q}|^2 \, e^{i\boldsymbol{q}\cdot\boldsymbol{r}} = -\Delta\delta(\boldsymbol{r})\,. \tag{4.29}$$

4.7 Calculating coordinate-space potentials – Three examples

1 – Pseudoscalar-scalar potential

Applying the Feynman rules to the tree-level process in Fig. 4.1 with vertex 1 being of the pseudoscalar type and vertex 2 being of the scalar type in Lagrangian (4.1), gives the amplitude:

$$\begin{aligned}\mathcal{M}(q) =& i\left[i^2\bar{u}(\boldsymbol{p}_{1,f})\gamma_5 g_1^p u(\boldsymbol{p}_{1,i})\right]\left[i\bar{u}(\boldsymbol{p}_{2,f}) g_2^s u(\boldsymbol{p}_{2,i})\right] \\ &\times\left[\frac{-i}{M^2-q^2}\right]\,,\end{aligned} \tag{4.30}$$

where $q = p_{1,f} - p_{1,i} = p_{2,i} - p_{2,f}$ is the 4-momentum associated with the virtual boson.

In the non-relativistic limit, $q^2 = q_0^2 - |\boldsymbol{q}|^2 \approx -|\boldsymbol{q}|^2$, and the spinor products in (4.30) simplify to:

$$\bar{u}(\boldsymbol{p}_{1,f})\gamma_5 u(\boldsymbol{p}_{1,i}) \approx -\boldsymbol{\sigma}_1\cdot\boldsymbol{q}\,, \tag{4.31}$$

$$\bar{u}(\boldsymbol{p}_{2,f})u(\boldsymbol{p}_{2,i}) \approx 2m_2\,, \tag{4.32}$$

where $\boldsymbol{p}_1 = (\boldsymbol{p}_{1,i} + \boldsymbol{p}_{1,f})/2$ and $\boldsymbol{p}_2 = (\boldsymbol{p}_{2,i} + \boldsymbol{p}_{2,f})/2$ are the momenta of the two fermions, averaged over their respective initial and final states.

The resulting non-relativistic momentum-space potential reads:

$$\tilde{V}(q) \approx \frac{\mathcal{M}(q)}{4m_1 m_2} \approx \frac{ig_1^p g_2^s}{2m_1} \frac{\boldsymbol{\sigma}_1 \cdot \boldsymbol{q}}{M^2 + |\boldsymbol{q}|^2} \,. \tag{4.33}$$

The non-relativistic coordinate-space potential is related to the momentum-space potential via the three-dimensional Fourier transform:

$$V(\boldsymbol{r}) = \int \frac{d^3q}{(2\pi)^3} e^{i\boldsymbol{q}\cdot\boldsymbol{r}} \tilde{V}(\boldsymbol{q}) \,. \tag{4.34}$$

Using the Fourier transform (4.22), we arrive at the coordinate-space potential in Eq. (4.5).

We note that, apart from the non-derivative form of the pseudoscalar interaction in (4.1), the derivative form of the pseudoscalar interaction is also commonly used in the literature (see, e.g., [63–65]):

$$\mathcal{L}_{\text{deriv.}} = -(\partial_\mu \phi) \sum_\psi \frac{g_\psi^p}{2m_\psi} \bar{\psi} \gamma^\mu \gamma_5 \psi \,. \tag{4.35}$$

The form of the non-relativistic potential in Eq. (4.5) does not depend on whether the non-derivative or derivative form of the pseudoscalar interaction is used. To see this explicitly, we note that, instead of the spinor product in (4.31), we have the following spinor product for the derivative form of the pseudoscalar interaction:

$$\frac{q_\mu}{2m_1} \bar{u}(\boldsymbol{p}_{1,f}) \gamma^\mu \gamma_5 u(\boldsymbol{p}_{1,i}) \approx \frac{\boldsymbol{\sigma}_1 \cdot \boldsymbol{p}_1}{m_1} q_0 - \boldsymbol{\sigma}_1 \cdot \boldsymbol{q} \,. \tag{4.36}$$

In the non-relativistic limit, $|q_0| \ll |\boldsymbol{q}|$ and $|\boldsymbol{p}_1|/m_1 \ll 1$, and so the spinor product in (4.36) reduces to (4.31). Likewise, the form of the non-relativistic potential in Eq. (5.3) also does not depend on whether the non-derivative or derivative form of the pseudoscalar interaction is used.

2 – Vector-vector potential

Applying the Feynman rules to the tree-level process in Fig. 4.1 with both vertices being of the vector type in Lagrangian (4.2), gives the amplitude:

$$\begin{aligned} \mathcal{M}(q) =& i \left[i\bar{u}(\boldsymbol{p}_{1,f}) \gamma^\mu g_1^V u(\boldsymbol{p}_{1,i}) \right] \left[i\bar{u}(\boldsymbol{p}_{2,f}) \gamma^\nu g_2^V u(\boldsymbol{p}_{2,i}) \right] \\ & \times \left[\frac{i\left(g_{\mu\nu} - q_\mu q_\nu / M^2\right)}{M^2 - q^2} \right] . \end{aligned} \tag{4.37}$$

In the non-relativistic limit, $q^2 \approx -|\boldsymbol{q}|^2$, and the spinor products in (4.37) simplify to:

$$\bar{u}(\boldsymbol{p}_{1,f}) \gamma^0 u(\boldsymbol{p}_{1,i}) \approx 2m_1 \,, \tag{4.38}$$

$$\bar{u}(\boldsymbol{p}_{2,f}) \gamma^0 u(\boldsymbol{p}_{2,i}) \approx 2m_2 \,, \tag{4.39}$$

$$\bar{u}(\boldsymbol{p}_{1,f}) \boldsymbol{\gamma} u(\boldsymbol{p}_{1,i}) \approx 2\boldsymbol{p}_1 - i\boldsymbol{q} \times \boldsymbol{\sigma}_1 \,, \tag{4.40}$$

$$\bar{u}(\boldsymbol{p}_{2,f})\gamma u(\boldsymbol{p}_{2,i}) \approx 2\boldsymbol{p}_2 + i\boldsymbol{q}\times\boldsymbol{\sigma}_2\,. \tag{4.41}$$

The $q_\mu q_\nu/M^2$ term in the propagator does not contribute to the amplitude, because of the conservation of the vector current in both vertices. Retaining the leading-order spin-independent term and the leading-order spin-dependent term, yields the non-relativistic momentum-space potential:

$$\tilde{V}(q) \approx \frac{g_1^V g_2^V}{M^2+|\boldsymbol{q}|^2}\left[1 - \frac{(\boldsymbol{q}\times\boldsymbol{\sigma}_1)\cdot(\boldsymbol{q}\times\boldsymbol{\sigma}_2)}{4m_1m_2}\right]. \tag{4.42}$$

Performing the Fourier transform, Eq. (4.34), with the aid of the identity (4.20) and the Fourier transforms (4.21), (4.23) and (4.24), we arrive at the coordinate-space potential in Eq. (4.7).

3 – Pseudovector-vector potential

Applying the Feynman rules to the tree-level process in Fig. 4.1 with vertex 1 being of the pseudovector type and vertex 2 being of the vector type in Lagrangian (4.2), gives the amplitude:

$$\begin{aligned}\mathcal{M}(q) =& i\left[i\bar{u}(\boldsymbol{p}_{1,f})\gamma^\mu\gamma_5 g_1^A u(\boldsymbol{p}_{1,i})\right]\left[i\bar{u}(\boldsymbol{p}_{2,f})\gamma^\nu g_2^V u(\boldsymbol{p}_{2,i})\right]\\ &\times\left[\frac{i\left(g_{\mu\nu}-q_\mu q_\nu/M^2\right)}{M^2-q^2}\right].\end{aligned} \tag{4.43}$$

In the non-relativistic limit, $q^2 \approx -|\boldsymbol{q}|^2$, and the spinor products in (4.43) simplify to:

$$\bar{u}(\boldsymbol{p}_{1,f})\gamma^0\gamma_5 u(\boldsymbol{p}_{1,i}) \approx 2\boldsymbol{\sigma}_1\cdot\boldsymbol{p}_1\,, \tag{4.44}$$

$$\bar{u}(\boldsymbol{p}_{2,f})\gamma^0 u(\boldsymbol{p}_{2,i}) \approx 2m_2\,, \tag{4.45}$$

$$\bar{u}(\boldsymbol{p}_{1,f})\boldsymbol{\gamma}\gamma_5 u(\boldsymbol{p}_{1,i}) \approx 2m_1\boldsymbol{\sigma}_1\,, \tag{4.46}$$

$$\bar{u}(\boldsymbol{p}_{2,f})\boldsymbol{\gamma} u(\boldsymbol{p}_{2,i}) \approx 2\boldsymbol{p}_2 + i\boldsymbol{q}\times\boldsymbol{\sigma}_2\,. \tag{4.47}$$

Again, the $q_\mu q_\nu/M^2$ term in the propagator does not contribute to the amplitude, because of the conservation of the vector current in the second vertex. We hence find the following non-relativistic momentum-space potential:

$$\tilde{V}(q) \approx \frac{g_1^A g_2^V}{M^2+|\boldsymbol{q}|^2}\left[\boldsymbol{\sigma}_1\cdot\left(\frac{\boldsymbol{p}_1}{m_1}-\frac{\boldsymbol{p}_2}{m_2}\right) + i\frac{(\boldsymbol{\sigma}_1\times\boldsymbol{\sigma}_2)\cdot\boldsymbol{q}}{2m_2}\right]. \tag{4.48}$$

Performing the Fourier transform, Eq. (4.34), with the aid of the Fourier transforms (4.21) and (4.22), and then performing the symmetrisation $(\boldsymbol{p}_1/m_1 - \boldsymbol{p}_2/m_2)\left(e^{-Mr}/r\right) \to \frac{1}{2}\{\boldsymbol{p}_1/m_1 - \boldsymbol{p}_2/m_2, e^{-Mr}/r\}$, we arrive at the coordinate-space potential in Eq. (4.8).

4.8 Coordinate-space potentials in semi-relativistic form

In a form convenient for numerical atomic calculations using relativistic Dirac-Hartree-Fock wavefunctions, the potentials in Eqs. (4.4) – (5.1), including Dirac spinors, can be written in the following general form:

$$V_{ss}(\boldsymbol{r}) = -\left(\bar{\psi}_2 g_2^s \psi_2\right)\left(\bar{\psi}_1 g_1^s \psi_1\right)\frac{e^{-Mr}}{4\pi r}\,, \tag{4.49}$$

$$V_{ps}(\boldsymbol{r}) = -\left(\bar{\psi}_2 g_2^s \psi_2\right)\left(\bar{\psi}_1 i\gamma_5 g_1^p \psi_1\right)\frac{e^{-Mr}}{4\pi r}\,, \tag{4.50}$$

$$V_{pp}(\boldsymbol{r}) = -\left(\bar{\psi}_2 i\gamma_5 g_2^p \psi_2\right)\left(\bar{\psi}_1 i\gamma_5 g_1^p \psi_1\right)\frac{e^{-Mr}}{4\pi r}\,, \tag{4.51}$$

$$V_{VV}(\boldsymbol{r}) = \left(\bar{\psi}_2 \gamma^\mu g_2^V \psi_2\right)\left(\bar{\psi}_1 \gamma_\mu g_1^V \psi_1\right)\frac{e^{-Mr}}{4\pi r}\,, \tag{4.52}$$

$$V_{AV}(\boldsymbol{r}) = \left(\bar{\psi}_2 \gamma^\mu g_2^V \psi_2\right)\left(\bar{\psi}_1 \gamma_\mu\gamma_5 g_1^A \psi_1\right)\frac{e^{-Mr}}{4\pi r}\,, \tag{4.53}$$

$$V_{AA}(\boldsymbol{r}) = \left(\bar{\psi}_2 \gamma^\mu\gamma_5 g_2^A \psi_2\right)\left(\bar{\psi}_1 \gamma_\mu\gamma_5 g_1^A \psi_1\right)\frac{e^{-Mr}}{4\pi r}\,, \tag{4.54}$$

where we have made use of the static approximation for the boson propagators, and in Eq. (4.54), we have dropped additional terms arising from the longitudinal polarisation mode of the massive spin-1 boson. In practical applications, often one of the fermions can be treated non-relativistically, in which case the potentials in Eqs. (4.49) – (4.54) reduce to a mixed relativistic/non-relativistic form (see, e.g., Refs. [44, 46, 51] for more details).

Bibliography

[1] B. A. Dobrescu and I. Mocioiu, JHEP **2006**, 005 (2006).

[2] R. D. Peccei and H. R. Quinn, Phys. Rev. Lett. **38**, 1440 (1977).

[3] R. D. Peccei and H. R. Quinn, Phys. Rev. D **16**, 1791 (1977).

[4] S. Weinberg, Phys. Rev. Lett. **40**, 223 (1978).

[5] F. Wilczek, Phys. Rev. Lett. **40**, 279 (1978).

[6] J. Kim, Phys. Rev. Lett. **43**, 103 (1979).

[7] M. Shifman, A. Vainshtein, and V. Zakharov, Nucl. Phys. B **166**, 493 (1980).

[8] A. R. Zhitnitsky, Yad. Fiz. **31**, 1024 (1980) [Sov. J. Nucl. Phys. **31**, 529 (1980)].

[9] M. Dine, W. Fischler, and M. Srednicki, Phys. Lett. **104B**, 199 (1981).

[10] G. Bertone, D. Hooper, and J. Silk, Phys. Rep. **405**, 279 (2005).

[11] J. A. Frieman, M. S. Turner, and D. Huterer, Ann. Rev. Astron. Astrophys. **46**, 385 (2008).

[12] W.-T. Ni, S.-S. Pan, H.-C. Yeh, L.-S. Hou, and J. Wan, Phys. Rev. Lett. **82**, 2439 (1999).

[13] B. R. Heckel, C. E. Cramer, T. S. Cook, E. G. Adelberger, S. Schlamminger, and U. Schmidt, Phys. Rev. Lett. **97**, 021603 (2006).

[14] S. Baessler, V. V. Nesvizhevsky, K. V. Protasov, and A. Yu. Voronin, Phys. Rev. D **75**, 075006 (2007).

[15] G. D. Hammond, C. C. Speake, C. Trenkel, and A. P. Paton, Phys. Rev. Lett. **98**, 081101 (2007).

[16] B. R. Heckel, E. G. Adelberger, C. E. Cramer, T. S. Cook, S. Schlamminger, and U. Schmidt, Phys. Rev. D **78**, 092006 (2008).

[17] G. Vasilakis, J. M. Brown, T. W. Kornack, and M. V. Romalis, Phys. Rev. Lett. **103**, 261801 (2009).

[18] A. P. Serebrov, Phys. Lett. B **680**, 423 (2009).

[19] V. K. Ignatovich and Y. N. Pokotilovski, Eur. Phys. J. C **64**, 19 (2009).

[20] A. P. Serebrov *et al.*, JETP Lett. **91**, 6 (2010).

[21] S. G. Karshenboim, Phys. Rev. Lett. **104**, 220406 (2010).

[22] S. G. Karshenboim, Phys. Rev. D **82**, 113013 (2010).

[23] A. K. Petukhov, G. Pignol, D. Jullien, and K. H. Andersen, Phys. Rev. Lett. **105**, 170401 (2010).

[24] S. G. Karshenboim and V. V. Flambaum, Phys. Rev. A **84**, 064502 (2011).

[25] S. A. Hoedl, F. Fleischer, E. G. Adelberger, and B. R. Heckel, Phys. Rev. Lett. **106**, 041801 (2011).

[26] G. Raffelt, Phys. Rev. D **86**, 015001 (2012).

[27] H. Yan, and W. M. Snow, Phys. Rev. Lett. **110**, 082003 (2013).

[28] L. Hunter, J. Gordon, S. Peck, D. Ang, and J.-F. Lin, Science **339**, 928 (2013).

[29] K. Tullney *et al.*, Phys. Rev. Lett. **111**, 100801 (2013).

[30] P.-H. Chu *et al.*, Phys. Rev. D **87**, R011105 (2013).

[31] M. Bulatowicz *et al.*, Phys. Rev. Lett. **111**, 102001 (2013).

[32] S. Mantry, M. Pitschmann, and M. J. Ramsey-Musolf, Phys. Rev. D **90**, 054016 (2014).

[33] L. R. Hunter and D. G. Ang, Phys. Rev. Lett. **112**, 091803 (2014).

[34] E. J. Salumbides, W. Ubachs, V. I. Korobov, J. Mol. Spectrosc. **300**, 65 (2014).

[35] T. M. Leslie, E. Weisman, R. Khatiwada, and J. C. Long, Phys. Rev. D **89**, 114022 (2014).

[36] A. Arvanitaki and A. A. Geraci, Phys. Rev. Lett. **113**, 161801 (2014).

[37] Y. V. Stadnik and V. V. Flambaum, Eur. Phys. J. C **75**, 110 (2015).

[38] S. Afach *et al.*, Phys. Lett. B **745**, 58 (2015).

[39] W. A. Terrano, E. G. Adelberger, J. G. Lee, and B. R. Heckel, Phys. Rev. Lett. **115**, 201801 (2015).

[40] N. Leefer, A. Gerhardus, D. Budker, V. V. Flambaum, and Y. V. Stadnik, Phys. Rev. Lett. **117**, 271601 (2016).

[41] F. Ficek, D. F. Jackson Kimball, M. G. Kozlov, N. Leefer, S. Pustelny, and D. Budker, Phys. Rev. A **95**, 032505 (2017).

[42] W. Ji, C. B. Fu, and H. Gao, Phys. Rev. D **95**, 075014 (2017).

[43] N. Crescini, C. Braggio, G. Carugno, P. Falferi, A. Ortolan, and G. Ruoso, Phys. Lett. B **773**, 677 (2017).

[44] V. A. Dzuba, V. V. Flambaum, and Y. V. Stadnik, Phys. Rev. Lett. **119**, 223201 (2017).

[45] C. Delaunay, C. Frugiuele, E. Fuchs, and Y. Soreq, Phys. Rev. D **96**, 115002 (2017).

[46] Y. V. Stadnik, V. A. Dzuba, and V. V. Flambaum, Phys. Rev. Lett. **120**, 013202 (2018).

[47] X. Rong *et al.*, Nature Comm. **9**, 739 (2018).

[48] M. S. Safronova, D. Budker, D. DeMille, D. F. Jackson Kimball, A. Derevianko, and C. W. Clark, Rev. Mod. Phys. **90**, 025008 (2018).

[49] F. Ficek, P. Fadeev, V. V. Flambaum, D. F. Jackson Kimball, M. G. Kozlov, Y. V. Stadnik, and D. Budker, Phys. Rev. Lett. **120**, 183002 (2018).

[50] X. Rong *et al.*, Phys. Rev. Lett. **121**, 080402 (2018).

[51] V. A. Dzuba, V. V. Flambaum, I. B. Samsonov, and Y. V. Stadnik, Phys. Rev. D **98**, 035048 (2018).

[52] Y. J. Kim, P. H. Chu, and I. Savukov, Phys. Rev. Lett. **121**, 091802 (2018).

[53] J. E. Moody and F. Wilczek, Phys. Rev. D **30**, 130 (1984).

[54] C. Bouchiat, Phys. Lett. **57B**, 284 (1975).

[55] A. A. Ansel'm, Pis'ma Zh. Eksp. Teor. Fiz. **36**, 46 (1982) [JETP Lett. **36**, 55 (1982)].

[56] L. D. Landau and E. M. Lifshitz, *Quantum Mechanics (Nonrelativistic Theory)*, 3rd ed. (Butterworth-Heinemann, Oxford, 1977).

[57] B. A. Dobrescu, Phys. Rev. Lett. **94**, 151802 (2005).

[58] J. J. Sakurai, *Advanced Quantum Mechanics*, (Addison-Wesley, Reading, 1967).

[59] F. Gross, *Relativistic Quantum Mechanics and Field Theory*, (Wiley-VCH, Weinheim, 1999).

[60] R. Daido and F. Takahashi, Phys. Lett. B **772**, 127 (2017).

[61] P. C. Malta, L. P. R. Ospedal, K. Veiga, and J. A. Helayël-Neto, Adv. High Energy Phys. **2016**, 2531436 (2016).

[62] K. Gordon, *Modern Elementary Particle Physics*, (Cambridge University Press, UK, 2017).

[63] M. Pospelov, A. Ritz, and M. B. Voloshin, Phys. Rev. D **78**, 115012 (2008).

[64] Y. V. Stadnik and V. V. Flambaum, Phys. Rev. D **89**, 043522 (2014).

[65] C. Abel *et al.*, Phys. Rev. X **7**, 041034 (2017).

Chapter 5

Pseudovector and pseudoscalar spin-dependent interactions in atoms

Phys. Rev. A **105**, 022812 (2022)

Pavel Fadeev[1], Filip Ficek[2], Mikhail G. Kozlov[3,4], Dmitry Budker[1,5], and Victor V. Flambaum[1,6]

[1] *Helmholtz Institute Mainz, Johannes Gutenberg University, 55128 Mainz, Germany*
[2] *Institute of Physics, Jagiellonian University, Łojasiewicza 11, 30-348 Kraków, Poland*
[3] *Petersburg Nuclear Physics Institute of NRC "Kurchatov Institute", Gatchina 188300, Russia*
[4] *St.Petersburg Electrotechnical University LETI,Prof. Popov Str. 5, 197376 St.Petersburg, Russia*
[5] *Department of Physics, University of California at Berkeley, Berkeley, California 94720-7300, USA*
[6] *School of Physics, University of New South Wales, Sydney, New South Wales 2052, Australia*

Hitherto unknown elementary particles can be searched for with atomic spectroscopy. We conduct such a search using a potential that results from the longitudinal polarization of a pseudovector particle. We show that such a potential, inversely proportional to the boson's mass squared, $V \propto 1/M^2$, can stay finite at $M \to 0$ if the theory is renormalizable. We also look for a pseudoscalar boson, which induces a contact spin-dependent potential that does not contribute to new forces searched for in experiments with macroscopic objects, but may be seen in atomic spectroscopy. We extract limits on the interaction constants of these potentials from the experimental spectra of antiprotonic helium, muonium, positronium, helium, and hydrogen.

5.1 Introduction

A possible explanation for various outstanding puzzles in physics, such as the origins of dark matter [1] and dark-energy [2, 3], the strong-CP puzzle [4], and the hierarchy puzzle [5] is the existence of beyond-the-standard-model (exotic) bosons. The exchange of such virtual

bosons gives rise to an interaction potential. This motivates experimental searches for such potentials in nuclear, atomic, and molecular phenomena [6–8].

Recent work [9] derived a list of these potentials, sorted by types of interactions (as opposed to [10], which classified the potentials by their spin-momentum structure). These are nonrelativistic potentials in coordinate space, induced by the exchange of spin-zero or spin-one exotic bosons between fermions. Reference [9] lists two types of potentials that were omitted in [10]:

(a) A potential proportional to the inverse square of the intermediate spin-one boson mass, originating from its longitudinal polarization.

(b) Potentials that include the contact term $\delta(r)$, with r being the distance between the interacting fermions.

Point (a) is important for the study of exotic bosons with pseudovector-pseudovector interactions. Point (b) is of concern when an experimental search for new bosons is conducted in atomic systems, where a contact interaction can play a vital role. Next, we discuss each of these potentials and the methodology of using them to obtain constraints on the properties of new bosons. Then, in section III we use these potentials to obtain novel limits on boson mass and coupling strength in various atomic systems. We conclude in Section IV.

5.2 Properties of pseudovector and pseudoscalar potentials

5.2.1 Potential proportional to $1/M^2$

Among the nine potentials derived in [9] which describe the exchange of an exotic boson between two fermions or macroscopic objects, the pseudovector-pseudovector potential is the only velocity-independent one with a term inversely proportional to the boson mass squared:

$$V_{AA}(\boldsymbol{r}) = -\,g_1^A g_2^A \underbrace{\boldsymbol{\sigma}_1\cdot\boldsymbol{\sigma}_2\frac{e^{-Mr}}{4\pi r}}_{\mathcal{V}_2} - \frac{g_1^A g_2^A m_1 m_2}{M^2}\underbrace{\left[\boldsymbol{\sigma}_1\cdot\boldsymbol{\sigma}_2\left[\frac{1}{r^3}+\frac{M}{r^2}+\frac{4\pi}{3}\delta(\boldsymbol{r})\right]-(\boldsymbol{\sigma}_1\cdot\hat{\boldsymbol{r}})\,(\boldsymbol{\sigma}_2\cdot\hat{\boldsymbol{r}})\left[\frac{3}{r^3}+\frac{3M}{r^2}+\frac{M^2}{r}\right]\right]\frac{e^{-Mr}}{4\pi m_1 m_2}}_{\mathcal{V}_3} \tag{5.1}$$

Here, g^A are dimensionless interaction constants that parametrize the pseudovector interaction strength, $\boldsymbol{\sigma}_1$ and $\boldsymbol{\sigma}_2$ denote the Pauli spin-matrix vectors of the two fermions, m_1 and m_2 are the masses of the fermions, M is the mass of the boson, $\hat{\boldsymbol{r}}$ is the unit vector directed from fermion 2 to fermion 1, and r is the distance between the two fermions. We work in natural relativistic units, $\hbar = c = 1$. Parts of the potentials defined as $\mathcal{V}_2$ and $\mathcal{V}_3$ link these terms to the definitions of the potentials described in [10]. While deriving $V_{AA}(\mathbf{r})$ we have

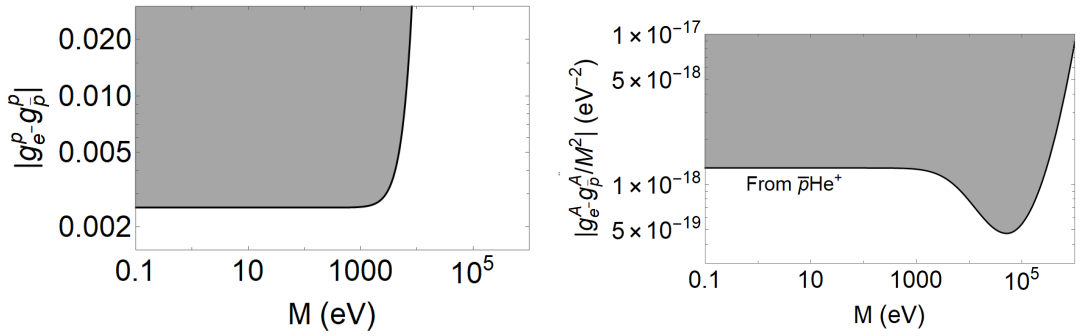

(a) (b)

Figure 5.1: *Constraints for the interaction between an electron and an antiproton at 90% confidence level on the coupling constants as a function of boson mass. We are using states in the* $(n, l) = (37, 35)$ *manifold of antiprotonic helium* $\bar{p}He^+$*. The plots are based on the experimental data from [26], theoretical calculations from [27], and our numerical estimate of the spin-dependent contribution. (a) Using the* V_{pp} *potential of Eq. (5.6) in numerical integration. For* $M < 10^2$ *eV the limit is at* 0.0025*. (b) Using* V_{AA} *in Eq.* (5.1)*. In the range* $M < 10^2$ *eV the bound is* $g_e^A g_{\bar{p}}^A/M^2 \leq 1.3 \times 10^{-18}$ *eV*$^{-2}$*. In the vicinity of* $M = 5 \times 10^4$ *eV the bound is at* 4.7×10^{-19} *eV*$^{-2}$*. This and other bounds are summarized in Table 5.1.*

retained the leading order spin-dependent terms; that is why operators such as $\mathcal{V}_8$ in [10] do not show up in Eq. (5.1).

To find the interaction for composite systems, one should sum the interaction (5.1) over all fermion constituents (electrons, protons, and neutrons), each with its own interaction constants. The result will be proportional to the nuclear or atomic spins, similar to the usual magnetic interaction between atoms in a crystal. Examples of composite systems used in experimental searches for spin-dependent potentials can be found in Refs. [6, 11–14].

The $\mathcal{V}_3$ term in Eq. (5.1) arises from a longitudinal polarization mode for a massive spin-1 boson (which gives the term $q_\nu q_\mu/M^2$ in the massive vector boson propagator, q_ν being the four-momentum transferred between the fermions) and nonconservation of the axial-vector current ($q_\nu J_\nu^a \neq 0$) [9, 15, 16]. This term appears to have a singularity in the limit of the boson mass $M \to 0$. However, there should be no divergence in a renormalizable theory. Let us reflect on the following scenario based on the standard-model Lagrangian. We will see that as $M \to 0$, the combination of parameters $g_1^A g_2^A/M^2$ remains finite. Consider Z-boson exchange between two fermions, where, in this case, the Z boson has purely pseudovector interactions and does not mix with the photon [$\sin(\theta_W) = 0$, where θ_W is the weak mixing angle]. Then, the Z-boson mass is given by $M = gv/2$, where v is the Higgs vacuum expectation value and g is the (universal) electroweak interaction constant [17]. The ratio $g^2/M^2 = 4/v^2$ remains finite as $M \to 0$, since the right-hand side is a constant. For v to be nonzero the fermion mass $m_f = fv/\sqrt{2}$ (f is a species-dependent interaction constant) should be nonzero. Thus, it is appropriate to place constraints on $g_1^A g_2^A/M^2$ of the $\mathcal{V}_3$ term in Eq. (5.1). The association with renormalizability (with the Higgs mechanisms of mass generation) makes this case worthy of experimental study.

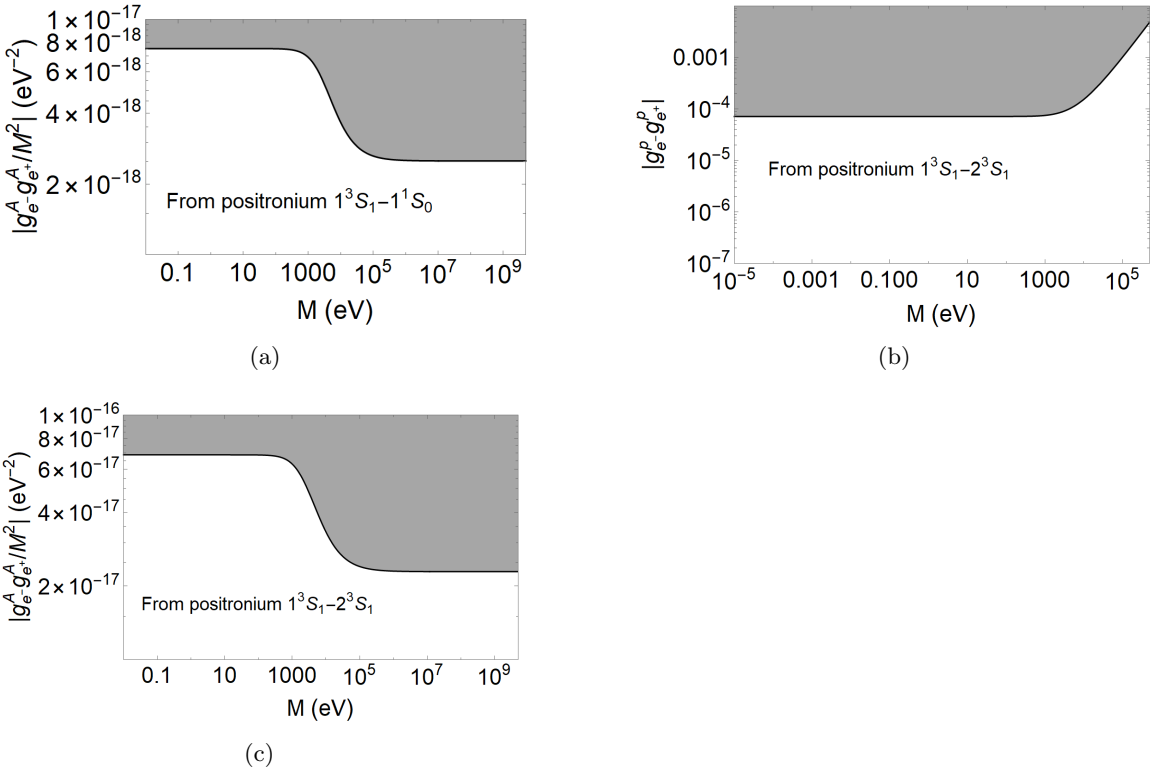

Figure 5.2: *Constraints for the electron-positron interaction at 90% confidence level on the coupling constants as a function of boson mass. (a) The plot is based on experimental [34–36] and theoretical [37] values for the $1^3S_1 - 1^1S_0$ ground state transition in positronium [33] and our numerical estimate of the spin-dependent contribution. (b) The plot is based on experimental [38] and theoretical [39, 40] values for the $1^3S_1 - 2^3S_1$ transition in positronium [32] and our numerical estimates of the spin-dependent contribution. The bound is based on V_{pp} potential of Eq. (5.6). (c) Using V_{AA} in Eq. (5.1). Same transition as in (b).*

In the special case of a massless vector boson, $M = 0$, only the $\mathcal{V}_2$ term remains in Eq. (5.1) because a massless vector boson does not have a longitudinal polarization mode, and so the $\mathcal{V}_3$ term does not appear in this case.

5.2.2 Bounds on contact terms

Searches for exotic spin-dependent forces have been conducted both in atomic-scale experiments and in macroscopic-scale experiments [11, 14, 18–22]. To search for new bosons, one may look for the difference between observations and theoretical predictions in the spectrum of an atomic, molecular, or nuclear system [23–25]. Such difference can be due to an exotic-boson exchange between the system's constituents.

Unlike in macroscopic searches for new bosons, a contact term in a potential is of significance in atomic systems. Let us focus on determining a bound on the properties of spin-zero or spin-one exotic bosons by using a potential that includes the contact term $\delta(\boldsymbol{r})$, such as the one appearing in Eq. (5.1) and other potentials in [9]. Contact terms were omitted in Ref. [10], but appeared in Refs. [4, 15].

As in [23], we compare experimental results for the hyperfine structure of the antiprotonic helium [26] with theoretical QED-based calculations for this system [27]. The difference between experiment and theory ΔE at 90% confidence level determined from

$$\int_{-\Delta E}^{+\Delta E} \frac{1}{\sqrt{2\pi}\sigma} e^{-(x-\mu)^2/(2\sigma^2)dx} = 0.9\,, \tag{5.2}$$

where μ is the mean difference between theoretical and experimental transition energies and σ is the total uncertainty, $\sigma^2 = \sigma_{th}^2 + \sigma_{exp}^2$. To avoid misunderstanding, note that here theory uncertainty means uncertainty in the results of the calculations of the transition frequencies within the standard model.

We focus on a transition with the antiproton in the (n, l) = (37, 35) state and the electron in the (1, 0) state (where the first number is the principal quantum number, and the second one is the orbital angular momentum). Let us consider the pseudoscalar-pseudoscalar potential, which appears in [23] and contains a contact term:

$$V_{pp}(\boldsymbol{r}) = -\frac{g_1^p g_2^p}{4} \underbrace{\left[\boldsymbol{\sigma}_1\cdot\boldsymbol{\sigma}_2\left[\frac{1}{r^3}+\frac{M}{r^2}+\frac{4\pi}{3}\delta(\boldsymbol{r})\right]-(\boldsymbol{\sigma}_1\cdot\hat{\boldsymbol{r}})\,(\boldsymbol{\sigma}_2\cdot\hat{\boldsymbol{r}})\left[\frac{3}{r^3}+\frac{3M}{r^2}+\frac{M^2}{r}\right]\right]\frac{e^{-Mr}}{4\pi m_1 m_2}}_{\mathcal{V}_3}\,. \tag{5.3}$$

We deduce the contribution of this potential to the transition energies of the antiproton in antiprotonic helium. The difference between the expectation values of V_{pp} in the two states gives an estimate of the energy shift between the states caused by V_{pp}. The contact term contribution is of the form $g_1^p g_2^p C$ where C is a constant. Other terms in the expectation value of V_{pp} vary with boson mass. We denote such terms by $g_1^p g_2^p \Delta U(M)$. Assuming the

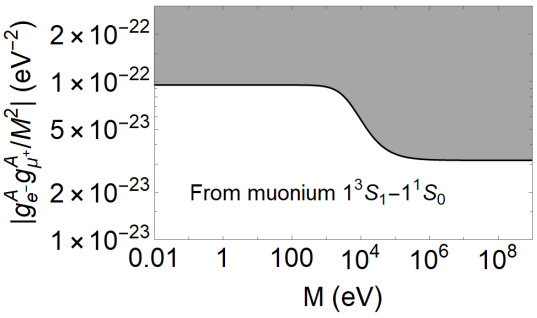

Figure 5.3: *Constraints for the interaction between an antimuon and an electron, at 90% confidence level on the coupling constants as a function of boson mass, using V_{AA} in Eq. (5.1). The plot is based on experimental [41] and theoretical [42, 43] values for the hyperfine ground state transition in muonium [32] and our numerical estimate of the spin-dependent contribution.*

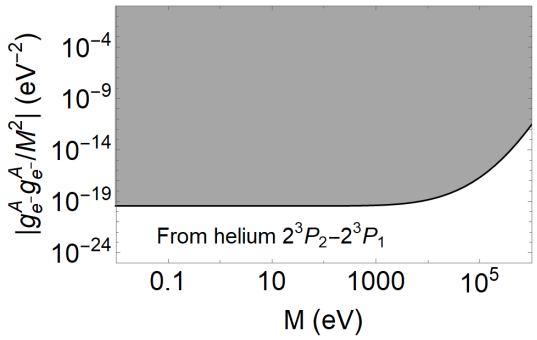

Figure 5.4: *Constraints for the interaction between electrons, at 90% confidence level on the coupling constants as a function of boson mass, using V_{AA} in Eq. (5.1). The plot is based on experimental [44] and theoretical [45] values for the $2^3P_2 - 2^3P_1$ transition in helium [24] and our numerical estimate of the spin-dependent contribution.*

difference between theory and experiment ΔE at 90% confidence level [Eq. (5.2)] is due to V_{pp}, we may write

$$|\, g_1^p g_2^p \,(C + \Delta U(M))\,| \leq |\, \Delta E\,|\,, \tag{5.4}$$

which results in

$$|\, g_1^p g_2^p\,| \leq \left|\frac{\Delta E}{(C + \Delta U(M))}\right|. \tag{5.5}$$

The left-hand side in this expression is the ordinate in Fig. 5.1(a). In the regime $C \gg \Delta U(M)$ the right-hand side would be a constant independent of M. However, in the limit of large M we obtain $\Delta U(M) \to -C$ and nearly cancel it. This may lead to a numerical instability at large M, discussed in Appendix 5.5.

The solution we propose is to use a different form of the potential in numerical calculations, a form which appeared during the derivation of the potentials and contains the operator ∇.

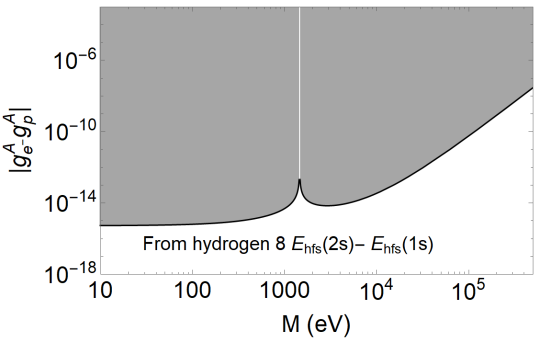

Figure 5.5: *Constraints for the electron-proton interaction, at 90% confidence level on the coupling constants as a function of boson mass, using V_{AA} in Eq. (5.1). The plot is based on experimental [43, 46–55] and theoretical [56] values for the $8E_{\rm hfs}(2s) - E_{\rm hfs}(1s)$ difference between hyperfine transitions in hydrogen [57] and our numerical estimate of their spin-dependent contributions. Such a difference cancels the contribution of the contact terms, since the electron density on the proton in the $2s$ state is eight times smaller than in the $1s$ state. The vertical asymptote at 1450 eV is due to a cancellation in the denominator of Eq. (5.8) for this plot.*

Such a form for Eq. (5.3) is

$$V_{pp}(\boldsymbol{r}) = \frac{g_1^p g_2^p}{16\pi m_1 m_2} (\boldsymbol{\sigma}_1 \cdot \boldsymbol{\nabla}) (\boldsymbol{\sigma}_2 \cdot \boldsymbol{\nabla}) \left(\frac{e^{-Mr}}{r} \right) . \tag{5.6}$$

Then, calculating expectation values with Eq. (5.6), we use integration by parts to avoid possible numerical issues of the contact term. From integration by parts of Eq. (5.6) we see that there is no physical problem, only a numerical one.

In Eq. (5.3) the correct large-M asymptotic is achieved due to delicate cancellation of different terms. This is hard to achieve in a numerical calculation. However, in Eq. (5.6) there is only one term, so no cancellation is required and the correct asymptotic is immediately seen ($e^{-Mr}/r \to \delta(\boldsymbol{r})\, 4\pi/M^2$). Using Eq. (5.6) instead of Eq. (5.3) and integrating by parts, we arrive at Fig. 5.1(a) — a bound on the $| g_{e^-}^p g_{\bar{p}}^p |$ coupling constants as a function of boson mass. Note that in [23] the bound was placed on the coefficient f_3, which relates to the pseudoscalar coupling constants in the following way [10]: $f_3 = -\frac{g_{e^-}^p g_{\bar{p}}^p m_e}{4 m_{\bar{p}}}$, where m_e is the mass of the electron and $m_{\bar{p}}$ is the mass of the antiproton.

We sort the potentials according to the type of mediating particle (scalar, vector, etc.) and place limits on their coupling constants [9]. In this form the limits may be compared with the astrophysical, dark matter search and particle accelerator limits.

Transition	Bound	In the range	In Figure
Antiprotonic helium	$g_e^p g_{\bar{p}}^p \leq 0.0025$	$M < 10^2$ eV	5.1(a)
$(35.5, 35, 34) - (34.5, 34, 34)$	$g_e^A g_{\bar{p}}^A \leq 1.3 \times 10^{-18} (M/\mathrm{eV})^2$	$M < 10^2$ eV	5.1(b)
Positronium	$g_{e^-}^p g_{e^+}^p \leq 7.9 \times 10^{-6}$	$M < 10^2$ eV	5.7
$1^3S_1 - 1^1S_0$	$g_{e^-}^p g_{e^+}^p \leq 1.0 \times 10^{-9} M/\,\mathrm{eV}$	$M > 10^5$ eV	5.7
	$g_{e^-}^A g_{e^+}^A \leq 7.5 \times 10^{-18} (M/\mathrm{eV})^2$	$M < 10^2$ eV	5.2(a)
	$g_{e^-}^A g_{e^+}^A \leq 2.5 \times 10^{-18} (M/\mathrm{eV})^2$	$M > 10^5$ eV	5.2(a)
Positronium	$g_{e^-}^p g_{e^+}^p \leq 7.2 \times 10^{-5}$	$M < 10^2$ eV	5.2(b)
$1^3S_1 - 2^3S_1$	$g_{e^-}^p g_{e^+}^p \leq 9.6 \times 10^{-9} M/\mathrm{eV}$	$M > 10^5$ eV	5.2(b)
	$g_{e^-}^A g_{e^+}^A \leq 6.9 \times 10^{-17} (M/\mathrm{eV})^2$	$M < 10^2$ eV	5.2(c)
	$g_{e^-}^A g_{e^+}^A \leq 2.3 \times 10^{-17} (M/\mathrm{eV})^2$	$M > 10^5$ eV	5.2(c)
Muonium	$g_{e^-}^p g_{\mu^+}^p \leq 2.1 \times 10^{-8}$	$M < 10^2$ eV	5.8
$1^3S_1 - 1^1S_0$	$g_{e^-}^p g_{\mu^+}^p \leq 1.4 \times 10^{-12} M/\mathrm{eV}$	$M > 10^5$ eV	5.8
	$g_{e^-}^A g_{\mu^+}^A \leq 9.5 \times 10^{-23} (M/\mathrm{eV})^2$	$M < 10^2$ eV	5.3
	$g_{e^-}^A g_{\mu^+}^A \leq 3.2 \times 10^{-23} (M/\mathrm{eV})^2$	$M > 10^5$ eV	5.3
Helium	$g_{e^-}^p g_{e^-}^p \leq 4.4 \times 10^{-8}$	$M < 10^2$ eV	5.9
$2^3P_2 - 2^3P_1$	$g_{e^-}^A g_{e^-}^A \leq 3.5 \times 10^{-20} (M/\mathrm{eV})^2$	$M < 10^2$ eV	5.4
Hydrogen	$g_{e^-}^p g_p^p \leq 2.1 (M/\mathrm{eV})^{-2}$	$M < 10^2$ eV	5.10
$8E_{\mathrm{hfs}}(2s) - E_{\mathrm{hfs}}(1s)$	$g_{e^-}^p g_p^p \leq 1.8 \times 10^{-15} (M/\mathrm{eV})^2$	$M > 10^5$ eV	5.10
	$g_{e^-}^A g_p^A \leq 5.3 \times 10^{-16}$	$M < 10^2$ eV	5.5
	$g_{e^-}^A g_p^A \leq 4.5 \times 10^{-31} (M/\mathrm{eV})^4$	$M > 10^5$ eV	5.5

Table 5.1: *Summary of the bounds obtained on properties of hypothetical bosons using various atomic systems.*

5.3 Results

5.3.1 New bound using $1/M^2$ term

We use the properties discussed above to obtain a bound based on Eq. (5.1) for electron–antiproton interaction in antiprotonic helium. In order to avoid numerical issues as $M \to \infty$, the form of Eq. (5.6) can be used in calculating expectation values for the exclusion plot. Thus we construct Fig. 5.1(b). To our knowledge, this is the first bound produced by the term proportional to $1/M^2$ in V_{AA}. Bounds on V_{AA} of this type may be obtained using the results in [24, 28–32], or using any other scheme that is able to constrain $\mathcal{V}_3$. Note further that the bound in Fig. 5.1(b) is for a semileptonic spin-dependent interaction between matter (electron) and antimatter (antiproton).

The bound in Fig. 5.1(b), as well as bounds on figures below which use V_{AA} are derived

in the following way. The equivalent of Eq. (5.4) for V_{AA} is

$$\left| g_1^A g_2^A \left(\Delta U_2(M) + \frac{1}{M^2} \Delta \tilde{U}_3(M) \right) \right| \leq \Delta E \,, \tag{5.7}$$

where $\Delta U_3(M) = \Delta \tilde{U}_3(M)/M^2$; $\Delta U_2(M)$ and $\Delta U_3(M)$ are related to $\mathcal{V}_2$ and $\mathcal{V}_3$ per Eq. (5.1). The bound in Fig. 5.1(b) is from

$$\left| \frac{g_1^A g_2^A}{M^2} \right| \leq \left| \frac{\Delta E}{\left(M^2 \Delta U_2(M) + \Delta \tilde{U}_3(M) \right)} \right| . \tag{5.8}$$

The term $\Delta \tilde{U}_3(M)$ dictates the shape of the plot for small mass M, while $M^2 \Delta U_2(M)$ dictates the shape for large mass M. The ordinates differ between Fig. 5.1(a) and 5.1(b) since Eqs. (5.5) and (5.8) are used, respectively. The scale of each figure is chosen to highlight the shape of each bound.

5.3.2 Positronium, muonium, helium, and hydrogen

We obtain a bound on the potential in Eq. (5.1) using the ground-state $1^3S_1 - 1^1S_0$ transition in positronium. As in [33], we take $|\Delta E| \leq 5$ MHz [11]. The result appears in Fig. 5.2(a) and its bound is described in Table 5.1. The shape of the bound line is explained by the fact that $\mathcal{V}_3$ dominates for small masses M, while $\mathcal{V}_2$ dominates for large masses M where $M^2 \Delta U_2(M)$ results in a constant (see Appendix 5.6).

We can get a bound on $g_{e^-}^A g_{e^+}^A$ from Eq. (5.7), instead of a bound on $g_{e^-}^A g_{e^+}^A / M^2$. Then we can compare the bound with the result in [33] and see that we have a more stringent bound in the regime of $M \ll \Delta \tilde{U}_3 / \Delta U_2$. This is due to the fact that, in contrast to Ref. [33], we use a potential containing the $1/M^2$ term.

In Figs. 5.2(b) and 5.2(c) we present bounds on pseudoscalar and pseudovector electron-positron interaction based on the $1^3S_1 - 2^3S_1$ transition in positronium. We take $\Delta E = 10\,\text{MHz}$ for this transition [32]. In Appendix 5.6 we give general analytical results for the potentials' expectation values in 1s and 2s states.

The ground-state hyperfine transition is measured accurately also in the atomic system of muonium. Using this transition, we obtain a bound on the potential in Eq. (5.1). As in [32], we take $|\Delta E| \leq 5 \times 10^{-4}$ MHz. The result appears in Fig. 5.3.

In Fig. 5.4 we obtain a bound on pseudovector coupling constants and boson mass from the $2^3P_2 - 2^3P_1$ transition of helium, using the results in [24], where $|\Delta E| \leq 3.7$ kHz.

Finally, in Fig. 5.5 we use spectroscopic transitions in hydrogen to obtain a bound on electron-proton pseudovector interaction. Following [57] we take the difference (at 90% confidence level) between theoretical and experimental results $|\Delta E| \leq 0.102$ kHz for $8E_{\text{hfs}}(2s) - E_{\text{hfs}}(1s)$, where E_{hfs} stands for the energy of the hyperfine transition in a particular state.

5.4 Conclusion

One can search for new elementary particles using atomic spectroscopy. For the first time, we conduct such a search using a potential that results from the longitudinal polarization of a pseudovector particle. We also consider the pseudoscalar potential that includes a contact spin-dependent term, which does not contribute to new forces searched for in experiments with macroscopic objects, but does contribute in atomic spectroscopy. We extract limits on the interaction constants of pseudovector and pseudoscalar particles from the experimental spectra of antiprotonic helium, muonium, positronium, helium, and hydrogen. The results are summarized in Table 5.1.

Acknowledgments

We thank Derek Jackson Kimball, Claudia Frugiuele, Yevgeny V. Stadnik, Szymon Pustelny, Anne Fabricant, and Eric Adelberger for their valuable remarks. The authors acknowledge the support by the DFG Reinhart Koselleck project, the European Research Council Dark-OsT advanced grant under project ID 695405, and the Simons and the Heising-Simons Foundations. F. F. is supported by the Polish National Science Centre Grant No. 2020/36/T/ST2/00323. V. V. F. is supported by the Australian Research Council Grants No. DP190100974 and DP200100150 and the JGU Gutenberg Research Fellowship. M. G. K. is supported by RSF grant 19-12-00157 and is grateful to JGU for hospitality.

5.5 Exclusion Plot with Contact Term

Direct application of Eq. (3) in the main text leads to Fig. 5.6, where apparently we obtained a bound on the coupling constants for any boson mass M, as the bound edge is horizontal on the right side of the plot. Nonetheless, this bound plot is incorrect for boson masses much larger than the fermion masses, due to numerical reasons. The problem is that the calculation for large masses M is affected by absence of the proper cancellation between different terms in Eq. (3) of the main text. Therefore in Fig. 5.6 we colored in white the bound where the result is inaccurate.

By focusing on $M < m_1, m_2$ (where m_1 and m_2 are fermion masses) we avoided the issue of finite numerical precision at large boson masses in the exclusion plot of Fig. 3 (b) in [23]. This ensured that the plot in [23], which includes the contribution of the contact term, is correct in the range considered.

5.6 Analytical Derivation of Expectation Values

Consider the potentials without their coupling constants coefficients

$$V_2 = (\sigma_1 \cdot \sigma_2)\frac{e^{-Mr}}{r}, \qquad V_3 = \left[\sigma_1 \cdot \sigma_2 \left(\frac{M}{r^2} + \frac{1}{r^3} + \frac{4\pi}{3}\delta^3(\mathbf{r})\right) - (\sigma_1 \cdot \hat{\mathbf{r}})(\sigma_2 \cdot \hat{\mathbf{r}}) \left(\frac{M^2}{r} + \frac{3M}{r^2} + \frac{3}{r^3}\right)\right] e^{-Mr}\,.$$

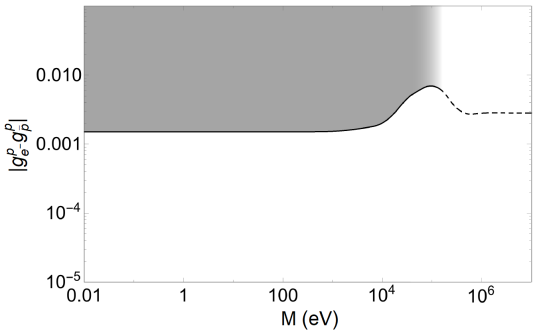

Figure 5.6: *Constraints for the interaction between an electron and an antiproton at 90% confidence level on the coupling constants as a function of boson mass, using the V_{pp} potential with the contact term [Eq.(3) in the main text] in numerical integration. The bound for large masses M is affected by absence of the proper cancellation between different terms in Eq. (3) of the main text. The affected region on the top right is shown in white above a dashed line. The shaded area is associated with the shaded area in Fig. 1(a) in the main text. See Fig. 1(a) for the accurate bound.*

We need the impact of these potentials on the energy difference between the 1^3S_1 and 2^3S_1 states in hydrogen, muonium and positronium, which are spherically symmetric. This allows us to average the V_3 potential over angles, using $\langle \hat{r}_i \hat{r}_k \rangle = \frac{1}{3}\delta_{ik}$. Note also that $\langle \sigma_1 \cdot \sigma_2 \rangle = 1$ for the total spin $S = 1$ states. As a result we only need integration of the potentials

$$\langle V_2 \rangle = \frac{e^{-Mr}}{r}, \qquad \langle V_3 \rangle = \frac{1}{3}\left(4\pi\delta(r) - \frac{M^2}{r}\right) e^{-Mr},$$

with the squared hydrogen-like wave functions for $1s$ and $2s$ orbitals

$$|\psi_1(r)|^2 = \frac{k^3 e^{-2kr}}{\pi}, \qquad |\psi_2(r)|^2 = \frac{k^3 e^{-kr}}{8\pi}\left(1 - \frac{kr}{2}\right)^2, \tag{5.9}$$

where $k = 1/a$ for hydrogen and muonium and $k = 1/2a$ for positronium, where a is the Bohr radius. For hydrogen-like ions $k = Z/a$. The results are

$$\begin{aligned} \langle \psi_1 | V_2 | \psi_1 \rangle &= \frac{4k^3}{(2k+M)^2}, \\ \langle \psi_2 | V_2 | \psi_2 \rangle &= \frac{k^3(k^2+2M^2)}{4(k+M)^4}, \end{aligned} \tag{5.10}$$

$$\begin{aligned} \langle \psi_1 | V_3 | \psi_1 \rangle &= \frac{16k^4(k+M)}{3(2k+M)^2}, \\ \langle \psi_2 | V_3 | \psi_2 \rangle &= \frac{k^3}{6} - \frac{k^3 M^2(k^2+2M^2)}{12(k+M)^4}. \end{aligned} \tag{5.11}$$

5.7 Additional plots of bounds on pseudoscalar interactions

In Figures 5.7, 5.8, 5.9, and 5.10 we show several plots referred to in Table I of the main text.

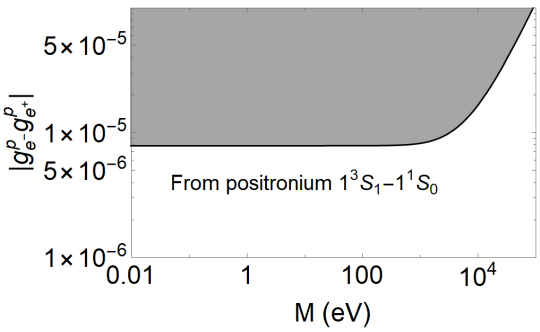

Figure 5.7: *Constraints for the electron-positron interaction at 90% confidence level on the coupling constants as a function of boson mass using Eq.(3) in the main text. The plot is based on experimental [34–36] and theoretical [37] values for the $1^3S_1 - 1^1S_0$ ground state transition in positronium [33] and our numerical estimate of the spin-dependent contribution.*

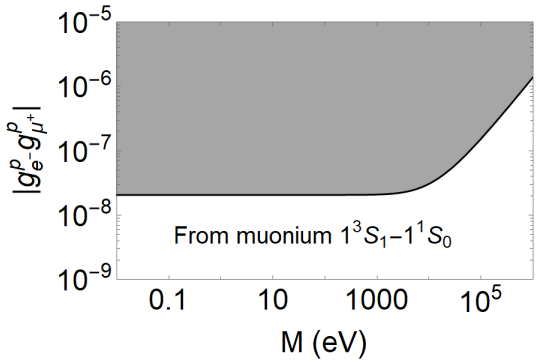

Figure 5.8: *Constraints for the interaction between an antimuon and an electron, at 90% confidence level on the coupling constants as a function of boson mass, using V_{pp} in Eq. (3) of the main text. The plot is based on experimental [41] and theoretical [42, 43] values for the hyperfine ground state transition in muonium [32] and our numerical estimate of the spin-dependent contribution.*

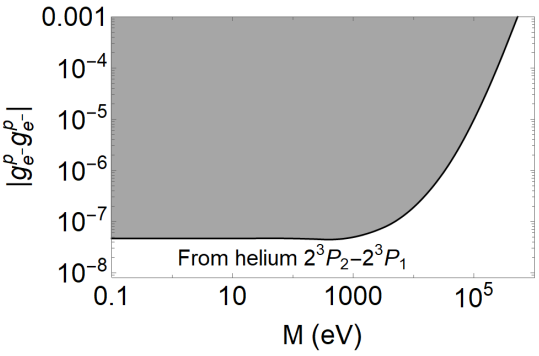

Figure 5.9: *Constraints for the interaction between electrons, at 90% confidence level on the coupling constants as a function of boson mass, using V_{pp} in Eq. (3) of the main text. The plot is based on experimental [44] and theoretical [45] values for the $2^3P_2 - 2^3P_1$ transition in helium [24] and our numerical estimate of the spin-dependent contribution.*

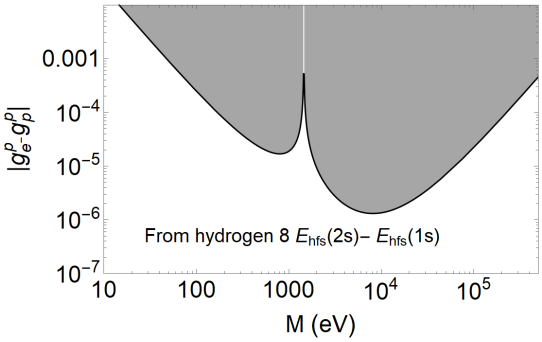

Figure 5.10: *Constraints for the electron-proton interaction, at 90% confidence level on the coupling constants as a function of boson mass, using V_{pp} in Eq.(3) of the main text. The plot is based on experimental [43, 46] and theoretical [56] values for the $8E_{\rm hfs}(2s) - E_{\rm hfs}(1s)$ difference between hyperfine transitions in hydrogen [57] and our numerical estimate of their spin-dependent contributions.*

Bibliography

[1] G. Bertone, D. Hooper, J. Silk, Phys. Rep. **405**, 279 (2005).

[2] A. Friedland, H. Murayama, M. Perelstein, Phys. Rev. D **67**, 043519 (2003).

[3] V. Flambaum, S. Lambert, M. Pospelov, Phys. Rev. D **80**, 105021 (2009).

[4] J. E. Moody and F. Wilczek, Phys. Rev. D **30**, 130 (1984).

[5] P. W. Graham, D. E. Kaplan, S. Rajendran, Phys. Rev. Lett. 115, 221801 (2015).

[6] M. S. Safronova, D. Budker, D. DeMille, Derek F. Jackson Kimball, A. Derevianko, and Charles W. Clark, Rev. Mod. Phys. **90**, 025008 (2018).

[7] Y. V. Stadnik and V. V. Flambaum, arXiv:1806.03115.

[8] M. Jiao, X. Rong, H. Liang, Y. F. Cai, and J. Du, Phys. Rev. D **101**, 115011 (2020).

[9] P. Fadeev, Y. V. Stadnik, F. Ficek, M. G. Kozlov, V. V. Flambaum, and D. Budker, Phys. Rev. A **99**, 022113 (2019).

[10] B. A. Dobrescu and I. Mocioiu, JHEP **2006**, 005 (2006).

[11] T. M. Leslie, E.Weisman, R. Khatiwada, and J. C. Long, Phys. Rev. D **89**, 114022 (2014).

[12] L. R. Hunter and D. G. Ang, Phys. Rev. Lett. **112**, 091803 (2014).

[13] Y. J Kim, P. H Chu, I Savukov, and S. Newman, Nat. Commun. **10**, 2245 (2019).

[14] W. Ji, C. B. Fu, and H. Gao, Phys. Rev. D **95**, 075014 (2017).

[15] P. C. Malta, L. P. R. Ospedal, K. Veiga, and J. A. Helayël-Neto, Adv. High Energy Phys. **2016**, 2531436 (2016).

[16] A. Parikh, Phys. Rev. D **104**, 036005 (2021).

[17] K. Gordon, *Modern Elementary Particle Physics* (Cambridge University Press, Cambridge UK, 2017).

[18] C. Smorra, Y. V. Stadnik, P. E. Blessing, M. Bohman, M. J. Borchert, J. A. Devlin, S. Erlewein, J. A. Harrington, T. Higuchi, A. Mooser, G. Schneider, M. Wiesinger, E. Wursten, K. Blaum, Y. Matsuda, C. Ospelkaus, W. Quint, J. Walz, Y. Yamazaki, D. Budker, and S. Ulmer, Nature **575**, 310 (2019).

[19] B. R. Heckel, C. E. Cramer, T. S. Cook, E. G. Adelberger, S. Schlamminger, and U. Schmidt, Phys. Rev. Lett. **97**, 021603 (2006).

[20] B. R. Heckel, E. G. Adelberger, C. E. Cramer, T. S. Cook, S. Schlamminger, and U. Schmidt, Phys. Rev. D **78**, 092006 (2008).

[21] L. Hunter, J. Gordon, S. Peck, D. Ang, and J.-F. Lin, Science **339**, 928 (2013).

[22] Y. J. Kim, P. H. Chu, and I. Savukov, Phys. Rev. Lett. **121**, 091802 (2018).

[23] F. Ficek, P. Fadeev, V. V. Flambaum, D. F. J. Kimball, M. G. Kozlov, Y. V. Stadnik, and D. Budker, Phys. Rev. Lett. **120**, 183002 (2018).

[24] F. Ficek, D. F. Jackson Kimball, M. G. Kozlov, N. Leefer, S. Pustelny, D. Budker, Phys. Rev. A **95**, 032505 (2017).

[25] C. Frugiuele and C. Peset, arXiv: 2107.13512.

[26] T. Pask, D. Barn, A. Dax, R. S. Hayano, M. Hori, D. Horváth, S. Friedreich, B. Juhász, O. Massiczek, N. Ono, A. Sót´er, and E. Widmann, Phys. Lett. B **678**, 55 (2009).

[27] V. I. Korobov and D. Bakalov, J. Phys. B: At. Mol. Opt. Phys. **34**, L519 (2001).

[28] A. Almasi, J. Lee, H. Winarto, M. Smiciklas, and M. V. Romalis, Phys. Rev. Lett. **125**, 201802 (20182020).

[29] Michael V. Romalis (private communication).

[30] S. G. Karshenboim and V. V. Flambaum, Phys. Rev. A **84**, 064502 (2011).

[31] S. G. Karshenboim, Phys. Rev. D **82**, 113013 (2010).

[32] C. Frugiuele, J. Pérez-Ríos, C. Peset, Phys. Rev. D **100**, 015010 (2019).

[33] S. Kotler, R. Ozeri, and D. F. Jackson Kimball, Phys. Rev. Lett. **115**, 081801 (2015).

[34] A. Ishida, T. Namba, S. Asai, T. Kobayashi, H. Saito, M. Yoshida, K. Tanaka, and A. Yamamoto, Phys. Lett. B **734**, 338 (2014).

[35] A. P. Mills, Jr. and G. H. Beaman, Phys. Rev. Lett. **34**, 246 (1975); A. P. Mills, Jr., Phys. Rev. A **27**, 262 (1983).

[36] M. W. Ritter, P. O. Egan, V. W. Hughes, and K. A. Woodle, Phys. Rev. A **30**, 1331 (1984).

[37] M. I. Eides and V. A. Shelyuto, Phys. Rev. D **89**, 111301(R) (2014).

[38] M. S. Fee, A. P. Mills, S. Chu, E. D. Shaw, K. Danzmann, R. J. Chichester, and D. M. Zuckerman, Phys. Rev. Lett. **70**, 1397 (1993).

[39] A. Czarnecki, K. Melnikov, and A. Yelkhovsky, Phys. Rev. A **59**, 4316 (1999).

[40] A. V. Manohar and I. W. Stewart, Phys. Rev. Lett. **85**, 2248 (2000).

[41] W. Liu, M. Boshier, S. Dhawan, et al., Phys. Rev. Lett. **82**, 711 (1999).

[42] S. G. Karshenboim, D. McKeen, and M. Pospelov, Phys. Rev. D **90**, 073004 (2014), [Addendum: Phys. Rev.D **90**, no.7, 079905(2014)].

[43] S. G. Karshenboim, Phys. Rept. **422**, 1 (2005).

[44] A. Marsman, M. Horbatsch, and E. A. Hessels, Phys. Rev. A **91**, 062506 (2015).

[45] K. Pachucki and V. A. Yerokhin, Phys. Rev. Lett. **104**, 070403 (2010).

[46] H. Hellwig, R. F. C. Vessot, M. W. Levine, P. W. Zitzewitz, D. W. Allan, and D. J. Glaze, IEEE Trans. Image Process. **19**, 200 (1970).

[47] P. W. Zitzewitz, E. E. Uzgiris, and N. F. Ramsey, Rev. Sci. Instrum. **41**, 81 (1970).

[48] L. Essen, R. W. Donaldson, E. G. Hope, and M. J. Bangham, Metrologia **9**,128 (1973).

[49] D. Morris, Metrologia **7**, 162 (1971).

[50] V. S. Reinhard and J. Lavanceau, in *Proceedings of the 28th Annual Symposium on Frequency Control, 29–31 May 1974, U.S. Army Electronics Command, Fort Mammouth, New Jersey (Electronic Industries Association, Washington, DC, 1974)*, p. 379.

[51] P. Petit, M. Desaintfuscien, and C. Audoin, Metrologia **16**, 7 (1980).

[52] J. Vanier and R. Larouche, ibid. **14**, 31 (1976).

[53] Y. M. Cheng, Y. L. Hua, C. B. Chen, J. H. Gao, and W. Shen, IEEE Trans. Instrum. Meas. **29**, 316 (1980).

[54] S. G. Karshenboim, Can. J. Phys. **78**, 639 (2000).

[55] N. Kolachevsky, A. Matveev, J. Alnis, C. G. Parthey, S. G. Karshenboim, and T. W. Hänsch, Phys. Rev. Lett. **102**, 213002 (2009).

[56] S. G. Karshenboim and V. G. Ivanov, Can. J. Phys. **83**, 1063 (2005); S. G. Karshenboim, S. I. Eidelman, P. Fendel, V. G. Ivanov, N. N. Kolachevsky, V. A. Shelyuto, and T. W. Hansch, Nucl. Phys. B, Proc. Suppl. **162**, 260 (2006).

[57] S. G. Karshenboim, Phys. Rev. A **83**, 062119 (2011).

Chapter 6

Gravity Probe Spin: Prospects for measuring general-relativistic precession of intrinsic spin using a ferromagnetic gyroscope

Phys. Rev. D **103**, 044056 (2021)

Pavel Fadeev[1], Tao Wang[2], Y. B. Band[3], Dmitry Budker[1,4], Peter W. Graham[5], Alexander O. Sushkov[6], and Derek F. Jackson Kimball[7]

[1] *Helmholtz Institute Mainz, Johannes Gutenberg University, 55099 Mainz, Germany*
[2] *Department of Physics, Princeton University, Princeton, New Jersey 08544, USA*
[3] *Department of Chemistry, Department of Physics, Department of Electro-Optics, and the Ilse Katz Center for Nano-Science, Ben-Gurion University, Beer-Sheva 84105, Israel*
[4] *Department of Physics, University of California at Berkeley, Berkeley, California 94720-7300, USA*
[5] *Department of Physics, Stanford Institute for Theoretical Physics, Stanford University, California 94305, USA*
[6] *Department of Physics, Boston University, Boston, Massachusetts 02215, USA*
[7] *Department of Physics, California State University - East Bay, Hayward, California 94542-3084, USA*

An experimental test at the intersection of quantum physics and general relativity is proposed: measurement of relativistic frame dragging and geodetic precession using intrinsic spin of electrons. The behavior of intrinsic spin in spacetime dragged and warped by a massive rotating body is an experimentally open question, hence the results of such a measurement could have important theoretical consequences. Such a measurement is possible by using mm-scale ferromagnetic gyroscopes in orbit around the Earth. Under conditions where the rotational angular momentum of a ferromagnet is sufficiently small, a ferromagnet's angular momentum is dominated by atomic electron spins and is predicted to exhibit macroscopic gyroscopic behavior. If such a ferromagnetic gyroscope is sufficiently isolated from the environment, rapid averaging of quantum uncertainty via the spin-lattice interaction enables readout of the ferromagnetic gyroscope dynamics with sufficient sensitivity to measure both the Lense-Thirring (frame dragging) and de Sitter (geodetic precession) effects due to the Earth.

One of the most perplexing problems in theoretical physics is devising a framework encompassing Einstein's theory of general relativity (GR) and quantum mechanics (QM) [1–3].

Experimentally addressing this subject likely requires probing distances at the Planck scale, far too short to be reached in the near future [4]. Even at longer distances, there has been a dearth of experiments probing regimes where both GR and QM are essential to understand observations [5, 6]. While quantum systems have been used in measurements of gravitational phenomena, for most such experiments the measured phenomena are either not inherently quantum mechanical (e.g., atomic measurements of the gravitational redshift [7–9], where clocks are tools to observe time dilation) or the gravitational phenomena are not inherently relativistic (e.g., observations of the quantum behavior of neutrons in Earth's gravitational field [10, 11], understandable with Newtonian gravity).

We propose an experiment testing phenomena that involve both GR and QM: measurement of gravitational frame dragging [12] and geodetic precession [13], which are fundamentally general-relativistic effects, with intrinsic spin, which is a fundamentally quantum phenomenon. It is crucial to emphasize that whether or not intrinsic spins undergo general relativistic precession is an experimentally open question: to date there has been no viable way to reach the required sensitivity for direct observation of frame dragging or geodetic precession of intrinsic spins. The significance of such a test is evident from the fact that GR incorporates only classical angular momentum arising from the rotation of finite-size, massive bodies [14–16]. The key point is that GR explicitly describes effects related to angular momentum arising from the motion of mass-energy through spacetime, but does not explicitly consider effects related to spin, where the angular momentum arises from an intrinsic quantum property of point-like particles.

Heuristically, it can be argued based on Einstein's equivalence principle that intrinsic spin should behave in the same way as the angular momentum of a classical gyroscope [17–19]. Thus a reasonable theoretical approach is to use standard quantum field theory for the locally flat spacetime and treat frame dragging and geodetic precession as small perturbations to the Lorentz metric [17–22]. However, whether or not this theoretical approach is correct remains to be proven experimentally [23]; in this sense, the proposed experiment can be envisioned as an equivalence principle test in a new regime. The proposed experiment is based on electron spins; meanwhile, frame-dragging also causes light polarization to rotate [24], a measurement of which would probe the analogous effect on photon spins [25, 26].

Indeed, without guidance from experimental measurements, there are a number of open theoretical possibilities. Even at an early stage it was realized that extending GR to include effects related to intrinsic spin (as, for example, in Cartan's theory [27]) could change the microscopic structure of GR in fundamental ways, such as introducing torsion [28, 29]. In Einstein's GR, mass-energy generates and interacts with curvature of spacetime but the torsion is zero, and so vectors curve along geodesics via parallel transport but do not twist. In Cartan's extension, intrinsic spin generates and interacts with nonzero torsion, and so frames transported along geodesics curve due to the effect of mass-energy and twist due to the effect of intrinsic spin (see, for example, the review by Hehl *et al.* [30]). Thus warping of spacetime described by GR with torsion does not affect intrinsic spin in the same way as classical angular momentum, leading to order unity differences between general-relativistic precession observed with intrinsic spin and that observed with a classical gyroscope [31]. Furthermore, spin-gravity interactions deviating from the predictions of GR are common features of theories attempting to go beyond standard physics [32–35]. Thus the results of an experiment measuring general-relativistic precession with intrinsic spins would have import-

ant consequences regardless of the outcome, distinguishing between a number of different theoretical possibilities.

A measurement of general-relativistic precession effects using intrinsic spin can be viewed as a "$\mathfrak{g}-1$" test for gravity, in analogy to the $g-2$ experiments that test quantum electrodynamics [36], where g is the electron gyromagnetic ratio. In the proposed experiment, the parameter $\mathfrak{g}$ is the gyrogravitational ratio: the ratio between intrinsic spin and angular momentum coefficients in the theoretical description of relativistic precession. If gravity affects intrinsic spin identically to orbital angular momentum, then $\mathfrak{g}=1$, as expected based on Einstein's equivalence principle applied to intrinsic spin [19, 37–40]. In other approaches $\mathfrak{g}$ differs from unity: for example, $\mathfrak{g}=2$ in certain classes of Yang-Mills gravity theories [41, 42] and $\mathfrak{g}=3$ in the torsion gravity theory described in Ref. [31].

Such an experiment only recently became possible, even in principle, based on a proposal for a ferromagnetic gyroscope (FG) with unprecedented sensitivity [43]. An ideal FG is a freely floating ferromagnet whose intrinsic spin S has far greater magnitude than any rotational angular momentum L associated with precession of the ferromagnet,

$$S \approx N\hbar \gg L \approx I\Omega \ , \tag{6.1}$$

where N is the number of polarized spins in the ferromagnet, $\hbar$ is Planck's constant, I is the moment of inertia of the ferromagnet, and Ω is the precession frequency. The inequality (6.1) translates to a certain range of background magnetic fields at the position of the FG; the upper limit on the magnitude is denoted the threshold field B^* and is defined in Table 6.1. Under these conditions, in the absence of external torques, angular momentum conservation keeps the expectation value of the total angular momentum $J=S+L$ fixed with respect to the local space coordinates. The spin-lattice interaction keeps S oriented along the easy magnetic axis $\hat{n}$ and rapidly averages components of S transverse to $\hat{n}$. This rapid averaging of transverse spin components without inducing a random walk of J significantly reduces quantum noise for measurement times longer than the characteristic time scale of the spin-lattice interaction, which is $\lesssim 10^{-9}$ s in most cases. This enables exquisitely precise measurements of spin precession, as discussed in detail in Refs. [43, 44]. A number of groups are actively working on developing the requisite experimental tools to construct an FG [45–49], opening the possibility of observing relativistic frame dragging of S as we describe below.

Specifically, we investigate measurement of both the Lense-Thirring effect [12, 50] (frame dragging) and the de Sitter (geodetic precession) effect [13, 51, 52]. Both effects cause precession of a gyroscope orbiting a massive body such as the Earth: Lense-Thirring precession is caused by spacetime being dragged by the rotation of a massive body whereas de Sitter precession is caused by the motion of a gyroscope through spacetime curved by a mass (present also for a non-rotating massive body). The Lense-Thirring precession is characterized by the angular velocity vector [50],

$$\boldsymbol{\Omega}_{LT} \approx \mathfrak{g}\frac{2}{5}\frac{GM}{c^2R}3\boldsymbol{\Omega}_E\cdot\hat{\boldsymbol{R}}\hat{\boldsymbol{R}}-\boldsymbol{\Omega}_E \ , \tag{6.2}$$

where $\mathfrak{g}$ is the gyrogravitational ratio, G is Newton's gravitational constant, M is the mass of the Earth, $\boldsymbol{R}=R\hat{\boldsymbol{R}}$ is the position of the satellite relative to the center of the Earth, c is speed of light, and $\boldsymbol{\Omega}_E$ is Earth's angular velocity ($\Omega_E \approx 2\pi\times 11.6\ \mu$Hz). For a satellite

Table 6.1: *Proposed characteristics of the orbiting ferromagnetic gyroscope (FG) system for a measurement of general-relativistic spin precession. The FG is assumed to be a fully magnetized cobalt sphere in vacuum with superconducting shielding as described in the text.*

Characteristic	Notation	Approximate Value
Radius	r	1 mm
Mass density	ρ	8.86 g/cm^3
Mass	$M \approx 4\pi\rho r^3/3$	4×10^{-2} g
Moment of inertia	$I \approx 2Mr^2/5$	1.6×10^{-4} g $\cdot$ cm^2
Number of polarized spins	N	4×10^{20}
Ferromagnetic resonance frequency	ω_0	10^{11} s^{-1}
Gyroscopic threshold field	$B^* = N\hbar^2/(g\mu_B I)$	3×10^{-10} G
Gyroscopic threshold frequency	$\Omega^* = N\hbar/I$	3×10^{-3} s^{-1}
Operating magnetic field	B	10^{-11} G
Larmor precession frequency	Ω_B	10^{-4} s^{-1}
Temperature	T	0.1 K
Background gas density	n	10^3 cm^{-3}

instantaneously above the North pole at $R \approx R_E \approx 6.5 \times 10^6$ m (where R_E is Earth's radius), $\Omega_{LT} \approx 4 \times 10^{-14}$ s^{-1} for $\mathfrak{g} = 1$. The de Sitter precession in a near-Earth orbit is [50, 53]

$$\boldsymbol{\Omega}_{dS} \approx \mathfrak{g}\frac{3}{2}\frac{GM}{c^2 R^2}\hat{\boldsymbol{R}} \times \boldsymbol{v} \ , \tag{6.3}$$

where $\boldsymbol{v}$ is the satellite velocity. For the same satellite at $R \approx R_E$ one obtains $\Omega_{dS} \approx 10^{-12}$ s^{-1} for $\mathfrak{g} = 1$. Note that depending on the particular nature of the nonstandard theory of gravity, it may be the case that $\mathfrak{g}$ could take on different values for the Lense-Thirring and de Sitter effects [28, 29].

Lense-Thirring and de Sitter precession of classical angular momentum have been measured by satellite experiments, and observed in astrophysical settings [54, 55]. Gravity Probe B (GP-B), a satellite containing four highly spherical niobium-coated fused quartz gyroscopes in a cryogenic environment, measured the de Sitter precession of the rotational angular momentum of the gyroscopes to a 0.3% precision and the Lense-Thirring precession of the gyroscopes to 20% [56, 57]. A different approach was to use the satellite laser-ranging network [58] to precisely track the precession of the angular momentum associated with the orbital motion of satellites, rather than gyroscopes [59–62]. Efforts are ongoing to observe these effects by interferometry methods [63, 64].

Our proposed experiment is modeled on GP-B, where the rotating niobium-coated fused quartz spheres are replaced by FGs. To evaluate the sensitivity, we assume that the FG is housed within a satellite similar to that used in the GP-B experiment [56] and referenced via a telescope to a remote star. For our sensitivity estimates, we assume an FG with

characteristics as listed in Table 6.1: a spherical cobalt ferromagnet of radius $r \approx 1$ mm with remanent magnetization along $\hat{n}$. The direction of the magnetic moment of the FG can be measured using a Superconducting QUantum Interference Device (SQUID) to detect the magnetic flux through a pick-up loop. A pick-up loop placed at a distance $d \approx 1$ mm away from the tip of the ferromagnet with loop radius $d \sin\theta_m \approx 0.8$ mm, where $\theta_m \approx 54.74°$ is the magic angle, maximizes the flux capture and would measure a changing magnetic flux of amplitude $\Phi \approx 100\ \mathrm{G \cdot cm^2}$ as the FG precesses. The sensitivity of a low-temperature SQUID to flux change is $\delta\Phi \lesssim 10^{-13}\ \mathrm{G \cdot cm^2/\sqrt{Hz}}$ [65–68], which gives a detector-limited angular resolution for the FG of $\delta\theta_{det} \approx \delta\Phi/\Phi \lesssim 10^{-15}\ \mathrm{rad/\sqrt{Hz}}$. This translates to a detection-limited spin-precession resolution:

$$\Delta\Omega_{det} \approx 10^{-15} t[\mathrm{s}]^{-3/2}\ \mathrm{s}^{-1}\ . \tag{6.4}$$

Estimates show that the fundamental quantum noise limit for an FG is far below $\Delta\Omega_{det}$ [43].

We estimate that the dominant source of statistical uncertainty in a satellite experiment using an FG to measure GR effects is not from the detector noise of the SQUID but rather from background gas collisions that impart angular momentum to the FG, causing random walk of its spin S. Based on analysis of Ref. [43], and accounting for the spherical geometry of the FG, we find that the spin-precession resolution is limited to

$$\Delta\Omega_{gas} \approx \frac{mr^2}{6N\hbar}\sqrt{\frac{nv_{th}^3}{\pi t}}\ , \tag{6.5}$$

where m is the mass of the background gas (assumed to be He in our case since the system is under cryogenic conditions), v_{th} is the average thermal velocity of the background gas, and other relevant parameters are listed in Table 6.1, assuming a background-gas density corresponding to cryogenic ultrahigh vacuum [36]. The effects of other sources of noise are estimated to be negligible compared to the effects of background gas (see Ref. [43] and Appendix 6.1). Indeed, recent experiments studying micron-scale ferromagnets levitated above superconductors have found that gas collisions are the dominant dissipation mechanism [49].

Using a ferromagnet as a gyroscope requires exquisite shielding and control of magnetic fields in order to avoid systematic errors due to magnetic torques. We propose to use a multi-layer superconducting Pb shielding system based on the GP-B design as described in Refs. [69, 70] combined with a conventional multi-layer μ-metal shielding and magnetic-field-control coil system as described, for example, in Ref. [71]. To achieve ultralow magnetic fields, the μ-metal/coil system, with feedback provided by internal SQUID magnetometers, is used to achieve an ambient magnetic field less than 10^{-11} G, close to the noise limit of SQUID magnetometers for integration times of one second. Nested collapsed Pb foil shields are inserted within the μ-metal/coil system and subsequently cooled below the superconducting phase transition. The collapsed Pb foil shields are folded in such a manner as to minimize their internal volume. Once the temperature of the Pb is below the superconducting phase transition, the shields are expanded by unfolding them so that they have a considerably larger internal volume. Persistent currents in the superconducting shields keep the flux constant and thus the field within the expanded Pb shields is reduced by the ratio between the effective areas of the expanded and collapsed Pb foil shield. In practice, the residual field

can be reduced by a factor of more than a hundred per layer, with practical limitations due to thermoelectric currents generated in the Pb shield. For such a superconducting shield system, the magnetic field within the shield will be determined by the frozen flux. These techniques can be used to achieve a magnetic field at the position of the FG, i.e. a background magnetic field B, much smaller than the required threshold field for operation ($B^* \approx 3 \times 10^{-10}$ G, see Table 6.1 and Ref. [43]).

The proposed size and geometry for the FG (a mm-diameter sphere) is motivated by the need to minimize perturbations from background gas collisions ($\Delta\Omega_{gas} \propto 1/N$ and minimized for a spherical shape), achieve the best possible detector-limited sensitivity ($\Delta\Omega_{det} \propto 1/N$ [43]), and maintain a reasonable requirement for the threshold field B^*.

Undoubtedly, some residual magnetic field $\boldsymbol{B}$ within the shields will persist, and so the questions now become whether the FG precession frequency $\boldsymbol{\Omega}_B$ due to this field is sufficiently stable and whether $\boldsymbol{\Omega}_B$ can be reliably distinguished from the sought-after effects, $\boldsymbol{\Omega}_{LT}$ and $\boldsymbol{\Omega}_{dS}$. Superconductors can achieve remarkable stability: drifts at the level of a part in 10^{11} per hour have been measured [72]. Assuming the residual trapped field in which the FG operates is $B \sim 10^{-11}$ G, this leads to a magnetic field drift of $\approx 3 \times 10^{-26}$ G/s, which corresponds to a drift of the magnetic precession frequency of $d\Omega_B/dt \approx 2 \times 10^{-19}$ s^{-2}. For the purposes of these estimates, we assume the worst-case scenario of a linear magnetic field drift at this rate (although on long time scales the drift will likely be a random walk of $\boldsymbol{B}$ and $\boldsymbol{\Omega}_B$).

The stability of $\boldsymbol{\Omega}_B$ is crucial for distinguishing magnetic precession from the Lense-Thirring and de Sitter effects. For a residual field with $B \sim 10^{-11}$ G, $\Omega_B \approx 10^{-4}$ s^{-1}, which is much larger than the Lense-Thirring and de Sitter effects [Eqs. (6.2) and (6.3)], and thus it is important to find a way to distinguish $\boldsymbol{\Omega}_B$ from $\boldsymbol{\Omega}_{LT}$ and $\boldsymbol{\Omega}_{dS}$. In the case of the Lense-Thirring effect, $\boldsymbol{\Omega}_{LT}$ periodically varies in time in a predictable way because $\hat{\boldsymbol{R}}$ changes in time with respect to $\boldsymbol{\Omega}_E$ as the FG orbits the Earth. If the FG is placed in an elliptical orbit, both $\boldsymbol{\Omega}_{LT}$ and $\boldsymbol{\Omega}_{dS}$ could be modulated by order unity as R changes. Thus it would become possible to search for the predictable periodic variation of $\boldsymbol{\Omega}_{LT}$ and $\boldsymbol{\Omega}_{dS}$ on top of the stable background magnetic-field precession. An example of how this can be done is modelled in Appendix 6.3.

Further discrimination of $\boldsymbol{\Omega}_{LT}$ and $\boldsymbol{\Omega}_{dS}$ from $\boldsymbol{\Omega}_B$ can be obtained by using an array of FGs and taking advantage of the vectorial nature of the general-relativistic spin-precession. Consider, for example, the Lense-Thirring effect (similar arguments can be made for the de Sitter effect). If $\boldsymbol{\Omega}_B$ is parallel with $\boldsymbol{\Omega}_{LT}$, the effects add linearly to the measured spin-precession frequency: $\Omega \approx \Omega_B + \Omega_{LT}$. However, if $\boldsymbol{\Omega}_B$ is perpendicular to $\boldsymbol{\Omega}_{LT}$, the contribution of the Lense-Thirring effect is quadratically suppressed: $\Omega \approx \Omega_B + \Omega_{LT}^2/2\Omega_B$. An array of FGs in separate shields can be employed with magnetic fields oriented in different directions, such that the various FGs have different predictable periodic patterns of sensitivity to general-relativistic spin-precession effects. This will enable coherent averaging and suppress systematic errors due to field drift and local perturbations.

Additionally, it may be possible to rotate or modulate $\boldsymbol{B}$ at a frequency much faster than the orbital frequency in order to further discriminate $\boldsymbol{\Omega}_{LT}$ and $\boldsymbol{\Omega}_{dS}$ from $\boldsymbol{\Omega}_B$. This may be achieved by rotating the magnetic shielding relative to the FG since the residual magnetic field will be dominated by frozen flux rather than the finite shielding factor. Further mechanisms

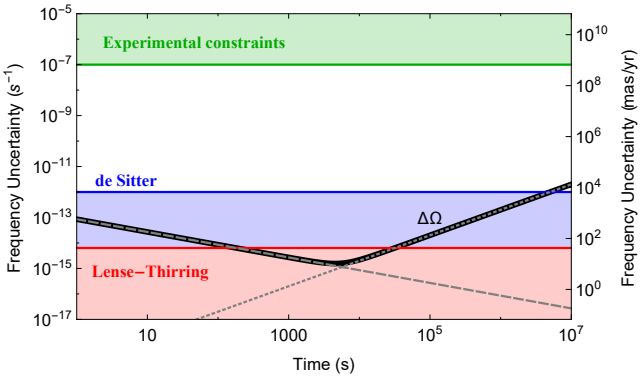

Figure 6.1: *Sensitivity to general relativistic spin-precession effects in the proposed "Gravity Probe Spin" experiment. The vertical scale on the right is in units of milliarcseconds (mas) per year. The black curve shows the projected uncertainty $\Delta\Omega$ in the measurement of the precession frequency Ω using a 1-mm radius spherical FG under conditions listed in Table 6.1. This curve results from two contributions summed in quadrature. First, the short-term statistical uncertainty is dominated by background gas collisions [Eq. (6.5), dashed gray line]. Second, the long-term uncertainty in the measurement is expected to be dominated by magnetic field drift within the superconducting magnetic shields, here assumed to be linear with rate 3×10^{-26} G/s (dotted gray line). The blue line and light blue shaded area indicate the level beyond which the measurements are sensitive to the de Sitter effect [13, 51, 52] and the red line and pink shaded area indicate the level beyond which the measurements are sensitive to the Lense-Thirring effect [12, 50], calculated for the GP-B orbit and gyrogravitational ratio $\mathfrak{g} = 1$ [Eqs. (6.2) and (6.3)]. The green line and light green shaded area show existing experimental constraints on anomalous gravity-induced spin-precession [81–83].*

to improve signal detection are possible: if two types of ferromagnetic materials are used, such that the materials' gyromagnetic ratios are opposite, their magnetic precession is in opposite directions but the relativistic precession are in the same direction. For control of systematic errors, it may also be interesting to consider experiments with materials having high net spin polarization but negligible magnetization, high magnetization but negligible spin polarization, and varying ratios of quantum orbital angular momentum to intrinsic spin, such as used in torsion pendulum experiments measuring exotic spin-dependent interactions [73–75].

Relative motion between the SQUID pick-up loop and the freely floating FG is another source of noise and systematic error that will require precise control. Errors due to this relative motion will ultimately be limited by the satellite position/orientation feedback control system referenced to the star-tracking telescope. We assume a star-tracking telescope and position/orientation feedback control similar to that used by GP-B, which had a long-term accuracy corresponding to 5×10^{-10} rad [76–78], which would provide sufficient stability for measurement of the $\mathfrak{g} = 1$ de Sitter and Lense-Thirring effects. Related technical issues are the trapping and release of the FG once the satellite is in orbit, damping of rotational motion of the FG such that $L \ll S$, vibrations of the pick-up coil, and the effect of electrostatic

and magnetic forces on the FG that might accelerate the FG relative to the satellite housing. Protocols for measurement and control of the FG and pick-up coil motion will need to be designed and could, for example, involve damping of FG motion using eddy currents [45] induced in a retractable conductor or various trapping and cooling techniques that have been developed to control the motion of macroscopic objects [79, 80]. The effects of stray electric fields and patch potentials, important issues for GP-B [56], are considered in Appendix 6.1.2. Overall, we expect that the ultimate accuracy of an FG-based measurement of general relativistic spin precession will be determined by the SQUID sensitivity, collisions of residual gas molecules with the FG, and magnetic field drift.

Figure 6.1 shows the scaling of uncertainty in the measurement of the spin precession frequency Ω as a function of time considering the aforementioned effects. In principle, the projected measurement sensitivity of such a "Gravity Probe Spin" experiment is sufficient to measure the de Sitter and Lense-Thirring effects for $\mathfrak{g} = 1$. Consequently, stringent bounds will result on parametrized post-Newtonian (PPN) physics, scalar-tensor theories, and other standard-model extensions [37]. By comparing the sensitivity of Gravity Probe Spin to existing experimental bounds on anomalous gravity-induced spin-precession [81–83] as shown in Fig. 6.1, the proposed experiment has the potential to explore many decades of unconstrained parameter space.

In conclusion, we have described a satellite experiment using mm-scale ferromagnetic gyroscopes that has the potential to perform the first measurement of gravitational frame-dragging of electrons' intrinsic spins. This experiment, building on the technology of Gravity Probe B, would be a unique test at the intersection of quantum mechanics and general relativity.

Acknowledgments

This research was supported by the Heising-Simons and Simons Foundations, the U.S. National Science Foundation under Grant No. PHY-1707875, the DFG through the DIP program (FO703/2-1), and by a Fundamental Physics Innovation Award from the Gordon and Betty Moore Foundation. The work of DB supported in part by the DFG Project ID 390831469: EXC 2118 (PRISMA+ Cluster of Excellence), the European Research Council (ERC) under the European Union Horizon 2020 Research and Innovation Program (grant agreement No. 695405), and the DFG Reinhart Koselleck Project. The work of AS supported in part by the US National Science Foundation grant 1806557, US Department of Energy grant DE-SC0019450, the Heising-Simons Foundation grant 2015-039, the Simons Foundation grant 641332, and the Alfred P. Sloan foundation grant FG-2016-6728.

6.1 Experimental requirements

6.1.1 Magnetic torque noise

An additional source of error affecting an FG, not considered in Ref. [43], was pointed out in Ref. [44] (see also Appendix 6.2). As noted in Ref. [43], the spin-lattice coupling gen-

erates stochastic fluctuations of the FG's magnetic moment μ described by the fluctuation-dissipation theorem. In the presence of a nonzero magnetic field B, this leads to a stochastic $\mu \times B$ torque acting on the FG, which in turn causes a random walk of the FG's spin axis J. This coupling of the FG to the external environment through B generates noise in a measurement of the precession frequency:

$$\Delta\Omega_B \approx \frac{\Omega_B^2}{\omega_0 \Omega^*} \sqrt{\frac{4\alpha k_B T}{\hbar N t}} \,, \tag{6.6}$$

where k_B is Boltzmann's constant and α is the Gilbert damping constant, taken as 0.01. Under the conditions of our proposed experiment, $\Delta\Omega_B$ is significantly smaller than other sources of error.

6.1.2 Electric field requirements

A precessing FG located in a spatial region with non-vanishing electric field may experience an electric-field-induced torque. In this section we estimate the requirements on the electric field and its gradient, in order to keep the FG precession rate due to this torque below the expected signal level.

A conducting sphere in a uniform electric field experiences no torque, since the induced electric dipole moment is parallel to the electric field. However a slight deviation from a spherical shape breaks the symmetry of the polarizability tensor, and, in general, causes the induced dipole moment to be at an angle to the electric field. Assuming the FG is shaped as a prolate spheroid (with semi-axes a, b, and c, where $a > b = c$) with small eccentricity $\varepsilon = \sqrt{1 - b^2/a^2}$, the correction to the depolarization factors is of order ε^2 [84]. The torque on such a slightly non-spherical FG of radius r in a uniform electric field E can be estimated (in cgs units) as $\tau_e^{(1)} \approx \varepsilon^2 r^3 E^2/5$. The resulting precession rate is given by $\Omega_e^{(1)} = \tau_e^{(1)}/(N\hbar)$. The requirement to keep this rate below Ω_{LT} with $\mathfrak{g} = 1$, $\Omega_e^{(1)} \lesssim 4 \times 10^{-14}$ s^{-1}, imposes the following condition on the product between the eccentricity and the magnitude of the electric field:

$$|\varepsilon E| \lesssim 3 \times 10^{-6}\,\mathrm{V/cm}. \tag{6.7}$$

It should be noted that, in practice, the requirement on $|\varepsilon E|$ may be significantly reduced since orbital modulation can be used to distinguish general relativistic precession effects from nominally constant background torques, as discussed in Sec. 6.3.

An electric field gradient E' will exert a force on the FG, which must balance with all the other forces in the FG at its equilibrium point. Since there are certainly other forces, there may be a non-vanishing electric field gradient, which exerts a torque on the FG even if it is a perfect sphere. The magnitude of this torque can be estimated as $\tau_e^{(2)} \approx r^4 E E'$. The resulting precession rate is given by $\Omega_e^{(2)} = \tau_e^{(2)}/(N\hbar)$. The requirement to keep this rate below Ω_{LT} with $\mathfrak{g} = 1$, $\Omega_e^{(2)} \lesssim 4 \times 10^{-14}$ s^{-1}, imposes the following condition on the product between the electric field and the gradient:

$$|EE'| < 10^{-11}\,\mathrm{V^2/cm^3}. \tag{6.8}$$

A procedure to reduce systematic error due to $\tau_e^{(2)}$, often employed in precision measurement protocols, is to apply a large electric field E and use a measurement of $\Omega_e^{(2)}$ to minimize E', then apply a large electric field gradient E', and use a measurement of $\Omega_e^{(2)}$ to minimize E. Performed iteratively, this procedure can enable cancellation of residual E and E' to relatively high precision, and will also help reduce systematic error due to nonsphericity of the FG [Eq. (6.7)].

The electric field at the equilibrium position of the FG is created by potentials on proximal surfaces. To control electric fields these surfaces have to be coated with a high-conductivity material, such as gold. Nonetheless, surface-potential patches of order 10 mV are still likely to be present [85]. The electric field from such patches falls off exponentially with distance to the surface. We estimate that 10 mV patches with spatial scale of < 1 mm create electric fields that satisfy requirements described by Eqs. (6.7) and (6.8) provided the FG is > 1 cm away from the surface. These estimates give the requirements on the surface preparation necessary to ensure that electrostatic precession remains below the GR signal. Again, FG precession due to GR effects can be distinguished from $\Omega_e^{(1)}$ and $\Omega_e^{(2)}$ through orbital modulation as described in Sec. 6.3.

6.1.3 Summary

Considerable development of FG technology is required before a Gravity-Probe-Spin-type experiment will become feasible. First and foremost, the gyroscopic precession of a ferromagnet as predicted in Ref. [43] has to be experimentally observed and studied. Several groups are working on ground-based laboratory experiments studying the behavior of micron-scale levitated ferromagnets [45–49]. To provide an overall sense of the target parameters for a Gravity Spin experiment, Table 6.2 shows the benchmarks required to achieve the estimated sensitivity plotted in Fig. 6.1. These benchmarks are derived from the requirements to achieve the estimated best experimental sensitivity to precession, $\Delta\Omega_{opt} \approx 10^{-15}$ rad/s, achieved after an integration time of $T_{opt} \approx 6 \times 10^4$ s.

Although, as discussed in the text, many of these benchmark experimental parameter values have been achieved in laboratory settings, the achievable experimental parameters have yet to be studied in the context of FG precession. Furthermore, achieving these benchmarks in a satellite presents a host of additional challenges. Detailed studies of these sources of noise and systematic errors in experiments with FGs in both laboratory and microgravity environments will be required on the way toward a Gravity Probe Spin experiment. Nonetheless, based on the estimates presented here and the modeling presented in Appendices 6.2 and 6.3, achieving these milestones appears possible in principle. We reiterate that the main purpose of our manuscript is to highlight the potential payoff of developing FG devices for fundamental physics experiments and to motivate further experimental efforts.

6.2 Model of a ferromagnetic gyroscope

We model the FG dynamics using the formulation described in Ref. [44]. The FG is taken to be a single-domain spherical magnet with body-fixed moments of inertia $\mathcal{I}_X = \mathcal{I}_Y = \mathcal{I}_Z \equiv \mathcal{I}$.

Table 6.2: *Summary of benchmark experimental parameters necessary to achieve the sensitivity plotted in Fig. 6.1. Electric-field-related estimates assume the nearly spherical FG has an eccentricity of* ~ 0.01.

Parameter	Benchmark
Magnetic flux sensitivity	$\delta\Phi \lesssim 5 \times 10^{-8}\ \frac{\text{G}\cdot\text{cm}^2}{\sqrt{\text{Hz}}}$
Magnetic field	$B \lesssim 10^{-11}$ G
Magnetic field drift	$\lvert B\rvert \lesssim 3 \times 10^{-26}$ G/s
Magnetic field gradient	$B' \lesssim 10^{-13}$ G/cm
Electric field	$E \lesssim 5 \times 10^{-5}$ V/cm
Electric field gradient	$E' \lesssim 6 \times 10^{-9}$ V/cm^2
Electric patch potentials	$\delta V \lesssim 0.01$ V
Background gas density	$n \lesssim 10^3$ cm^{-3}
Temperature	$T \lesssim 0.1$ K
Angular stability	$\Delta\theta \lesssim 6 \times 10^{-11}$ rad

It is subject to a uniform magnetic field $\mathbf{B}$ and general-relativistic precession described by the angular velocity vector $\mathbf{\Omega}_r$. The Hamiltonian describing this system is given by:

$$\hat{H} = \underbrace{\frac{1}{2\mathcal{I}}\hat{\mathbf{L}}^2}_{H_R} \underbrace{-(\omega_0/\hbar)(\hat{\mathbf{S}}\cdot\hat{\mathbf{n}})^2}_{H_A} \underbrace{-\hat{\boldsymbol{\mu}}\cdot\mathbf{B}}_{H_B} + \underbrace{\mathbf{\Omega}_r\cdot(\hat{\mathbf{L}}+\mathfrak{g}\hat{\mathbf{S}})}_{H_\Omega}\,. \tag{6.9}$$

In the rotational Hamiltonian H_R, $\hat{\mathbf{L}}$ is the orbital angular momentum operator; in the anisotropy Hamiltonian H_A [86], $\hat{\mathbf{S}}$ is the spin operator, $\hat{\mathbf{n}}$ is the operator for the unit vector in the direction of the easy magnetization axis, and ω_0 is the ferromagnetic resonance frequency; in the Zeeman Hamiltonian term H_B, $\hat{\boldsymbol{\mu}} = g\mu_B\hat{\mathbf{S}}$ is the magnetic moment operator (μ_B is the Bohr magneton and g is the Landé factor); and H_Ω is the Hamiltonian accounting for the angular velocity vector $\mathbf{\Omega}_r$ related to general-relativistic precession, where $\mathfrak{g}$ is the gyrogravitational ratio (if $\mathfrak{g} = 1$ the GR effects for intrinsic spin $\mathbf{S}$ and orbital angular momentum $\mathbf{L}$ are the same).

The dynamics are treated semiclassically since the FG has large spin expectation value S, as done in Ref. [44]. We write the Heisenberg equations of motion in reduced units, defining dimensionless vectors: the unit spin $\mathbf{m} \equiv \mathbf{S}/S$, the orbital angular momentum $\boldsymbol{\ell} \equiv \boldsymbol{L}/S$, the total angular momentum, $\mathbf{j} = \mathbf{m} + \boldsymbol{\ell}$ and the unit vector in the direction of the magnetic field

$\mathbf{b} = \mathbf{B}/B$:

$$\begin{aligned}\dot{\mathbf{m}} = {} & \omega_B \mathbf{m} \times \mathbf{b} + \omega_0 (\mathbf{m} \times \mathbf{n})(\mathbf{m} \cdot \mathbf{n}) \\ & - \alpha \mathbf{m} \times (\dot{\mathbf{m}} - \boldsymbol{\Omega} \times \mathbf{m}) + \mathfrak{g} \boldsymbol{\Omega}_r \times \mathbf{m} \,, \end{aligned} \tag{6.10}$$

$$\begin{aligned}\dot{\boldsymbol{\ell}} = {} & -\omega_0 (\mathbf{m} \times \mathbf{n})(\mathbf{m} \cdot \mathbf{n}) \\ & + \alpha \mathbf{m} \times (\dot{\mathbf{m}} - \boldsymbol{\Omega} \times \mathbf{m}) + \boldsymbol{\Omega}_r \times \boldsymbol{\ell} \,, \end{aligned} \tag{6.11}$$

$$\dot{\mathbf{n}} = (\boldsymbol{\Omega} + \boldsymbol{\Omega}_r) \times \mathbf{n} \,, \tag{6.12}$$

where the angular velocity vector $\boldsymbol{\Omega}$ is given by

$$\boldsymbol{\Omega} = \omega_1 \boldsymbol{\ell} = \omega_1 (\mathbf{j} - \mathbf{m}) \,. \tag{6.13}$$

Here $\omega_B = g\mu_B |\mathbf{B}|$ is the Larmor frequency and $\omega_1 = S/\mathcal{I}$ is the nutation frequency. The terms containing the Gilbert damping coefficient α account for Gilbert dissipation of spin components perpendicular to the easy magnetization axis. The Gilbert damping is due to interactions of the spin with internal degrees of freedom such as lattice vibrations (phonons), spin waves (magnons), thermal electric currents, etc. [87, 88]. The Gilbert damping tends to lock the spin to the easy axis because the components of the spin orthogonal to the easy axis quickly decay [44]. Hence we take $\mathbf{m}(t) = \mathbf{n}(t)$, which also simplifies the numerical calculations. Adding the spin and rotational angular-momentum in Eqs. (6.10) and (6.11), we obtain

$$\dot{\mathbf{j}} = \dot{\mathbf{m}} + \dot{\boldsymbol{\ell}} = \omega_B \mathbf{m} \times \mathbf{b} + \boldsymbol{\Omega}_r \times \boldsymbol{\ell} + \mathfrak{g} \mathbf{m} \,, \tag{6.14}$$

$$= \omega_B \mathbf{m} \times \mathbf{b} + \boldsymbol{\Omega}_r \times \mathbf{j} + \mathfrak{g} - 1 \mathbf{m} \,. \tag{6.15}$$

Using Eq. (6.13) and our approximation that $\mathbf{m} = \mathbf{n}$ (hence $\mathbf{m} \times \mathbf{n} = 0$), Eq. (6.12) can be rewritten in the form

$$\dot{\mathbf{m}} \quad = \quad (\omega_1 \mathbf{j} + \boldsymbol{\Omega}_r) \times \mathbf{m} \,. \tag{6.16}$$

We can solve Eqs. (6.15) and (6.16) for a given satellite trajectory that specifies $\boldsymbol{\Omega}_r(t) = \boldsymbol{\Omega}_{\rm LT}^{(1)}(t) + \boldsymbol{\Omega}_{\rm dS}^{(1)}(t)$ to obtain the dynamics of the FG. The upper index (1) in the expression for $\boldsymbol{\Omega}_r(t)$ sets $\mathfrak{g} = 1$ in Eqs. (2) and (3) of the main text, since in the modelling $\mathfrak{g}$ is present in the dynamical equations such that it distinguishes between the effect of general-relativistic precession of intrinsic spin as compared to that of angular momentum, as seen in Eq. (6.9). The results of the modeling for illustrative cases are discussed in the next section.

6.3 Orbital dynamics of ferromagnetic gyroscope

In order to use an FG to measure GR-induced spin precession, it is crucial to have a distinct signature that can be differentiated from background effects. As noted in the main text,

periodic motion of an FG at harmonics of the orbital frequency arise due to the modulation of $\mathbf{\Omega}_{LT}$ and $\mathbf{\Omega}_{dS}$ as the FG orbits the Earth. This offers a method to distinguish GR-induced spin precession from Larmor precession and nutation, whose frequencies are constant in time for fixed B.

To illustrate the use of orbital modulation in a "Gravity Probe Spin" experiment, we model the behavior of an FG in a circular polar orbit around the Earth with radius $R \approx 7,000$ km (Fig. 6.2). The FG operates in an external magnetic field $\mathbf{B}$ oriented along Earth's rotation axis Ω_E, chosen to be the z-axis of our coordinate system. As discussed in Sec. 6.2, the spin is locked along the direction of its easy magnetization axis by Gilbert damping, and is initially prepared to be perpendicular to B, along x. In this geometry, precession due to the de Sitter effect [Eq. (3) in the main text] is both constant in time, since R is constant, and quadratically suppressed, since Ω_{dS} is perpendicular to Ω_B and $\Omega_{dS} \ll \Omega_B$. On the other hand, the Lense-Thirring precession $\Omega_{LT}(t)$ is parallel to Ω_B when the FG is at the north and south poles and as such is modulated at twice the orbital frequency [Eq. (2) in the main text]. The orbital modulation of $\Omega_{LT}(t)$ can be understood based on the fact that the Lense-Thirring effect generated by the rotation of the Earth is the gravito-magnetic equivalent of a dipole field, and possesses axial symmetry about z.

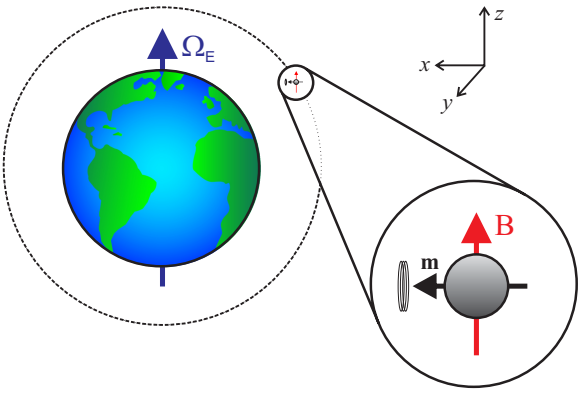

Figure 6.2: *Conceptual schematic diagram of a "Gravity Probe Spin" experiment. A freely floating spherical FG located within a superconducting shield is in a circular polar orbit. The magnetic field B (from the frozen flux in the superconducting shields) is oriented parallel to the direction of Earth's rotation axis Ω_E, both designated to point along z. The insert shows the initial orientation of the FG's magnetic moment and spin m along the x axis. The pick-up coil measures the FG's magnetization along x. This geometry is designed for the detection of the Lense-Thirring effect.*

The results of a numerical solution of Eqs. (6.15) and (6.16) for the FG dynamics, $\mathbf{m}(t)$, under the conditions described above are shown in Figs. 6.3 and 6.4. The figures show power spectral densities (PSDs) of the estimated flux Φ through a pick-up coil in the geometry described in the text [see discussion surrounding Eq. (4) in the main text] as the FG orbits the Earth as shown in Fig. 6.2. In order to clearly discern the Lense-Thirring effect in Figs. 6.3 and 6.4, we choose $\mathfrak{g} = 10^7$, just below the present experimental constraints on the

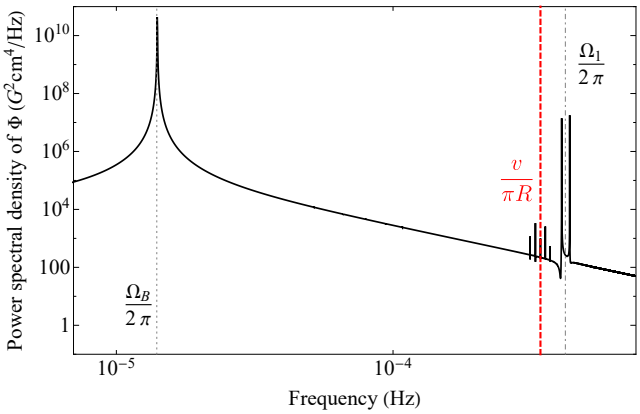

Figure 6.3: *Estimated power spectral density (PSD) of the time-dependent flux signal* Φ *due to a precessing FG that would be measured by a SQUID pick-up coil as in Fig. 6.2. The plot shows the PSD of a time-domain signal of duration* $T = 3 \times 10^7$ *s obtained by numerical solution of differential equations based on the model discussed in Sec. 6.2. The parameters of the model match those listed in Table 6.1. The gray dotted line marks the Larmor frequency,* $\Omega_B/(2\pi)$*, the gray dot-dashed line marks the nutation frequency,* $\Omega_1/(2\pi)$*, and the red dashed line marks the second harmonic of the orbital frequency,* $v/(\pi R)$*. In order to enhance visualization, for this plot we choose* $\mathfrak{g} = 10^7$ *for the Lense-Thirring effect, just below the present experimental constraints (Fig. 1 in the main text).*

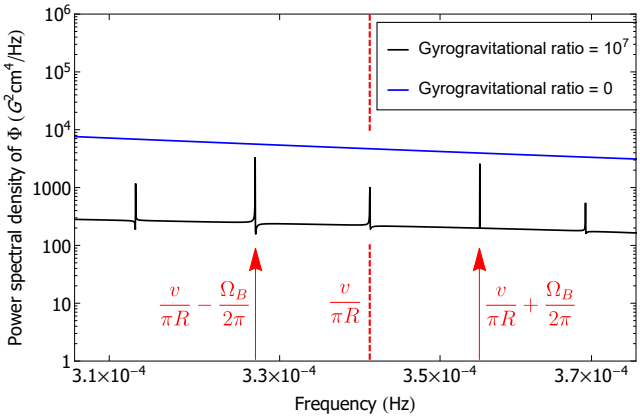

Figure 6.4: *The black curve shows the PSD of the time-dependent flux signal* Φ *under the same conditions and assumptions as in Fig. 6.3. The blue curve, vertically offset for easier comparison, shows the PSD of the time-dependent flux signal* Φ *for the case where the gyrogravitational ratio* $\mathfrak{g} = 0$*. The dashed red line marks the second harmonic of the orbital frequency,* $v/(\pi R)$*, and prominent signals at sidebands shifted by the Larmor frequency are indicated by the red arrows at* $v/(\pi R) \pm \Omega_B/(2\pi)$*. Note also sidebands at* $v/(\pi R) \pm \Omega_B/\pi$*.*

Lense-Thirring effect (Fig. 1 in the main text). The PSD shown in Fig. 6.3 demonstrates, as expected, that the dominant signal is at the Larmor frequency (Ω_B) and prominent signals due to nutation appear at Ω_1 with sidebands at $\Omega_1 \pm \Omega_B$. There is a noticeable signal due

to the Lense-Thirring effect (with $\mathfrak{g} = 10^7$) at the second harmonic of the orbital frequency, $2\pi \times v/(\pi R)$ (in rad/s, note the frequency units in the figures are Hz). In Fig. 6.4, the signal with $\mathfrak{g} = 10^7$ is compared to the signal for $\mathfrak{g} = 0$ near the second harmonic of the orbital frequency, $2v/R$. Figure 6.5 shows $\Delta\Phi^2$, the PSD of the difference between the measured flux from two FGs situated in magnetic fields with equal magnitudes but opposite directions ($\pm\hat{z}$) for the case where $\mathfrak{g} = 1$. The $\mathfrak{g} = 1$ case would correspond to the case of particular interest where intrinsic spin and orbital angular momentum behave identically in general relativity. As in the case where $\mathfrak{g} = 10^7$, there are noticeable signals arising from modulation of FG precession at twice the orbital frequency due to the Lense-Thirring effect, seen at the sideband frequencies $2v/R \pm \Omega_B$. The results of the modeling demonstrate that the Lense-Thirring effect indeed modulates FG precession at the second harmonic of the orbital frequency, offering a signature of GR effects distinguishable from effects that do not vary periodically with the orbit. The asymmetric shapes of the peaks in Figs. 6.3, 6.4, 6.5, and subsequent plots are described by Fano line shapes [89] that result from the interference of the background and the resonances in the PSD.

For reference, the expected measurement noise floor due to collisions with residual background gas, based on Eq. (5) in the main text, is estimated to be

$$\delta(\Phi^2)_{gas} \approx \frac{10^{-9}}{\sqrt{T}}\ \mathrm{G^2cm^4/Hz}\ . \tag{6.17}$$

Comparing $\delta(\Phi^2)_{gas}$ to the signals plotted in Fig. 6.5 show that for a measurement times $T \gtrsim 10^4$ s the Lense-Thirring precession for $\mathfrak{g} = 1$ should be resolvable, consistent with the sensitivity estimates shown in Fig. 1 of the main text.

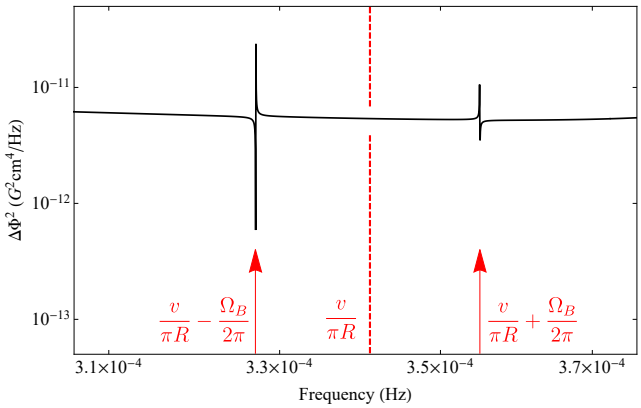

Figure 6.5: *PSD of the difference in time-dependent flux signal with* $\mathfrak{g} = 1$ *between two gyroscopes. The gyroscopes situated in opposite external magnetic fields along the* z *axis. The conditions and assumptions are the same as in Fig. 6.3. The dashed red line marks the second harmonic of the orbital frequency,* $v/(\pi R)$*, and prominent signals at sidebands shifted by the Larmor frequency are indicated by the red arrows at* $v/(\pi R) \pm \Omega_B/(2\pi)$*.*

Employing a different geometry for the FG, namely orienting B parallel to Ω_{dS}, gives linear sensitivity to Ω_{dS} (in which case sensitivity to Ω_{LT} is quadratically suppressed). By putting the satellite into an elliptical orbit (Fig. 6.6), R and v are modulated and a distinct

signature in the PSD of Φ can be obtained for the de Sitter effect, as demonstrated in Fig. 6.7. Figure 6.7 gives the result of modeling the FG dynamics for a polar elliptical orbit with eccentricity of 0.3: the PSD shows the difference between the measured flux from two FGs situated in magnetic fields with equal magnitudes but opposite directions ($\pm\hat{y}$) assuming $\mathfrak{g} = 1$. Signals due to the de Sitter effect are observed at sidebands around the orbital frequency ω_{orb},

$$\omega_{orb} = \sqrt{\frac{G\,M}{a^3}}\,, \tag{6.18}$$

where a is the semi-major axis of the ellipse. This is expected since $\Omega_{dS}(t)$ is periodic with the modulation of R and v as the FG orbits, leading to a signal at the first harmonic of ω_{orb}.

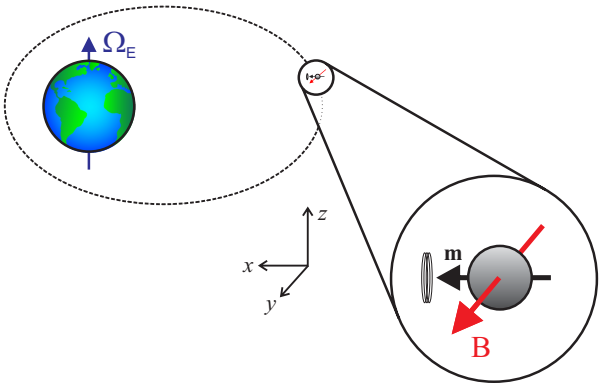

Figure 6.6: *Conceptual schematic diagram of a "Gravity Probe Spin" experiment similar to that shown in Fig. 6.2 except that the orbit is elliptical and the magnetic field B is directed along the y-axis, perpendicular to the orbital plane. This geometry is designed for the detection of the de Sitter effect.*

In conclusion, the numerical modeling demonstrates that, in principle, for particular experimental geometries there exist potentially measurable signatures of general relativistic precession of an FG at harmonics of the orbital frequency.

Bibliography

[1] C. Rovelli, *Quantum Gravity* (Cambridge University Press, 2007).

[2] C. Kieffer, *Quantum Gravity* (Oxford University Press, 2012).

[3] A. Eichhorn, Front. Astron. Space Sci. **5**, 47 (2019).

[4] M. E. Peskin and D. V. Schroeder, *An Introduction to Quantum Field Theory* (Addison-Wesley Pub. Co, Reading, Mass, 1995).

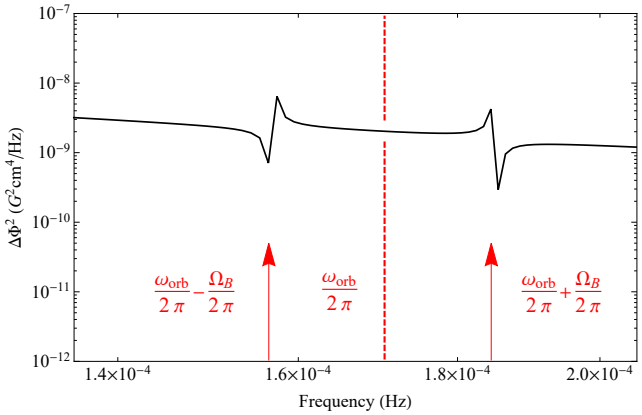

Figure 6.7: *PSD of the difference in time-dependent flux signal with* $\mathfrak{g} = 1$ *between two gyroscopes. The gyroscopes are situated, respectively, in external magnetic fields along the y axis with equal magnitudes and opposite directions. The FG is modelled for the duration of* 10^6 *s in a polar elliptical orbit as indicated in Fig. 6.6, with ellipticity of 0.3. The dashed red line marks the first harmonic of the orbital frequency,* $\omega_{orb}/(2\pi)$*, and prominent signals at sidebands shifted by the Larmor frequency are indicated by the red arrows at* $\omega_{orb}/(2\pi) \pm \Omega_B/(2\pi)$*.*

[5] R. Howl, L. Hackermüller, D. E. Bruschi, and I. Fuentes, Advances in Physics: X **3**, 1383184 (2018).

[6] *Experimental Search for Quantum Gravity*, edited by S. Hossenfelder (Springer, 2018).

[7] R. V. Pound, G. A. Rebka, Phys. Rev. Lett. **4**, 337 (1960).

[8] H. Müller, A. Peters, S. Chu, Nature **463**, 926 (2010).

[9] C. W. Chou, D. B. Hume, T. Rosenband and D. J. Wineland, Science **329**, 1630 (2010).

[10] R. A. Colella, W. Overhauser, and W. A. Werner, Phys. Rev. Lett. **34**, 1472 (1975).

[11] V. V. Nesvizhevsky, H. G. Börner, A. K. Petoukhov, H. Abele, S. Baeßler, F. Rueß, Th. Stöferle, A. Westphal, A. M. Gagarski, G. A. Petrov, and A. V. Strelkov, Nature (London) **15**, 297 (2002).

[12] J. Lense and H. Thirring, Physikalishe Zeitschrift **19** (1918).

[13] W. de Sitter, Mon. Not. Roy. Astron. Soc. **77**, 155 (1916).

[14] C. W. Misner, K. S. Thorne, J. A. Wheeler, and D. I. Kaiser, *Gravitation* (Princeton University Press, 2017).

[15] A. Zee, *Einstein gravity in a nutshell* (Princeton University Press, 2013).

[16] C. M. Will, *Theory and experiment in gravitational physics* (Cambridge University Press, 2018).

[17] B. Mashhoon, Class. Quant. Grav. **17**, 2399 (2000).

[18] B. Mashhoon and Y. N. Obukhov, Phys. Rev. D **88**, 064037 (2013).

[19] R. J. Adler, P. Chen, and E. Varani, Phys. Rev. D **85**, 025016 (2012).

[20] A.J. Silenko and O.V. Teryaev, Phys. Rev. D **71**, 064016 (2005).

[21] A.J. Silenko and O.V. Teryaev, Phys. Rev. D **76**, 061101(R) (2007).

[22] A. J. Silenko, ArXiv: 0802.4443 (2008).

[23] J. D. Tasson, Phys. Rev. D **86**, 124021 (2012).

[24] S. Kopeikin and B. Mashhoon, Phys. Rev.D **65**, 064025 (2002).

[25] M. Sereno, Monthly Notices of the Royal Astronomical Society **356**, 381 (2005).

[26] M. L. Ruggiero and A. Tartaglia, Monthly Notices of the Royal Astronomical Society **374**, 847 (2007).

[27] É. Cartan, C.R. Acad. Sci. (Paris) **174**, 593 (1922).

[28] V. de Sabbata and C. Sivaram, *Spin and torsion in gravitation* (World Scientific, 1994).

[29] W. T. Ni, Rep. Prog. Phys. **73**, 056901 (2010).

[30] F. W. Hehl, P. von der Heyde, G. D. Kerlick, and J. M. Nester, Rev. Mod. Phys. **48**, 393 (1976).

[31] J. Audretsch, Phys. Rev. D **24**, 1470 (1981).

[32] D. Oriti, *Approaches to Quantum Gravity* (Cambridge University Press, Cambridge U.K., 2009).

[33] S. Capozziello and M. de Laurentis, Phys. Rep. **509**, 167 (2011).

[34] M. S. Safronova, D. Budker, D. DeMille, D. F. Jackson Kimball, A. Derevianko, and C.W. Clark, Rev. Mod. Phys. **90**, 025008 (2018).

[35] *Equations of Motion in Relativistic Gravity*, edited by D. Puetzfeld, C. Lämmerzahl, and B. Schutz (Springer, 2015).

[36] D. Hanneke, S. Fogwell and G. Gabrielse, Phys. Rev. Lett. **100**, 120801 (2008).

[37] J. M. Overduin, Class. Quantum Grav. **32**, 224003 (2015).

[38] D. Singh, G. Papini, Nuovo Cimento B **115**, 223 (2000).

[39] I. M. Pavlichenkov, EPL **85**, 40008 (2009).

[40] W.-T. Ni, Int. J. Mod. Phys. Conf. Ser. **40**, 1660010 (2016).

[41] V. Parameswaran Nair, *Concepts in Particle Physics* (World Scientific, 2018).

[42] F. W. Hehl, J. Lemke, and E. W. Mielke, in *Geometry and Theoretical Physics* edited by J. Debrus and A. C. Hirshfeld (Springer, Heidelberg, 1991), pp. 56 — 140.

[43] D. F. Jackson Kimball, A. O. Sushkov, and D. Budker, Phys. Rev. Lett. **116**, 190801 (2016).

[44] Y. B. Band, Y. Avishai, and A. Shnirman, Phys. Rev. Lett. **121**, 160801 (2018).

[45] T. Wang, S. Lourette, S. R. O'Kelley, M. Kayci, Y. B. Band, D. F. Jackson Kimball, A. O. Sushkov, and D. Budker, Phys. Rev. Appl. **11**, 044041 (2019).

[46] J. Gieseler, A. Kabcenell, E. Rosenfeld, J. D. Schaefer, A. Safira, M. J. A. Schuetz, C. Gonzalez-Ballestero, C. C. Rusconi, O. Romero-Isart, and M. D. Lukin, Phys. Rev. Lett. **124**, 163604 (2020).

[47] C. Timberlake, G. Gasbarri, A. Vinante, A. Setter, and H. Ulbricht, Appl. Phys. Lett. **115**, 224101 (2019).

[48] P. Huillery, T. Delord, L. Nicolas, M. Van Den Bossche, M. Perdriat, and G. Hétet, Phys. Rev B **101**, 134415 (2020).

[49] A. Vinante, P. Falferi, G. Gasbarri, A. Setter, C. Timberlake, and H. Ulbricht, Phys. Rev. Applied **13**, 064027 (2020).

[50] L. I. Schiff, Phys. Rev. Lett. **4**, 215 (1960).

[51] W. J. A. Schouten, Versl. Kon. Ak. Wet. **27**, 214 (1918).

[52] A. D. Fokker, Versl. Kon. Ak. Wet. **29**, 611 (1920).

[53] R. Ruffini and C. Sigismondi editors, *Nonlinear Gravitodynamics, the Lense-Thirring effect*, World Scientific pub., Singapore (2003).

[54] V. V. Krishnan et al., Science **367**, 577 (2020).

[55] J. van Leeuwen et al., Astrophys. J. **798**, 118 (2015).

[56] C. W. F. Everitt, et. al., Phys. Rev. Lett. **106**, 221101 (2011).

[57] C. W. F. Everitt, B. Muhlfelder, D. B. DeBra, B. W. Parkinson, J. P. Turneaure, A. S. Silbergleit, E. B. Acworth, M. Adams, R. Adler, W. J. Bencze, and J. E. Berberian, Classical and Quantum Gravity **32**, 224001 (2015).

[58] M.R. Pearlman, J.J. Degnan, J.M. Bosworth, Adv. Space Res. **30**, 135 (2002).

[59] D. M. Lucchesi, L. Anselmo, M. Bassan, C. Magnafico, C. Pardini, R. Peron, G. Pucacco, M. Visco, Universe **5**, 141 (2019).

[60] L. Iorio, Universe **4**, 113 (2018).

[61] I. Ciufolini, A. Paolozzi, E. C. Pavlis, R. Koenig, J. Ries, V. Gurzadyan, R. Matzner *et al.*, Eur. Phys. J. C **76**, 120 (2016).

[62] I. Ciufolini, E. Pavlis, F. Chieppa, E. Fernandes-Vieira, and J. Pérez-Mercader, Science **279**, 2100 (1998).

[63] A. Di Virgilio, F. Bosi, U. Giacomelli, A. Simonelli, G. Terreni, A. Basti, N. Beverini, G. Carelli, D. Ciampini, F. Fuso, A. Ortolan, A. Porzio, ArXiv: **0802.4443** (2020).

[64] A. Di Virgilio, M. Allegrini, A. Beghi, J. Belfi, N. Beverini, F. Bosi, B. Bouhadef, M. Calamai, G. Carelli, D. Cuccato, E. Maccioni, A. Ortolan, G. Passeggio, A. Porzio, M.L. Ruggiero, R. Santagata, A. Tartaglia, C. R. Phys. **15**, 866 (2014).

[65] D. D. Awschalom, J. R. Rozen, M. B. Ketchen, W. J. Gallagher, A. W. Kleinsasser, R. L. Sandstrom, and B. Bumble, Appl. Phys. Lett. **53**, 2108 (1988).

[66] O. Usenko, A. Vinante, G. Wijts, and T. H. Oosterkamp, Appl. Phys. Lett. **98**, 133105 (2011).

[67] W. Gardner, Sean T. Halloran, Erik A. Lucero, and Kathryn A. Moler, Rev. Sci. Inst. **79**, 053704 (2008).

[68] J. Clarke and A. I. Braginski, eds., *The SQUID Handbook Vol. 1* (Wiley, Weinheim, 2004).

[69] M. A. Taber, D. O. Murray, J. M. Lockhart, D. J. Frank, and D. Donegan, Advances in Cryogenic Engineering **39**, 161 (1994).

[70] J. C. Mester, J. M. Lockhart, B. Muhlfelder, D. O. Murray, and M. A. Taber, Advances in Space Research **25**, 1185 (2000).

[71] V. V. Yashchuk, S.-K. Lee, and E. Paperno, V.V. Yashchuk, in *Optical Magnetometry* edited by D. Budker and D. F. Jackson Kimball (Cambridge University Press, Cambridge, 2013).

[72] R. S. Van Dyck Jr., D. L. Farnham, S. L. Zafonte, and P. B. Schwinberg, Rev. Sci. Inst. **70**, 1665 (1999).

[73] R. C. Ritter, L. I. Winkler, and G. T. Gillies. Phys. Rev. Lett. **70**, 701 (1993).

[74] L. S. Hou and W. T. Ni, Mod. Phys. Lett. A **16**, 763 (2001).

[75] B. R. Heckel, W. A. Terrano, and E. G. Adelberger, Phys. Rev. Lett. **111**, 151802 (2013).

[76] H. Dougherty, D. Hegel, J. Kirschenbaum, J. V. Beukel, W. Reeve, and J. Kasdin, Control Engineering Practice, **3**, 1119 (1995).

[77] D.-H. Gwo, S. Wang, K. A. Bower, D. E. Davidson, P. Ehrensberger, L. Huff, E. Romero, M. T. Sullivan, K. Triebes, and J. A. Lipa, Adv. Space Res. **32** 1401 (2003).

[78] J. W. Conklin, M. Adams, W. J. Bencze, D. B. DeBra, G. Green, L. Herman, T. Holmes, B. Muhlfelder, B. W. Parkinson, A. S. Silbergleit, and J. Kirschenbaum, Class. Quant. Grav. **32**, 224015 (2015).

[79] J. D. Teufel, T. Donner, D. Li, J. W. Harlow, M. S. Allman, K. Cicak, A. J. Sirois, J. D. Whittaker, K. W. Lehnert, and R. W. Simmonds, Nature **475**, 359 (2011).

[80] J. Chan, T. P. Mayer Alegre, A. H. Safavi-Naeini, J. T. Hill, A. Krause, S. Gröblacher, M. Aspelmeyer, and O. Painter, Nature **478**, 89 (2011).

[81] B. J. Venema, P. K. Majumder, S. K. Lamoreaux, B. R. Heckel, and E. N. Fortson, Phys. Rev. Lett. **68**, 135 (1992).

[82] B. R. Heckel, E. G. Adelberger, C. E. Cramer, T. S. Cook, S. Schlamminger, and U. Schmidt, Phys. Rev. D **78**, 092006 (2008).

[83] D. F. Jackson Kimball, J. Dudley, Y. Li, D. Patel, and J. Valdez, Phys. Rev. D **96**, 075004 (2017).

[84] L. D. Landau, L. P. Pitaevskii, E. M. Lifshitz EM, *Electrodynamics of Continuous Media: Volume 8 (Course of Theoretical Physics)*, Butterworth-Heinemann; 2 edition (1984).

[85] W.J. Kim WJ, A.O. Sushkov, D.A.R. Dalvit, S.K. Lamoreaux, Physical Review A **81**, 022505 (2010).

[86] W. F. Brown Jr., Phys. Rev. **130**, 1677 (1963).

[87] H. B. Callen and T. A. Welton, Phys. Rev. **83**, 34 (1951).

[88] T. L. Gilbert, IEEE Transactions on Magnetics **40**, 3443 (2004).

[89] U. Fano, Phys. Rev. **124**, 1866 (1961).

Chapter 7

Ferromagnetic Gyroscopes for Tests of Fundamental Physics

Quantum Sci. Technol. 6, 024006 (2021)

Pavel Fadeev[1,2], Chris Timberlake[3], Tao Wang[4], Andrea Vinante[3,5], Y. B. Band[6], Dmitry Budker[1,2,7], Alexander O. Sushkov[8],Hendrik Ulbricht[3], Derek F. Jackson Kimball[9]

[1] *Helmholtz-Institut, GSI Helmholtzzentrum für Schwerionenforschung, 55128 Mainz, Germany*

[2] *Johannes Gutenberg-Universität Mainz, 55128 Mainz, Germany*

[3] *School of Physics and Astronomy, University of Southampton, SO17 1BJ Southampton, United Kingdom*

[4] *Department of Physics, Princeton University, Princeton, New Jersey 08544, USA*

[5] *Istituto di Fotonica e Nanotecnologie – CNR and Fondazione Bruno Kessler, I-38123 Povo, Trento, Italy*

[6] *Department of Chemistry, Department of Physics, Department of Electro-Optics, and the Ilse Katz Center for Nano-Science, Ben-Gurion University, Beer-Sheva 84105, Israel*

[7] *Department of Physics, University of California at Berkeley, Berkeley, California 94720-7300, USA*

[8] *Department of Physics, Boston University, Boston, Massachusetts 02215, USA*

[9] *Department of Physics, California State University - East Bay, Hayward, California 94542-3084, USA*

A ferromagnetic gyroscope (FG) is a ferromagnet whose angular momentum is dominated by electron spin polarization and that will precess under the action of an external torque, such as that due to a magnetic field. Here we model and analyze FG dynamics and sensitivity, focusing on practical schemes for experimental realization. In the case of a freely floating FG, we model the transition from dynamics dominated by libration in relatively high externally applied magnetic fields, to those dominated by precession at relatively low applied fields. Measurement of the libration frequency enables in situ determination of the magnetic field and a technique to reduce the field below the threshold for which precession dominates the FG dynamics. We note that evidence of gyroscopic behavior is present even at magnetic fields much larger than the threshold field below which precession dominates. We also model the dynamics of an FG levitated above a type-I superconductor via the Meissner effect, and find that for FGs with dimensions larger than about 100 nm the observed precession frequency is reduced compared to that

of a freely floating FG. This is due to an effect akin to negative feedback that arises from the distortion of the field from the FG by the superconductor. Finally we assess the sensitivity of an FG levitated above a type-I superconductor to exotic spin-dependent interactions under practical experimental conditions, demonstrating the potential of FGs for tests of fundamental physics.

7.1 Introduction

Gyroscopes are valuable tools for metrology and navigation due to their sensitivity to rotations. For example, the Gravity Probe B space mission contained several spinning spheres made of fused quartz and coated with a layer of niobium [1]. Changes in the direction of angular momentum and rate of rotation of these spheres were detected by a Superconducting QUantum Interference Device (SQUID). In a different technique, ring laser interferometers (optical gyroscopes based on the Sagnac effect) have been used for continuous measurement of the Earth rotation and tilt [2]. Yet another approach observes gyroscopic motion due to precession of molecules, atoms and nuclei [3]. In the present work, we investigate how the intrinsic spin of electrons can play the role of a gyroscope.

Atoms, molecules, and nuclei, that can possess angular momentum due to their rotational motion as well as due to intrinsic spin, can act as gyroscopes [4–8]. Atomic, molecular, and nuclear gyroscopes have proven to be particularly useful for precision tests of fundamental physics [9], including tests of Lorentz symmetry [10–12], searches for exotic spin-dependent interactions [13–16], dark matter experiments [17–20], and measurements of electric dipole moments [21–23] and gravitational dipole moments [24–26]. It has recently been proposed that a ferromagnet can act as a new type of gyroscope that may be particularly useful for precision tests of fundamental physics [27]. However, in order to realize the potential sensitivity of a ferromagnetic gyroscope (FG), it is essential to decouple the ferromagnet from the environment, e.g., by requiring either microgravity or some method of frictionless suspension. A promising platform for FG-based fundamental physics experiments involves levitating an FG above a superconducting surface by taking advantage of the Meissner effect [28–32]. In the present work we model the dynamics of a freely floating FG and the dynamics of an FG levitated above a perfect type-I superconductor (SC). We find that the response of an FG to external torques is considerably modified in the case of an FG levitated above an SC: the precession frequency can be reduced by orders of magnitude as compared to that for a freely floating FG. Taking this effect into account, we analyze the sensitivity of an FG levitated above an SC to torques from exotic fields [9].

Under conditions where the angular momentum of a ferromagnet is dominated by the intrinsic spin of the polarized electrons, an applied torque is predicted to cause gyroscopic precession of the ferromagnet [27]. If such a ferromagnetic gyroscope (FG) can be sufficiently isolated from the environment, a measurement of the precession can yield sensitivity to torques far beyond that of other systems (such as atomic magnetometers [33] and conventional gyroscopes [34]). The high sensitivity of an FG is a result of the rapid averaging of quantum noise [27, 35]. A key enabling technology for practical realization of an FG is a method of near frictionless suspension. One approach is to levitate a ferromagnet above an SC [28]. Recently, there has been considerable interest and progress in development of sensors based on ferromagnets levitated above SCs [28–32, 36].

Magnetization dynamics of ferromagnets, including precession and nutation motions, have been observed in thin films using ferromagnetic resonance [37, 38]. Such dynamics occur on characteristic time scales of a picosecond, related to the time it takes for the electron spins to relax to their equilibrium state. The FG concept concerns dynamics on time scales much longer than the aforementioned relaxation time, involving macroscopic motion of the whole ferromagnet.

In the present work, we propose a strategy for a proof-of-principle experiment aimed at observing FG precession, and analyze a concrete example of such an experiment involving a levitating sphere above a type-I SC. We model the behavior of an FG levitated above an SC and compare to the behavior of a freely floating FG. Qualitative and quantitative differences are observed in the precession dynamics of the FG in the two cases. In relation to tests of fundamental physics, FGs have recently been proposed as tools to measure general-relativistic precession [39]; here we extend this discussion to show how FGs can be used in other searches for new physics.

As discussed in Ref. [27], in order for a ferromagnet to exhibit spin precession in an applied magnetic field, it should be in the regime where the intrinsic spin S due to the magnetization exceeds the classical rotational angular momentum L associated with the physical rotation of the ferromagnet, $S \gg L$. In the opposite case, where the orbital angular momentum associated with precession exceeds that of the spin along the axis, the ferromagnet "tips over" or, in the undamped case, oscillates or librates about its equilibrium orientation along the applied magnetic field. These two regimes can be identified as the precessing regime and the tipping regime. Ferromagnetic compass needles operate in the tipping regime — they tip along the direction of the external magnetic field. Atomic and nuclear spins are in the precessing regime — they precess around the direction of the external magnetic field.

Let us reformulate the criterion $L \ll S$ for a ferromagnet to be in the precessing regime in the following way: the product of the moment of inertia I and the precession frequency Ω (that represents the classical rotational angular momentum of the system) should be smaller than the spin content of the ferromagnet

$$I\Omega \ll N\frac{\hbar}{2}\,, \tag{7.1}$$

where N is the number of polarized spins and $\hbar$ is Planck's constant, such that each electron has an intrinsic spin of $\hbar/2$. Rephrasing (7.1) as a bound on frequency, we have

$$\Omega \ll \Omega^* = \frac{N\hbar}{2I}\,, \tag{7.2}$$

or as a bound on the external magnetic field B applied on the ferromagnet,

$$|B| \ll B^* = \left|\frac{\hbar\Omega^*}{g\mu_B}\right|\,. \tag{7.3}$$

Here g is the Landé g-factor and μ_B is the Bohr magneton. If the applied magnetic field B is smaller than B^*, we expect the ferromagnet to be in the precessing regime.

One of the key features of an FG is the fact that a torque on the electron spins generates macroscopic rotation of the ferromagnet. This behavior of an FG is closely related to the

Barnett [40] and Einstein-de Haas [41, 42] effects. In contrast to nuclear spins, whose precession is largely decoupled from the crystal lattice as observed in solid-state nuclear magnetic resonance (NMR) experiments, in a ferromagnet there is strong coupling between electron spins and the crystal lattice via the exchange interaction. These internal dynamics governing an FG are well-described by the Landau-Lifshitz-Gilbert model [43, 44]. Thus, when the electron spins within the ferromagnet are made to precess, the entire ferromagnet rotates.

Constructing an FG by creating suitable conditions for a magnet to precess instead of tipping opens the possibility of a sensitive measurement device. For instance, by bringing a SQUID near the FG and measuring the change in magnetic flux as the FG precesses, the torques acting on the FG can be precisely measured [27].

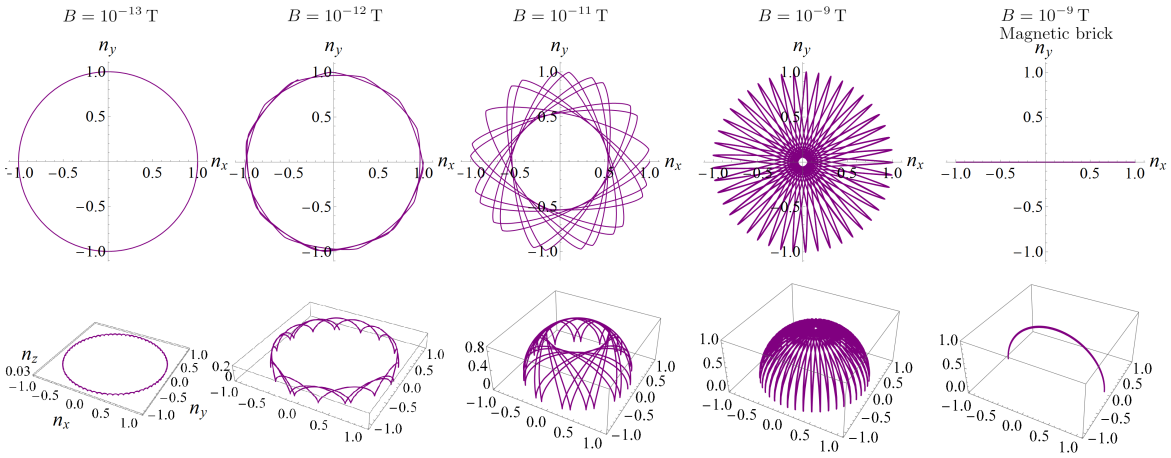

Figure 7.1: *Precession and nutation motions of a ferromagnet in an external magnetic field B whose direction is perpendicular to the plane. The modelled ferromagnet has a radius of 30 μm and contains 7×10^{15} electron spins. Depicted is the spin vector $\check{\mathrm{n}}$ of initial position along the x axis, whose projection onto the x-y plane is shown in the upper row. The lower row shows the motion in three dimensions. As B grows the precession interweaves with nutation such that the latter dominates, resulting eventually in a librational mode around the direction of B. For the depicted ferromagnet, the threshold magnetic field B^* [Eq. (7.3)] below which precession motion is dominant compared to libration, is 7×10^{-12} T. The last column depicts the case of a "magnetic brick", a hypothetical ferromagnet with zero spin polarization but equivalent magnetization.*

7.2 Model of a freely floating ferromagnetic gyroscope

To better understand the dynamics of an FG, we model a freely floating FG in space subjected to a constant magnetic field $\boldsymbol{B}$, similar to the modelling in Ref. [39]. A weak magnetic field causes precession of the FG with Larmor frequency

$$\omega_L = \frac{g_e \mu_B}{\hbar} B = \gamma B \ , \tag{7.4}$$

where g_e is the electron g–factor, and γ is the gyromagnetic ratio. We consider a spherical FG with radius of 30 μm and 7×10^{15} electron spins, identical to the microsphere used in the experiment described in Ref. [30]. Note that the threshold precession frequency Ω^* described in Eq. (7.2) is equal to the Einstein-de Haas frequency

$$\omega_I = \frac{S}{I} = \frac{N\hbar}{2I} \ , \tag{7.5}$$

where $I = 2mr^2/5$ is the moment of inertia for a sphere of mass m and radius r. The frequency ω_I plays the role of the nutation frequency in the zero magnetic field limit for the FG dynamics.

The equations of motion for the ferromagnet are

$$\frac{\partial \boldsymbol{j}}{\partial t} = \omega_L \left(\boldsymbol{n} \times \hat{\boldsymbol{B}} \right) \ , \tag{7.6}$$

$$\frac{\partial \boldsymbol{n}}{\partial t} = \omega_I \left(\boldsymbol{j} \times \boldsymbol{n} \right) \ , \tag{7.7}$$

where we defined the following dimensionless vectors: the unit spin $n \equiv S/S$, the rotational angular momentum $\boldsymbol{\ell} \equiv \boldsymbol{L}/S$, and the total angular momentum $j = n + \boldsymbol{\ell}$. Equations (7.6) and (7.7) are derived from Landau-Lifshitz-Gilbert equations under the assumption that the spin vector is locked to the easy axis, as was done in the modelling of the FG in [35, 39].

Solving for $\boldsymbol{j}(t)$ and $\boldsymbol{n}(t)$, Fig. 7.1 shows the different kinds of motions of a freely floating FG in an external magnetic field. For magnetic fields below the threshold in Eq. (7.3) the precession motion is prominent. In the intermediate regime $B \approx B^*$ both precession and nutation manifest. At fields much larger than B^* the amplitude of the nutation grows so large that it manifests as oscillation, i.e. libration, of the ferromagnet about the direction of the applied magnetic field. Note that even in the case where libration is the dominant motion, precession of the plane of libration can still be observed. The frequencies observed in the periodic FG dynamics in each regime can be obtained by analytical approximate solutions of the equations of motion [45].

7.3 Experimental strategy

To observe precession of a ferromagnetic gyroscope, we propose to work at an external magnetic field weaker than the threshold, below which precession dominates (at sufficiently low magnetic fields, the amplitude of nutation becomes relatively small so that the dynamics of the FG are dominated by the precession). Generally, in experiments, this will require both shielding and careful control of the external magnetic field. Fortunately, the ferromagnet itself can be used as a magnetometer even for fields larger than the threshold field for precession by measuring the libration frequency ω_l. Oscillation of a ferromagnet at the libration frequency ω_l was observed in soft ferromagnetic levitating particles [32] (denoted there as ω_ϕ) and with ferromagnets levitating above type-I SC [30]. For a hard ferromagnet, ω_l is the geometrical average of the Larmor frequency ω_L and the Einstein–de Haas frequency ω_I [29]

$$\omega_l^2 = \omega_L \omega_I \ . \tag{7.8}$$

Since the libration frequency ω_l depends on the magnetic field, it can be used to measure and reduce the magnetic field until precession dominates the dynamics. For a freely floating FG, as one reduces the magnetic field below the threshold field defined in Eq. (7.3), the frequencies will split on the logarithmic scale (Fig. 7.2) such that they can be resolved in the magnetic flux spectrum measured by a SQUID pick-up loop.

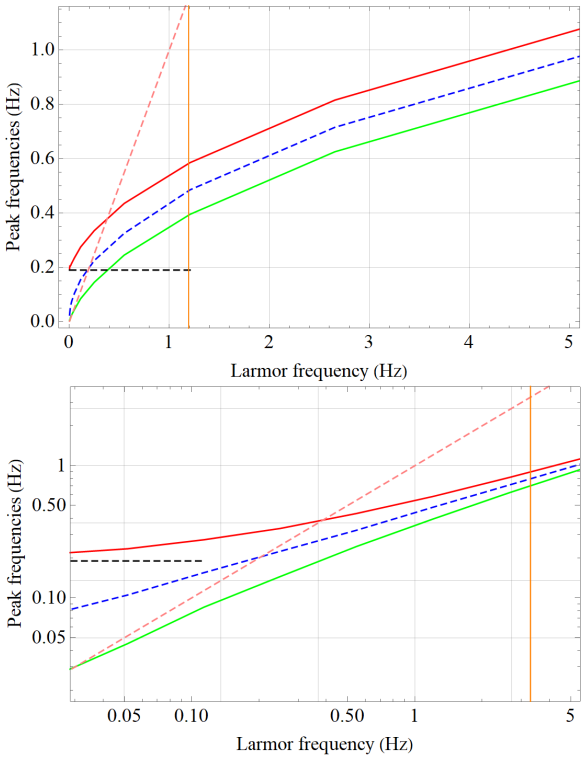

Figure 7.2: *Modelling the dynamics of an FG by Eqs. (7.6) and (7.7). In linear and logarithmic scales, presented are the frequencies of the maxima in the spectrum of FG dynamics as can be measured with a SQUID pick-up loop, as a function of the Larmor frequency ω_L. The external magnetic field direction is perpendicular to the precession plane, as in Fig. 7.1. The SQUID pick-up loop measures the flux from the FG in the horizontal direction x. The middle line (dashed blue) is the sole frequency appearing in the spectrum of a "magnetic brick" (hypothetical ferromagnet with zero spin polarization but equivalent magnetization, see main text) with a radius of 30 μm in an external magnetic field. The red and green curves are the frequencies of a fully spin-polarized ferromagnet with the same radius, corresponding respectively to nutation and precession frequencies. As might be expected from Eq. (7.8), the blue line is the geometric average of the red and green lines, above the threshold frequency. The orange vertical line is the threshold frequency Ω^*. The dashed pink line is the Larmor frequency of Eq. (7.4). The dashed black line, ω_I, corresponds to the nutation frequency in the zero magnetic field limit.*

Quantitatively, solving Eqs. (7.6) and (7.7) for $\boldsymbol{j}(t)$ and $\boldsymbol{n}(t)$ for various ω_L, the model of the dynamics of a freely floating FG shows signals at two distinct frequencies in the magnetic flux observed along the x-direction (perpendicular to the magnetic field applied along z).

These frequencies are fractionally split in low magnetic fields, that is, the difference between the frequencies, normalized by their geometric average, becomes bigger at lower frequencies, as shown in Fig. 7.2, where the fractional behaviour is emphasized on the logarithmic scale. The apparent splitting of the nutation and precession curves on the logarithmic scale in Fig. 7.2 (the red and green curves) points to the transition from the librational behaviour above the threshold (the vertical line) into the precession and nutation motion below the threshold. The two frequencies can be viewed as a modulation of a central frequency (dashed blue line in Fig. 7.2) which appears in the case of a "magnetic brick", a hypothetical ferromagnet with zero spin polarization ($j = 0$ $n + \ell$) but equivalent magnetization. The concept of a magnetic brick is introduced to separate, in the model, effects due to magnetic torques from effects related to the gyroscopic nature of the ferromagnet.

As for the precession frequency, green curve in Fig. 7.2, it deviates from the Larmor frequency in Eq. (7.4), as expected from the interplay between nutation and precession motions [46]. The Larmor frequency is a dashed pink line with a unit slope on the linear scale of Fig. 7.2. The parameters used in the model match those for the experimental setup discussed in the next section, which result in $\omega_I = 1.193$ rad/s [30]. This ω_I is plotted as a dashed black horizontal line in Fig. 7.2.

Above the threshold, the librational-mode frequency ω_l can be observed and used to measure and control the magnetic field. Using this technique the magnetic field can be tuned below the threshold field where the FG dynamics clearly display precession and nutation, demonstrating the gyroscopic behavior of a ferromagnet and confirming experimentally the prediction of precession. In the next section we examine this experimental strategy in the context of a ferromagnetic microsphere levitating above a type-I SC.

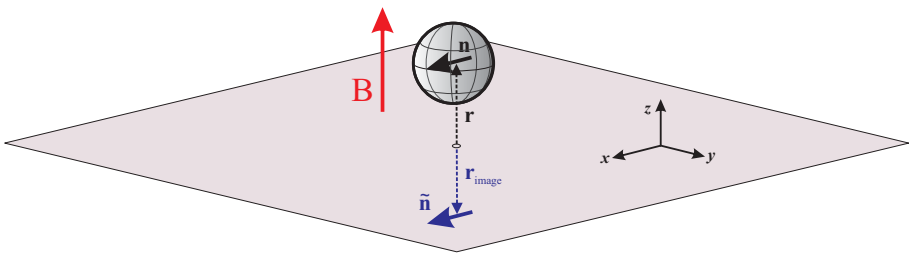

Figure 7.3: *Schematic setup for an FG levitated above a type-I superconductor. The sphere and arrow labeled* $\boldsymbol{n}$ *represent the FG, the gray plane represents the surface of the SC, the blue arrow labeled* $\tilde{\boldsymbol{n}}$ *represents the image dipole, the red arrow indicates the external magnetic field applied along the vertical direction,* r *is the vector pointing to the location of the center of the sphere and* r_{image} *is the vector pointing to the location of the image dipole.*

7.4 Ferromagnetic gyroscope levitated above a type-I superconductor

A promising avenue for experimental realization of an FG are optomechanical and magnetomechanical systems, for instance: a ferromagnet levitated by magnetic or electric fields. In particular, the motion, dynamics and stability of a magnetically levitated ferromagnet have been studied [45] and are in agreement with expectations regarding the precessing and tipping regimes. Here we consider a ferromagnetic microsphere levitating above a type-I SC (Fig. 7.3). In this case, the expulsion of the magnetic field from the superconductor by the Meissner effect creates a field in the region above the superconductor mathematically equivalent to that from image dipole. The image–dipole magnetic field pushes the microsphere up while gravity pulls it down. To investigate the effect of the superconductor on the FG dynamics, we include the field from the image dipole in the modelling.

The image field $\mathfrak{B}$ is a magnetic field emanating from the image dipole located at a vertical distance $2z$ (center to center) below the levitating FG, where z is the height of the FG above the SC plane. In SI units,

$$\mathfrak{B} = -\frac{\mu_0}{4\pi}\frac{\mu}{\tilde{r}^5}\left\{3\ \tilde{\boldsymbol{r}}\ (\tilde{\boldsymbol{r}}\cdot\tilde{\boldsymbol{n}}) - \tilde{\boldsymbol{n}}\ \tilde{r}^2\right\}\ , \tag{7.9}$$

where μ_0 is the permeability of free space, $\tilde{\boldsymbol{r}}$ is relative to the position of the image dipole

$$\begin{aligned} \tilde{r} &= r - r_{\text{image}}\ , \\ r &= (x, y, z)\ , \\ r_{\text{image}} &= (x, y, -z)\ , \end{aligned} \tag{7.10}$$

$\mu\tilde{\boldsymbol{n}}$ is the magnetic moment of the image dipole and $\mu\boldsymbol{n}$ is the magnetic moment of the levitating ferromanget

$$\begin{aligned} \boldsymbol{n} &= (n_x, n_y, +n_z)\ , \\ \tilde{\boldsymbol{n}} &= (n_x, n_y, -n_z)\ . \end{aligned} \tag{7.11}$$

Here we take the origin of the coordinate system to be on the SC plane. The image dipole has the same horizontal component of the magnetic moment as the FG, and opposite vertical component.

To include $\mathfrak{B}$ into the equations of motion in Sec. 7.2, we derive the Larmor frequency associated with this image dipole field

$$\omega_{\mathfrak{B}} = \gamma\mathfrak{B}\ , \tag{7.12}$$

so that Eq. (7.6) contains the term

$$\omega_{\mathfrak{B}}\left(\boldsymbol{n}\times\hat{\mathfrak{B}}\right)\ . \tag{7.13}$$

Moreover, we include the ferromagnet center-of-mass equations of motion

$$\frac{\partial\boldsymbol{p}}{\partial t} = \frac{\mu}{2}\nabla\left(\mathfrak{B}\cdot\boldsymbol{n}\right) + m\boldsymbol{g}\ , \tag{7.14}$$

$$\frac{\partial\boldsymbol{r}}{\partial t} = \frac{\boldsymbol{p}}{m}\ , \tag{7.15}$$

where $\boldsymbol{p}$ is the FG center-of-mass momentum, $\boldsymbol{g}$ is the gravitational acceleration, and the factor 1/2 is a consequence of the image dipole being not frozen in type-I SC, i.e., following the levitating dipole [47–49].

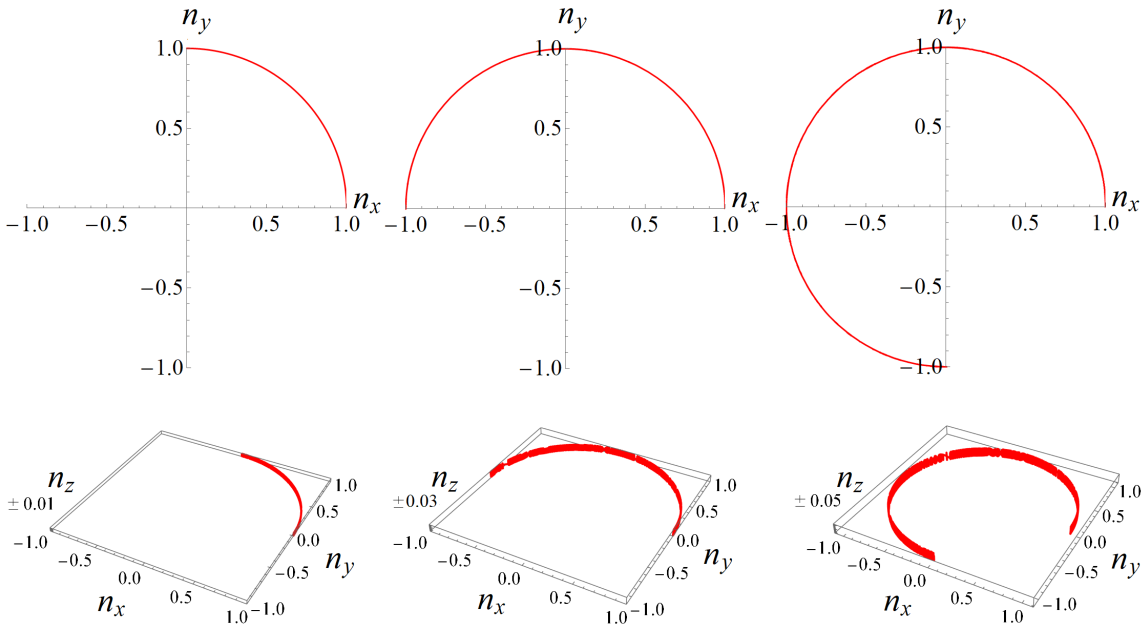

Figure 7.4: *Precession of an FG levitating above an SC. The modelled ferromagnet has a radius of* 30 μ*m and consists of* 7×10^{15} *electron spins. Depicted is the spin vector* $\check{\boldsymbol{n}}$*, whose projection onto the xy plane is shown in the upper row. The lower row shows the motion in three dimensions. The columns, from left to right, are for tilt angles [Eq. (7.17)] of 1, 2, and 3 degrees, respectively. In the modelling time runs for* ≈ 75 *seconds, which is a quarter of a period for the leftmost column, according to Eq. (7.16).*

Modelling the levitating FG dynamics of the spin vector $\boldsymbol{n}$ and the center-of-mass motion, we recover the frequencies ω_z and ω_β experimentally observed in Ref. [30], which describe oscillation of the center-of-mass in the vertical direction and libration of the magnetic moment about the vertical axis, respectively. Libration of the levitated ferromagnet at the frequency ω_β is predominantly caused by the image dipole field. Before introducing an additional external magnetic field to observe the effects of Larmor precession, let us note the precession motion that exists even without the introduction of an external magnetic field. We observe in the modelling a precession in the horizontal plane, with a frequency of

$$\omega_{xy} = \omega_I n_{z0} \ , \tag{7.16}$$

where n_{z0} is the initial vertical component of the FG magnetic moment, which is linked to the tilt angle β

$$\sin\beta = \frac{n_{z0}}{n_0} \ , \tag{7.17}$$

where n_0 is the unit spin vector and n_z is the length of its vertical component, at the initial moment of the modelling. Such a vertical component of the magnetic moment and spin translates to a vertical component of the total angular momentum, since $j = n + \ell$. The librational mode ω_β corresponds to an oscillation between n_z and ℓ_z. The image field does not change $j_z = n_z + \ell_z$, thus as long as the mean value of ℓ_z is not zero, precession occurs around the vertical axis, i.e. rotation of $\check{\mathrm{n}}$ in the horizontal plane ensues. In Fig. 7.4 we present examples of such a precession in the modelling. We also observe in the modelling that setting the FG's initial angular momentum to $\ell_z = -\sin\beta$ counteracts the effect of the tilt, as expected from conservation of angular momentum.

We can explain the appearance of ω_{xy} in terms of the image dipole. The image dipole precesses with the FG so the component of the image field in the horizontal xy plane acting on the FG is constant in the rotating frame. On the other hand, the tilt of the FG with respect to the vertical axis changes the field acting on the FG due to the image dipole — the librational oscillation causes an oscillating field along z that induces FG precession. Since the librational oscillation frequency is fast compared to the precession frequency, effectively the FG is sensitive to the average field, such that bigger librational oscillation results in a bigger effective field and faster precession. Note that the vertical component of the field appears due to the initial tilt angle of the FG magnetization axis out of the horizontal plane.

Such a precession was not observed in previous experiments as the ferromagnetic microsphere was not free to rotate in the horizontal plane, either because of the SC's tilt out of the horizontal plane in Ref. [30] or because of frozen flux in Ref. [28]. This tilt (or frozen flux) introduces a preferred direction for the magnetic moment of the levitating microsphere, so that it is situated in an energetic minimum; thus the ferromagnet oscillates around this direction (with frequency ω_α [30]) instead of precessing in the horizontal plane.

The above precession occurs due to the image field, while to use an FG to measure external torques we seek to observe the effect due to, for example, an external magnetic field. Therefore we introduce an external magnetic field B_{ext}, consequently adding $\mu\nabla\left(\boldsymbol{B}_{ext}\cdot\boldsymbol{n}\right)$ to the right-hand-side of Eq (7.14); Eq. (7.6) is modified to read

$$\frac{\partial \boldsymbol{j}}{\partial t} = \omega_L\left(\boldsymbol{n}\times\hat{\boldsymbol{B}}_{ext}\right) + \omega_{\mathfrak{B}}\left(\boldsymbol{n}\times\hat{\mathfrak{B}}\right) \ . \tag{7.18}$$

Since j_z is a constant of motion, if the tilt angle β is initially zero (horizontal FG with respect to the SC surface), so that $j_z(t=0) = 0$, then the angular momentum associated with precession $\ell_z = I\Omega$ must be equal and opposite to $s_z = N\hbar\sin\beta$. Thus we have

$$\sin\beta = \frac{I\Omega}{N\hbar} \ . \tag{7.19}$$

The magnitude of the image dipole field a distance z_0 above the SC surface is

$$|\mathfrak{B}| = \frac{\mu\mu_0}{4\pi z_0^3} \ , \tag{7.20}$$

and its z-component is

$$\mathfrak{B}_z = \mathfrak{B}\sin\beta \ . \tag{7.21}$$

The effective magnetic field that the FG experiences is the vector sum of the external magnetic field $\boldsymbol{B}_{ext}$ (taken to be along the z-axis) and $\mathfrak{B}_z$, so the precession frequency Ω is now given by

$$\Omega = \gamma \left(B_{\text{ext}} - \mathfrak{B}_z\right) = \gamma \left(B_{\text{ext}} - \mathfrak{B}\frac{I\Omega}{N\hbar}\right) \ . \tag{7.22}$$

Solving for Ω we find

$$\begin{aligned} \Omega &= \frac{\gamma B_{\text{ext}}}{1 + \gamma\mathfrak{B}/\omega_I} \ , \\ &= \frac{\gamma B_{\text{ext}}}{1 + \frac{\gamma\mu\mu_0 I}{2\pi z_0^3 N\hbar}} \ . \end{aligned} \tag{7.23}$$

Thus an FG levitated above an SC possesses an effectively reduced gyromagnetic ratio compared to the freely floating FG. The suppression of the effective gyromagnetic ratio due to the image field can be explained by a mechanism analogous to negative feedback [50]. Requiring $\Omega \ll \Omega^*$ for the FG to be in the precession regime gives

$$B_{\text{ext}} \ll \mathfrak{B} + \frac{\omega_I}{\gamma} \approx \mathfrak{B} \ . \tag{7.24}$$

The image field is typically much larger than B^*; hence precession can be observed in higher magnetic fields for an FG levitated over an SC compared to a freely floating FG. However, the corresponding precession frequency is smaller compared to a free FG. For a spherical FG with 30 micron radius, matching the experimental conditions of Ref. [30], the ratio of a free FG precession frequency to that for an FG levitated above an SC is $\approx 4 \times 10^6$. For 1 micron radius, this ratio is ≈ 340, so the suppression of precession frequency is reduced in the case of a smaller–radius FG. Based on Eq. (7.23), in Fig. 7.5 we plot as a function of the FG radius the ratio of the precession rate for a levitating FG above an SC to that for a freely floating FG.

This constraint on B_{ext} can be viewed as an effective threshold field for a levitated FG above an SC due to the image field. Modelling such a system for the conditions of the levitated ferromagnet from [30], but with 1 micron radius instead of 30 microns, we observe gyroscopic behaviour in the time domain, as shown in Fig. 7.6, consistently 340 times slower than that in the case of precession of a freely floating FG. As another check of the negative feedback explanation, we have varied the magnitude of the image field $\mathfrak{B}$ (by varying the gravitational field magnitude) and observed in the modelling suppressed precession rates (compared to freely floating FG) matching the expected rates from Eq. (7.23). In Fig. 7.6 we decoupled the motion of the center of mass from that of the spin vector $\check{\text{n}}$, for clarity. In the presence of both B_{ext} and a finite initial tilt angle β [that of Eq. (7.17)], the resulting precession frequency is the difference between the precession frequency in the case of initial tilt angle with null B_{ext}, and that with B_{ext} and null initial tilt angle [in accordance with Eq. (7.22)].

To observe ω_l, and then precession, an external magnetic field should be introduced, and several modifications should be made to the experimental apparatus used in [30]. One challenge is that external torques can effectively lock the ferromagnet's orientation and prevent precession. In a previous study of a ferromagnet levitated above a type-II SC, the ferromagnet's orientation was locked by the magnetic field due to trapped flux in the SC [28].

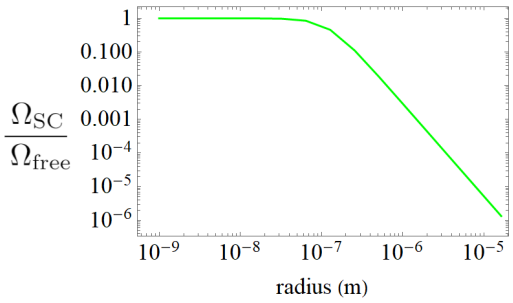

Figure 7.5: *The ratio of the precession frequency of an FG levitating above an SC [Eq. (7.23)] to that of a freely floating FG [Eq. (7.4)], as a function of the FG's radius. At radii below* 10^{-7} *m the ratio saturates to 1, i.e., the gyromagnetic ratio is the same as in free fall.*

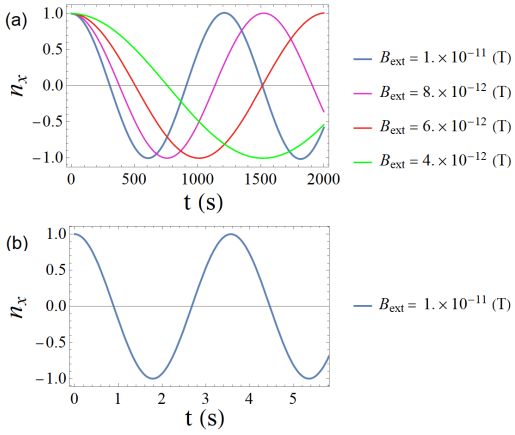

Figure 7.6: *(a) Spin component in the horizontal direction,* n_x*, as a function of time for an FG above a type-I SC, for several external magnetic fields. The precession rates are slower from that of a freely floating FG by an amount predicted in Eq. (7.23). (b) A freely floating FG situated in an external magnetic field of* 10^{-11} *T. Note the time scale — the precession frequency is about 340 times greater than for an FG above an SC for the same magnetic field in part (a).*

In Type-I SC, however, flux trapping can be eliminated. Yet in a recent experiment with a levitating microsphere the ferromagnet was not free to rotate in the horizontal plane because of locking due to a relative tilt of the surface of the cylindrical "bowl-shaped" trap in the SC [30]. In order to allow the microsphere to nutate and precess in the horizontal plane, a spherical "bowl-shaped" trap, instead of a cylindrical one, could be used. Following an observation of the horizontal precession due to the image field, an external magnetic field $\boldsymbol{B}_{ext}$ can be introduced in the z direction, much like was done in [28]. This field is expected to cause a librational motion of the FG around it, with a frequency ω_l which can be detected with a sufficiently sensitive magnetic field sensor, such as a SQUID. Reducing $B_{\rm ext}$ below the threshold in Eq. (7.24), nutational motion will appear. Further reducing the magnetic field will reveal ω_L. Note that the threshold in Eq. (7.24) is larger relative to Eq. (7.3), and thus

is easier to control technically.

7.5 Sensitivity to new physics

An FG is a correlated system of N electron spins that acts as a gyroscope with total spin $\sim N\hbar/2$. Spin projections transverse to the FG's magnetization axis fluctuate rapidly due to interaction with the crystalline lattice while, unless acted upon by an external torque, the expectation value of the total spin vector $\boldsymbol{S}$ remains fixed due to angular momentum conservation. This behavior enables rapid averaging of quantum uncertainty, opening the possibility of measuring torques on electron spins with a sensitivity many orders of magnitude beyond the present state-of-the-art [27, 39]. For this reason, FGs can be powerful tools to search for physics beyond the Standard Model [9].

Sensitivity estimates carried out in Refs. [27, 39] assume a freely floating FG in ultrahigh cryogenic vacuum at temperatures ≈ 0.1 K (residual He vapor density $\approx 10^3$ atoms/cm^3). Here we carry out sensitivity estimates for an FG levitated above a type-I SC under the vacuum conditions achieved in the experiment of Ref. [30] (residual helium pressure $\approx 10^{-5}$ mbar, corresponding to a He vapor density of $n \approx 3\times10^{13}$ atoms/cm^3) at a temperature of ≈ 4 K. We assume a spherical FG with radius ≈ 1 μm. Therefore the conditions assumed in the following discussion are practically realizable with relatively minor modifications to existing experimental apparatuses.

In Ref. [30], the dominant source of noise comes from collisions of He atoms with the FG. These collisions transfer angular momentum to the FG and cause a random walk of precession angle ϕ [27, 39]. For a spherical freely floating FG, the uncertainty in the precession frequency caused by gas collisions is given by [39]

$$\Delta\Omega_{col} \approx \frac{m_g r^2}{6N\hbar}\sqrt{\frac{n v_{th}^3}{\pi t}} \ , \tag{7.25}$$

where v_{th} is the mean thermal velocity of the residual gas atoms and m_g is their mass. However, in the case of an FG levitated above an SC, "negative feedback" from the image dipole field $\mathfrak{B}$ affects the FG's response to random torques caused by gas collisions in much the same way as it affects the Larmor precession frequency as described by Eq. (7.23). In general, the effect of any external torque $\boldsymbol{\tau}_{ext}$ acting on the FG is modified by this "negative feedback" mechanism. The equation, analogous to Eq. (7.18), describing the rate of change of total angular momentum $\boldsymbol{J}$ is

$$\boldsymbol{J} = \boldsymbol{\tau}_{ext} + \omega_{\mathfrak{B}}\left(\boldsymbol{S}\times\hat{\mathfrak{B}}\right) \ . \tag{7.26}$$

The external torques from gas collisions generate stochastic (random) variation in the precession frequency, and, because of nutation, a correlated stochastic variation in the tilt angle β and thus $\mathfrak{B}$. Just as Eq. (7.25) was derived using Eq. (7.6) as a starting point [27, 39], we can start from Eq. (7.26) and, following the same logic used to derive Eq. (7.23), show that the uncertainty in the precession frequency due to gas collisions for an FG levitated above an SC is given by

$$\Delta\Omega'_{col} \approx \frac{\Delta\Omega_{col}}{1+\gamma\mathfrak{B}/\omega_I} \ . \tag{7.27}$$

Therefore, under the conditions considered here, the effects of gas collisions on FG dynamics are smaller (compared to a freely floating FG) by 340 times. This results in an uncertainty in the measured FG precession frequency of

$$\Delta\Omega'_{col} \sim \frac{10^{-5}}{\sqrt{t}} \frac{\text{rad}}{\text{s}} . \tag{7.28}$$

Other potential noise sources, such as thermal currents and blackbody radiation, were considered in Refs. [27, 39] and are also found to be negligible under the experimental conditions of Ref. [30]. Furthermore, the experimental results in Ref. [30] for a 30-micron-radius levitated ferromagnet showed that eddy current damping was negligible, and eddy current damping contributes even less for smaller FG radii: the eddy current power dissipation in a conducting sphere is $\propto r^5$. A one-micron radius ferromagnet can be single domain, in which case direct (hysteresis-based) magnetic losses should be largely suppressed as well.

The precession of the FG can be measured with a SQUID. For a SQUID with pick-up loop radius of ≈ 1 μm situated about a micron from an FG (such that the flux capture is maximal), the amplitude of the time-varying magnetic flux is $\Phi \approx 10^{-12}$ T $\cdot$ m^2. Low-temperature SQUIDs have a flux sensitivity of $\delta\Phi \lesssim 10^{-21}$ T $\cdot$ m$^2/\sqrt{\text{Hz}}$ [51–54], which yields a corresponding sensitivity to the precession angle of $\delta\phi \approx \delta\Phi/\Phi \approx 10^{-9}$ rad$/\sqrt{\text{Hz}}$. Thus the detection-limited uncertainty in a measurement of the FG precession frequency $\Omega = d\phi/dt$ integrating over a time t is $\Delta\Omega_{det} \sim 10^{-9} t^{-3/2}$ rad/s. Since the uncertainty in the measurement of precession due to gas collisions is far larger than $\Delta\Omega_{det}$, requirements on the pick-up loop geometry and SQUID sensitivity are correspondingly relaxed. For example, a pick-up loop radius of $R \approx 1$ mm positioned ≈ 1 mm from the FG would achieve a detection-limited sensitivity in 1 s of integration time better than the gas collision limit,

$$\Delta\Omega'_{det} \sim 10^{-6} \frac{1}{t^{3/2}} \frac{\text{rad}}{\text{s}} . \tag{7.29}$$

Vibrations were another important source of technical noise in the experiment described in Ref. [30]. Relative motion between the position of the FG and the SQUID pick-up loop lead to variations in the flux through the loop and consequently generate noise in the precession measurement. Commercial vibration isolation systems used, for example, in atomic force microscopy experiments can reduce vibration amplitudes to $\delta x \lesssim 10^{-5}$ mm at frequencies $\lesssim 1$ Hz [55]. The fractional flux noise in the pick-up loop $\delta\Phi/\Phi \sim \delta x/x$, where $x \approx R \approx 1$ mm is the distance between the FG and the pick-up loop. This corresponds to an uncertainty in the precession measurement similar to the gas-collision limit,

$$\Delta\Omega_{vib} \sim \frac{10^{-5}}{\sqrt{t}} \frac{\text{rad}}{\text{s}} . \tag{7.30}$$

It is notable that $\Delta\Omega_{det}$ appears to surpass the “standard quantum noise limit" [27, 56]. While the energy resolution per bandwidth (E_R) for existing magnetometers is at or above the quantum limit $\hbar$, an FG can in principle achieve $E_R \ll \hbar$, under conditions where external sources of error are controlled so that the FG sensitivity is limited by detector noise [33]. Such accuracy arises because the quantum uncertainty is rapidly averaged by the internal ferromagnetic spin-lattice interaction, while the FG maintains gyroscopic stability due to

the conservation of the total angular momentum (dominated by the intrinsic spin). Another way to understand the sensitivity of an FG is to note that the ferromagnetic spin-lattice interaction spreads the quantum fluctuations over a broad frequency band ($\gtrsim 1-100$ GHz). Due to the gyroscopic stability, one can still measure slow changes of the average direction of the FG spin. Integrating over long periods of time averages the quantum fluctuations, acting as a "low-pass filter" for the quantum noise. Thus a high sensitivity to comparatively low-frequency spin precession can be achieved.

As an example of the potential of FGs as tools for testing fundamental physics, we consider an experimental search for yet-to-be-discovered (exotic) spin-dependent interactions mediated by new bosons [57–59]. In particular, axions and axionlike particles (ALPs) mediate a pseudoscalar (P) interaction between electrons described by the potential

$$V_{PP}(\boldsymbol{R}) = \frac{(g_P^e)^2}{4\pi\hbar c}\frac{\hbar^3}{4m_e^2 c} \cdot \left\{ \boldsymbol{S}_1 \cdot \boldsymbol{S}_2 \left(\frac{m_b c}{\hbar R^2} + \frac{1}{R^3} + \frac{4\pi}{3}\delta^3(\boldsymbol{R}) \right) - \left(\boldsymbol{S}_1 \cdot \hat{\boldsymbol{R}}\right)\left(\boldsymbol{S}_2 \cdot \hat{\boldsymbol{R}}\right) \left(\frac{m_b^2 c^2}{\hbar^2 R} + \frac{3m_b c}{\hbar R^2} + \frac{3}{R^3} \right) \right\} e^{-\frac{m_b c R}{\hbar}} , \tag{7.31}$$

where $(g_P^e)^2/4\pi\hbar c$ is the dimensionless pseudoscalar coupling constant between electrons, m_e is the electron mass, $\boldsymbol{S}_{1,2}$ are the electron spins, m_b is the mass of the hypothetical pseudoscalar boson, c is the speed of light, and $\boldsymbol{R} = R\hat{\boldsymbol{R}}$ is the separation between the electrons.

One could search for spin precession induced by the pseudoscalar-mediated dipole-dipole interaction, Eq. (7.31), by modulating the distance between a polarized spin source and a levitated FG. Some of the most stringent laboratory constraints on such exotic dipole-dipole interactions have been achieved using spin-polarized torsion balances [60, 61] with $SmCo_5$ as a polarized spin source. In $SmCo_5$, the orbital magnetic moment of the Sm^{3+} electrons nearly cancels their spin moment, and so $SmCo_5$ possesses a high spin polarization while having a relatively small magnetic moment, thus reducing magnetic-field-related effects. The spin–polarized source in such an experiment could be positioned underneath the SC to further shield the FG from the magnetic field due to the spin source. Although the SC will shield the FG from the magnetic field of the $SmCo_5$ spin source, it turns out that the pseudoscalar interaction (7.31) is unshielded by the SC [62]. This is a consequence of the fact that SC shielding relies on the coupling of magnetic fields to currents rather than to electron spins. Thus, since the Meissner effect is unrelated to interactions with the electron spins, the SC shield has no effect on the pseudoscalar-mediated dipole-dipole interaction described by Eq. (7.31) [61, 62]. Note that effects due to exotic interactions manifest as external torques $\boldsymbol{\tau}_{ext}$ as described by Eq. (7.26), and therefore their influence on the precession frequency is suppressed by the same factor appearing in Eqs. (7.23) and (7.27).

An experiment using a one-micron-radius FG levitated above an SC would be sensitive to the region of parameter space bound from below by the dotted red line in Fig. 7.7. We assume that the $SmCo_5$ spin source is a one-mm radius sphere positioned one mm away to the FG to allow space for the SC. A one-mm-radius $SmCo_5$ sphere would contain $\sim 5 \times 10^{19}$ polarized electron spins. The FG sensitivity to spin precession is given by Eq. (7.28). For comparison, Fig. 7.7 shows the most stringent laboratory constraints in this region of parameter space,

which are based on spin-polarized torsion-balance measurements [60] and He spectroscopy [63, 64]; related experiments are discussed in the review [9] and Refs. [65–72]. Compared to these existing constraints, our proposed experiment with a levitated FG can explore many decades of unconstrained parameter space. This illustrates the potential of FGs as tools to search for exotic spin-dependent interactions, which could open a window to beyond-the-Standard-Model physics. We also note that new bosons such as axions and ALPs are candidates to explain the nature of dark matter [9], and much like other types of precision mechanical sensors [73], FGs can be useful tools for the potential detection of bosonic, wavelike dark matter.

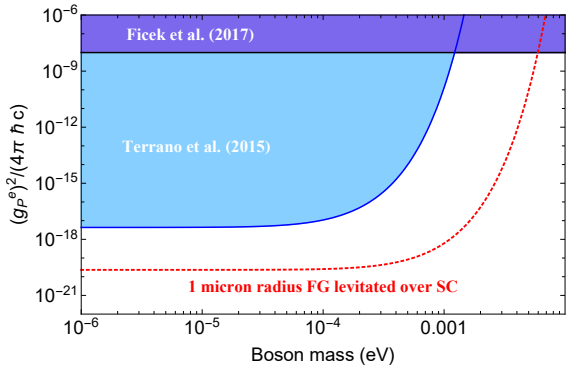

Figure 7.7: *Comparison between the existing experimental constraints (solid lines and shaded regions) on a pseudoscalar-mediated dipole-dipole interaction between electron spins and the projected sensitivity of an experiment using a one micron radius spherical FG levitated above a type-I SC (dotted red line). The projected sensitivity is based on the gas-collision limit [Eq. (7.28), comparable to the expected technical limit due to vibrations and microphonic noise, Eq. (7.30)]. Constraints shown with the black line and dark blue shaded region are based on He spectroscopy [63]; constraints shown with the blue line and light blue shaded region are from an experiment using a spin-polarized torsion pendulum [60]. The proposed experiment with the levitated FG assumes as a polarized spin source a 1-mm radius $SmCo_5$ sphere positioned 1 mm away from the FG and an integration time of $t = 10^6$ s.*

7.6 Conclusion

In summary, we present a roadmap for experimental realization of a ferromagnetic gyroscope (FG). In essence, an FG is a ferromagnet that precesses under the influence of external torques. A ferromagnetic gyroscope is a new type of sensor that can be particularly useful as a tool for precision tests of fundamental physics.

We model and explain the dynamics of an FG freely floating in space and propose a strategy to experimentally realize an FG. The librational mode in the magnetization dynamics serves as a calibration tool for the applied magnetic field. This enables the magnetic field to be tuned to sufficiently small magnitudes so that the FG precession mode can be observed.

We also compare the dynamics of a freely floating FG to that of an FG levitated above

a type-I superconductor. The effect of the SC is modelled using an image dipole field. We find that the SC has a significant effect on the FG dynamics: the image dipole field generates a "negative feedback" that effectively suppresses the response of an FG to external torques as compared to the case of a freely floating FG. The effective magnetic field threshold below which precession is dominant is thus higher in the case of an FG levitated above an SC as compared to a freely floating FG [Eq. (7.24)] while the observed precession frequency for a given field strength is lower [Eq. (7.23)].

Acknowledgments

P. F. would like to thank Martti Raidal and the team in NICPB for their hospitality in Tallinn, Estonia. This research was supported by the Heising-Simons and Simons Foundations, the U.S. National Science Foundation under Grant No. PHY-1707875, the DFG through the DIP program (FO703/2-1), and by a Fundamental Physics Innovation Award from the Gordon and Betty Moore Foundation. The work of D. B. supported in part by the DFG Project ID 390831469: EXC 2118 (PRISMA+ Cluster of Excellence), the European Research Council (ERC) under the European Union Horizon 2020 Research and Innovation Program (grant agreement No. 695405) and the DFG Reinhart Koselleck Project. The work of A. S. supported in part by the US National Science Foundation grant 1806557, US Department of Energy grant DE-SC0019450, the Heising-Simons Foundation grant 2015-039, the Simons Foundation grant 641332, and the Alfred P. Sloan foundation grant FG-2016-6728. The work of C. T., A. V., and H. U. supported in part by the EU H2020 FET project TEQ (Grant No. 766900), the Leverhulme Trust (RPG2016-046) and the COST Action QTSpace (CA15220).

Bibliography

[1] C. W. F. Everitt, et. al., Phys. Rev. Lett. **106**, 221101 (2011).

[2] A. Gebauer, M. Tercjak, K. Ulrich Schreiber, H. Igel, J. Kodet, U. Hugentobler, J. Wassermann, F. Bernauer, C.-J. Lin, S. Donner, S. Egdorf, A. Simonelli, and J.-P. R. Wells, Phys. Rev. Lett. 125, 033605 (2020).

[3] C. Zhang, H. Yuan, Z. Tang, W. Quan, and J. C. Fang, Appl. Phys. Rev. 3, 041305 (2016).

[4] T. W. Kornack, R. K. Ghosh, and M. V. Romalis, Physical review letters 95, 230801 (2005).

[5] E. A. Donley, IEEE Sensors 2010 Conf. 7–22 (2010).

[6] M. Larsen and M. Bulatowicz, 2012 IEEE international frequency control symposium proceedings. IEEE, (2012).

[7] M. P. Ledbetter, K. Jensen, R. Fischer, A. Jarmola, and D. Budker, Phys. Rev. A 86, 052116 (2012).

[8] T. Wu, J. W. Blanchard, D. F. Jackson Kimball, M. Jiang, and D. Budker. Phys. Rev. Lett. 121, 023202 (2018).

[9] M. S. Safronova, D. Budker, D. DeMille, Derek F. Jackson Kimball, A. Derevianko, and C. W. Clark, Rev. Mod. Phys. 90, 025008 (2018).

[10] J. M. Brown, S. J. Smullin, T. W. Kornack, and M. V. Romalis, Phys. Rev. Lett. 105, 151604 (2010).

[11] M. Smiciklas, J. M. Brown, L. W. Cheuk, S. J. Smullin, and M. V. Romalis, Phys. Rev. Lett. 107, 171604 (2011).

[12] T. Pruttivarasin, M. Ramm, S. G. Porsev, I. I. Tupitsyn, M. S. Safronova, M. A. Hohensee, and H. Häffner, Nature (London) 517, 592 (2015).

[13] G. Vasilakis, J. M. Brown, T. W. Kornack, and M. V. Romalis, Phys. Rev. Lett. 103, 261801 (2009).

[14] M. Bulatowicz, R. Griffith, M. Larsen, J. Mirijanian, C. B. Fu, E. Smith, W. M. Snow, H. Yan, and T. G. Walker, Phys. Rev. Lett. 111, 102001 (2013).

[15] L. Junyi, A. Almasi, and M. Romalis, Phys. Rev. Lett. 120, 161801 (2018).

[16] L. Hunter, J. Gordon, S. Peck, D. Ang, and J.-F. Lin, Science 339, 928 (2013).

[17] Wu, T., Blanchard, J.W., Centers, G.P., Figueroa, N.L., Garcon, A., Graham, P.W., Kimball, D.F.J., Rajendran, S., Stadnik, Y.V., Sushkov, A.O. and Wickenbrock, A., Phys. Rev. Lett. 122, 191302 (2019).

[18] C. Abel, N. J. Ayres, G. Ban, G. Bison, K. Bodek, V. Bondar, M. Daum et al., Phys. Rev. X 7, 041034 (2017).

[19] T. S. Roussy, D. A. Palken, W. B. Cairncross, B. M. Brubaker, D. N. Gresh, M. Grau, K. C. Cossel et al., arXiv:2006.15787 (2020).

[20] A. Garcon, J. W. Blanchard, G. P. Centers, N. L. Figueroa, P. W. Graham, D. F. Jackson Kimball, S. Rajendran, A. O. Sushkov, Y. V. Stadnik, A. Wickenbrock, T. Wu, and D. Budker, Sci. Adv. 5, eaax4539 (2019).

[21] B. Graner, Y. Chen, E. G. Lindahl, and B. R. Heckel, Phys. Rev. Lett. 116, 161601 (2016).

[22] Andreev V et al (ACME Collaboration) Nature 562 355 (2018).

[23] W. B. Cairncross, D. N. Gresh, M. Grau, K. C. Cossel, T. S. Roussy, Y. Ni, Y. Zhou, J. Ye, and E. A. Cornell, Phys. Rev. Lett. 119 1–5 (2017).

[24] D. J. Wineland1, J. J. Bollinger, D. J. Heinzen, W. M. Itano, and M. G. Raizen, Phys. Rev. Lett. 67, 1735 (1991).

[25] B. J. Venema, P. K. Majumder, S. K. Lamoreaux, B. R. Heckel, and E. N. Fortson, Phys. Rev. Lett. 68, 135 (1992).

[26] D. F. Jackson Kimball, J. Dudley, Y. Li, D. Patel, and J. Valdez, Phys. Rev. D 96, 075004 (2017).

[27] D. F. Jackson Kimball, A. O. Sushkov, and D. Budker, Phys. Rev. Lett. **116**, 190801 (2016).

[28] T. Wang, S. Lourette, S. R. O Kelley, M. Kayci, Y. B. Band, D. F. Jackson Kimball, A. O. Sushkov, and D. Budker, Phys. Rev. Appl. **11**, 044041 (2019).

[29] J. Gieseler, A. Kabcenell, E. Rosenfeld, J. D. Schaefer, A. Safira, M. J. A. Schuetz, C. Gonzalez-Ballestero, C. C. Rusconi, O. Romero-Isart, and M. D. Lukin, Phys. Rev. Lett. **124**, 163604 (2020).

[30] A. Vinante, P. Falferi, G. Gasbarri, A. Setter, C. Timberlake, and H. Ulbricht, Phys. Rev. Applied 13, 064027 (2020).

[31] C. Timberlake, G. Gasbarri, A. Vinante, A. Setter, and H. Ulbricht, Appl. Phys. Lett. **115**, 224101 (2019).

[32] P. Huillery, T. Delord, L. Nicolas, M. Van Den Bossche, M. Perdriat, and G. Hétet, Phys. Rev B **101**, 134415 (2020).

[33] M. W. Mitchell and S. Palacios Alvarez, Rev. Mod. Phys. 92, 21001 (2020).

[34] N. El-Sheimy and A. Youssef, Satell. Navig. 1, 2 (2020).

[35] Y. B. Band, Y. Avishai, and A. Shnirman, Phys. Rev. Lett. **121**, 160801 (2018).

[36] J. Prat-Camps, C. Teo, C. C. Rusconi, W. Wieczorek, and O. Romero-Isart. Phys. Rev. Appl. **8**, 034002 (2017).

[37] D. M. Burn, S. L. Zhang, G. Q. Yu, Y. Guang, H. J. Chen, X. P. Qiu, G. van der Laan, and T. Hesjedal, Phys. Rev. Lett. **125**, 137201 (2020).

[38] K. Neeraj, N. Awari, S. Kovalev, D. Polley, N. Z. Hagström, S. S. P. K. Arekapudi, A. Semisalova, K. Lenz, B. Green, J.-C. Deinert, I. Ilyakov, M. Chen, M. Bawatna, V. Scalera, M. D'Aquino, C. Serpico, O. Hellwig, J.-E. Wegrowe, M. Gensch, and S. Bonetti, Nat. Phys. (2020).

[39] P. Fadeev, T. Wang, Y. B. Band, D. Budker, P. W. Graham, A. O. Sushkov, and D. F. Jackson Kimball, ArXiv: **2006.09334** (2020).

[40] S. J. Barnett, Phys. Rev. **6**, 239 (1915).

[41] A. Einstein and W. J. de Haas, Verh. Dtsch. Phys. Ges. **17**, 152 (1915); **18**, 173 (1916).

[42] O. W. Richardson, Phys. Rev. (Ser. I) **26**, 248 (1908).

[43] L. D. Landau and L. M. Lifshitz, Phys. Zeitsch. der Sow. **8**, 153 (1935); reprinted in Ukr. J. Phys. **53**, 14 (2008).

[44] T. L. Gilbert, IEEE Trans. Magn. **40**, 3443 (2004).

[45] C. C. Rusconi, V. Pöchhacker, J. I. Cirac, and O. Romero-Isart, Phys. Rev. B 96, 134419 (2017).

[46] P. Morales, D. E. Jaramillo, and J. Osorio, Rev. Mex. Fis. E 62, 44 (2016).

[47] A. Cansiz, J. R. Hull, and Ö. Gundogdu, Supercond. Sci. Technol. 18, 990 (2005).

[48] K. Giaro, W. Gorzkowski, and T. Motylewski, Physica C. 168, 479 (1990).

[49] Q.-G. Lin, Phys. Rev. B 74, 024510 (2006).

[50] P. Horowitz and W. Hill, *The Art of Electronics* (Cambridge University Press, Cambridge, England, 2015).

[51] D. D. Awschalom, J. R. Rozen, M. B. Ketchen, W. J. Gallagher, A. W. Kleinsasser, R. L. Sandstrom, and B. Bumble, Appl. Phys. Lett. **53**, 2108 (1988).

[52] O. Usenko, A. Vinante, G. Wijts, and T. H. Oosterkamp, Appl. Phys. Lett. **98**, 133105 (2011).

[53] W. Gardner, Sean T. Halloran, Erik A. Lucero, and Kathryn A. Moler, Rev. Sci. Inst. **79**, 053704 (2008).

[54] J. Clarke and A. I. Braginski, eds., *The SQUID Handbook Vol. 1* (Wiley, Weinheim, 2004).

[55] www.minusk.com

[56] V. Giovannetti, S. Lloyd, and L. Maccone, Science 306, 1330 (2004).

[57] J. E. Moody and F. Wilczek, Phys. Rev. D **30**, 130 (1984).

[58] B. A. Dobrescu and I. Mocioiu, Journal of High Energy Physics **2006.11**, 005 (2006).

[59] P. Fadeev, Y. V. Stadnik, F. Ficek, M. G. Kozlov, V. V. Flambaum, and D. Budker, Phys. Rev. A **99**, 022113 (2019).

[60] W. A. Terrano, E. G. Adelberger, J. G. Lee, and B. R. Heckel, Phys. Rev. Lett. **115**, 201801 (2015).

[61] B. R. Heckel, E. G. Adelberger, C. E. Cramer, T. S. Cook, Stephan Schlamminger, and U. Schmidt, Phys. Rev. D **78**, 092006 (2008).

[62] D. F. Jackson Kimball, J. Dudley, Y. Li, S. Thulasi, Szymon Pustelny, D. Budker, and M. Zolotorev, Phys. Rev. D **94**, 082005 (2016).

[63] F. Ficek, D. F. Jackson Kimball, M. G. Kozlov, N. Leefer, S. Pustelny, and D. Budker, Phys. Rev. A **95**, 032505 (2017).

[64] C. Delaunay, C. Frugiuele, E. Fuchs, and Y. Soreq, Phys. Rev. D **96**, 115002 (2017).

[65] L. Hunter, J. Gordon, S. Peck, D. Ang, and J.-F. Lin, Science **339**, 928 (2013).

[66] B. R. Heckel, W. A. Terrano, and E. G. Adelberger, Phys. Rev. Lett. **111**, 151802 (2013).

[67] S. Kotler, R. Ozeri, and D. F. Jackson Kimball, Phys. Rev. Lett. **115**, 081801 (2015).

[68] Y. J. Kim, P.-H. Chu, and I. Savukov, Phys. Rev. Lett. **121**, 091802 (2018).

[69] W. Ji, Y. Chen, C. Fu, M. Ding, J. Fang, Z. Xiao, K. Wei, and H. Yan, Phys. Rev. Lett. **121**, 261803 (2018).

[70] X. Rong, M. Jiao, J. Geng, B. Zhang, T. Xie, F. Shi, C.-K. Duan, Y.-F. Cai, and J. Du, Phys. Rev. Lett. **121**, 080402 (2018).

[71] M. Jiao, X. Rong, H. Liang, Y.-F. Cai, and J. Du, Phys. Rev. D **101**, 115011 (2020).

[72] J. Ding, J. Wang, X. Zhou, Y. Liu, K. Sun, A. O. Adeyeye, H. Fu, X. Ren, S. Li, P. Luo, and Z. Lan, Phys. Rev. Lett. **124**, 161801 (2020).

[73] D. Carney, G. Krnjaic, D. C. Moore, C. A. Regal, G. Afek, S. Bhave, B. Brubaker et al., Quantum Science and Technology (2020).

Conclusion

The projects completed in this thesis represent progress in theoretical understanding and experimental efforts in several disciplines:

- In nuclear physics, the magnitude of time-reversal-invariance violation in neutron-nucleus scattering provides the theoretical validation to ongoing experimental efforts to detect P and T-violation in nuclear systems (like those of the NOPTREX collaboration). In the future our calculations will continue to guide the search for this effect. If the effect is detected, our results can be used to relate the observations to the fundamental parameters of the T-violating interaction.

  Searches for temporal or spatial variation of the fine-structure constant α serve as further motivation to build a nuclear clock based on the lowest nuclear transition of thorium-229 and use such a clock to explore fundamental physics. The possibility of discovering variation of constants in Mössbauer transitions in particular might invigorate the technique of Mössbauer spectroscopy. The link we uncovered between the enhancement of α and quark-mass m_q variation is interesting by itself as a bridge between enhancements of different constants — it will be used and improved upon.

- In the search for new bosons, our results help to constrain the mass and coupling strength of the particles that could one day provide an explanation for dark matter. We collaborated with researchers from China to search for these hypothetical particles using a spin-based amplifier [1, 2]. In this type of search, macroscopic polarized masses are probed, with the effect of exotic-boson exchange being able to manifest as an effective magnetic field that may act on the mass.

  Moving forward, the bounds on spin-dependent one-boson exchange potentials will continue to improve, reflecting the improvement in measurement devices and novel ways of detection. Newer bounds and theoretical predictions will be compared to our bounds. Our list of potentials will continue to be used as a source where these general spin-dependent potentials, and their properties, appear. The search for new bosons will go on until the day they are found, or the need for them diminishes in case the motivation for their existence subsides. An example of such a scenario is the possibility of dark matter originating as modified Newtonian dynamics or sterile neutrinos.

- Our proposal to detect a magnet's precession due to gravity, followed by exploring the dynamics of a levitated magnet above a superconductor, led to a new international team effort. Prior to detecting gravitational effects acting on the magnetization of a ferromagnet situated on a satellite, a proof-of-principle setup should be built on Earth. To

this end, we formed a collaboration, LEvitated MAgnets for QUantum MEtrology, to build a prototype system — LEMAQUME is a European Union QuantERA project [3]. Moreover, our idea for a test of the gyrogravitatonal ratio motivates developments in metric-affine gravity [4], quantum hydrodynamics of spinning particles [5], and foundations tests of quantum physics in space [6].

We predicted, discussed, proposed, and analyzed novel effects in the spectra of nuclear, atomic, and mesoscopic systems. In this way we explored hills and valleys (in the spectra), charting the terrain for further exciting developments.

Bibliography

[1] H. W. Su, Y. H. Wang, M. Jiang, W. Ji, P. Fadeev, D. H. Hu, X. H. Peng, and D. Budker, Sci. Adv. **7**, eabi9535 (2021).

[2] Y. Wang, H. Su, M. Jiang, Y.Huan, Yu. Qin, C. Guo, Z. Wang, D. Hu, W. Ji, P. Fadeev, X. Peng, and D. Budker, arXiv:2201.11847.

[3] www.lemaqume.org

[4] S. Bahamonde and J. G. Valcarcel, Eur. Phys. J. C **81**, 495 (2021).

[5] M. Iv. Trukhanova and Y. N. Obukhov, Universe **7(12)**, 498 (2021).

[6] G. Gasbarri, A. Belenchia, M. Carlesso, S. Donadi, A. Bassi, R. Kaltenbaek, M. Paternostro, H. Ulbricht, Commun. Phys. **4**, 155 (2021).

List of talks and conferences

The projects completed in this thesis were presented in several invited talks and conferences. These are listed below, alongside workshops and winter/summer schools I took part in during the PhD.

- Greenhorn meeting, Heidelberg, Germany (2018).
- Invited talk, Centre for Quantum and Optical Science, Swinburne University of Technology, Melbourne, Australia (2019).
- Invited talk, quantum science seminar, University of Queensland, Australia (2019).
- Greenhorn meeting — organizer, Mainz, Germany (2019)
- The 37th Advanced School in Theoretical Physics: New Ideas for Old Puzzles in Particle Physics. Jerusalem (2020).
- Invited talk, New Zealand Institute for Advanced Study at Massey University (2020).
- Vienna Summer School on Gravitational Quantum Physics (2020).
- Invited talk, Institute of Physics, University of Tartu, Estonia (2020).
- Invited talk, National Institute of Chemical Physics and Biophysics, Estonia (2020).
- Moriond Gravitation (2021).
- Invited talk, Adam Mickiewicz University, Poland (2021).
- Invited talk, University of Queensland, Australia (2021).
- Invited talk, Quantum Engineering of Levitated System, Benasque, Spain (2022).
- Seminar on high-precision measurements and searches for new physics, Bad Honnef, Germany (2022).
- 11th International conference on precision physics of simple atomics systems (PSAS 2022), Warsaw, Poland (2022).
- Invited talk, Physics Department, Boğaziçi University, Istanbul, Turkey (2022).